STUDY OF THE RELATIVE RESIDUAL SURFACE STRESSES ON 6H SILICON CARBIDE CERAMIC DUE TO MACHINING USING LASER RAMAN MICROPROBE SPECTROSCOPY

Thesis
submitted to

Graduate Engineering and Research
School of Engineering

UNIVERSITY OF DAYTON

In Partial Fulfillment of the Requirements for

The Degree

Master of Science in Electro-Optics

by

Joseph L. Binford, III

UNIVERSITY OF DAYTON

Dayton, Ohio
July 1996

STUDY OF THE RELATIVE RESIDUAL SURFACE STRESSES ON 6H SILICON CARBIDE CERAMIC DUE TO MACHINING USING LASER RAMAN MICROPROBE SPECTROSCOPY

APPROVED BY:

Perry P. Yaney, Ph.D.
Professor, Electro-Optics Program
Committee Chair

Robert J. Brecha, Ph.D.
Assistant Professor, Department of Physics
Committee Member

Norman L. Hecht, Ph.D.
Professor, Graduate Material Engineering
Committee Member

Donald L. Moon, Ph.D.
Associate Dean
Graduate Engineering Programs & Research

Joseph F. Lestingi, D. Eng., P.E.
Dean
School of Engineering

ii

ABSTRACT

**STUDY OF THE RELATIVE RESIDUAL SURFACE STRESSES ON
6H SILICON CARBIDE CERAMIC DUE TO MACHINING USING LASER
RAMAN MICROPROBE SPECTROSCOPY**

BINFORD, Joseph L. III
University of Dayton, 1996
Advisor: Dr. Perry P. Yaney

Microcracks and other defects in ceramic materials are often caused by the presence of residual surface stress. These imperfections affect the strength of the ceramic material and eventually cause mechanical failure. Information about the residual surface stress can determine the best machining process for obtaining optimal characteristics in finished ceramic materials. In this work, sixteen 6H polytype silicon carbide (SiC) specimens comprising nine processing techniques were studied. The main goal of the studies were measurements of the Raman shifts and linewidths of the 767 cm^{-1} (E_1), the 788 cm^{-1} (A_{1T}/E_2), and the 797 cm^{-1} (E_{1T}) Raman lines on the planar optic branch for 6H SiC. Emphasis was placed on measurements of the 788 cm^{-1} (TO) Raman line since it has a relatively large signal strength and is highly stable. These Raman shift and linewidth measurements represented the relative residual surface stress in the ceramic material. A laser Raman microprobe was used to conduct these investigations and includes the use of a two-dimensional liquid-nitrogen-cooled CCD array detector mounted on a modified

Czerny-Turner double spectrometer and a diode-laser-pumped, doubled cw Nd:YAG laser at 532 nm. The studies showed that creep feed grinding produces less residual surface stress when compared with conventional grinding. However, the use of heat treatment or oxidation on baseline (conventional) grind specimens reduced the residual surface stress below that of the creep feed grind specimens. These studies also revealed that decreased residual surface stress is associated with higher flexural strength. Other studies were conducted to investigate polarization, fluorescence, the presence of other SiC polytypes, and grinding damage profiles obtained by varying the incident laser wavelength. A galvanometer scanner was incorporated into the Raman microprobe system and operated successfully during preliminary studies to demonstrate its capabilities for further spectroscopic image processing applications.

ACKNOWLEDGMENTS

There are many people to whom I am deeply grateful for their encouragement and support over the past year as I worked to complete my master's degree. (I suppose I could not possibly list all of those who have in some way or other aided me in this endeavor, through an encouraging word, a thoughtful comment, or a simple praise.) I am especially grateful to my advisor, Dr. Perry P. Yaney, for his dedication, guidance, and instruction which enabled me to further my scientific understanding and technical abilities. His insightful discussions and wry sense of humor helped to enliven my studies throughout the course of the research.

I also wish to thank Dr. Norman L. Hecht, of the University of Dayton Research Institute (UDRI), Metals and Ceramics Division, for his guidance and support of this work.[*] His helpful comments and suggestions were deeply appreciated. In addition, I wish to thank Dr. Muhammad Karim of the Electro-Optics Program for my financial assistance[**] during a portion of my thesis research. Also, I would like to thank Dr. J. Michael O'Hare and the University of Dayton Department of Physics for additional financial support of the project.

I wish to express to my thesis committee, Dr. Perry P. Yaney, Dr. Norman L. Hecht, and Dr. Robert J. Brecha, my gratitude for their diligent technical reviews of this thesis and their helpful suggestions and recommendations during its refinement. I would

v

also like to thank Mr. Dale McCullum, Mr. Steve Goodrich, and Mr. Leon Chuck for their helpful discussions on ceramics.

I would also like to acknowledge Mr. Alan Forsythe of the U.D. Kettering Labs machine shop, who successfully machined the aluminum pieces needed for mounting the galvanometer scanner assembly despite my inexperience in creating mechanical drawings! In addition, I would like to thank Mr. Frantz Hebbeler of the U.D. Physics Department for his helpful machining tips, his words of encouragement, and his interesting conversations. I'm also grateful to Mrs. Linda J. Fiorita for her helpfulness in the physics office and for the cheerful attitude which she imparts to everyone.

I am so very thankful for the love, encouragement, and prayerful support my parents have given me throughout my graduate studies at the University of Dayton. I also wish to thank my brother Jim for all the love and moral support he has shown me. I thank God for His infinite love and mercy in strengthening me during the times that I needed Him most and for inspiring me to persevere in the face of obstacles to achieve the plans He has for me. I'm reminded of a favorite verse in Scripture spoken by the Apostle Paul to the church in Corinth:

> *For our light and momentary troubles are achieving for us an eternal glory that far outweighs them all.*
>
> II Corinthians 4:17 (NIV)

This thesis is dedicated to the memory of my maternal grandmother, Mrs. Crystal Ires Garrity Baurle, who, because of her love for learning and her love for me, would have enjoyed celebrating this wonderful achievement with me.

TABLE OF CONTENTS

CHAPTER

Results

LIST OF FIGURES

LIST OF TABLES

CHAPTER I

INTRODUCTION

The Raman effect was discovered by C. V. Raman in 1921.[1] Raman spectroscopic techniques play an important role in understanding the microstructure of many materials. Due to its typically weak signal, the potential of Raman spectroscopy wasn't fully realized until the 1960's with the advent of the laser, a source of light strong enough to induce easily-measurable levels of Raman signal using electronic detection. For example, the Raman signal strength is about 10^{-11} of the incident light power for 6H SiC specimens based on the experimental setup used in this research. (See Appendix A.)

Raman spectroscopy is a powerful research tool for studying the atomic lattices and molecular structures of materials. By measuring the Raman signal, the vibrational modes and hence the intrinsic properties of the material may be determined. In combination with other well known research methods, such as IR absorption spectroscopy and x-ray diffraction techniques, Raman spectroscopy can aid in the measurement of bond length, bond angle, and bond strength.

The vibrational modes of solids may also be analyzed using Raman spectroscopy based on principles from solid state physics and crystallography. In addition, the creation of new modes, the splitting of modes, and the broadening and/or shifting of modes can give an indication of the residual stresses (bulk or surface) in the material due to

1

machining treatments during processing. These changes in the modes arise from compression or tension of the crystallite structure due to changes in the crystal symmetry, the local size of the lattice, or both.

Emphasis in both industry and government is more than ever being placed on ways to evaluate the quality and integrity of materials. A Raman microprobe facility greatly aids in the nondestructive testing of materials by measuring the vibrational modes and correlating changes in the spectra with changes in material strength (flexural or tensile) and the residual surface strain produced during processing. The primary focus of this thesis is to show the influence of various grinding methods on the residual surface stresses and the flexural strength of 6H SiC using Raman microprobe spectroscopy. It has been shown that material strength is greatly influenced by surface processing.[2] In addition, a galvanometer scanner which was installed in the Raman microprobe system at the end of this work will be described and the preliminary experimental results obtained with it will be presented.

Chapter II gives a short background and a review of the theory of Raman scattering. A discussion on the crystal lattice structures of cubic and hexagonal SiC and how residual surface stresses introduced through grinding are determined from the Raman spectrum is also given. Chapter III describes the Raman microprobe system and the acquisition and calibration of Raman spectral data using both PMT and CCD array detection systems. Chapter IV consists of three sections. The first section describes typical Raman spectra obtained from both single crystal and polycrystalline 6H SiC specimens using both detection systems. The second section covers a polarization

dependence study of the 790 cm^{-1} region Raman modes for 4H and 6H SiC single crystal specimens. Finally, the third section describes the grinding studies performed on 6H SiC specimens, including a discussion on ceramic material processing methods, the techniques used to measure the relative residual surface stresses produced by each of these processing methods, and the correlation of these measurements with flexural strength. Chapter V details the experimental results of studies performed primarily on 6H SiC specimens. These studies included the following: fluorescence studies of certain ceramic specimens; appearance of different vibrational modes due to the existence of other crystalline polytypes (4H); and studies of grinding damage profiles using different incident wavelengths. Chapter VI describes a prototype galvanometer scanner for the Raman microprobe system with consideration for computer-controlled operation. Chapter VII provides a discussion of this work with conclusions and recommendations for future research.

Calculations of the absolute power of Raman light scattered by 6H SiC for this research are given in Appendix A. Detailed listings of computer macros used to analyze the Raman data are included in Appendix B with internal documentation. Appendix C describes the wavelength dispersion linearity of spectrometers and Appendix D provides additional information on Raman tensor analysis. A discussion on weighted statistical averaging is given in Appendix E.

CHAPTER II

THEORY

The Raman Effect

The Raman effect is different from the well known Rayleigh scattering effect in which the scattered light is of the same frequency as that of the incident light. The Raman effect, by contrast, is an "inelastic" process wherein an incident photon is annihilated with the simultaneous creation of a new photon of lower or higher energy than the incident photon. In the lower energy case, the remaining energy excites the molecule or crystalline lattice to a higher vibrational and/or rotational state. This process is called Stokes scattering and is typically strongest due to the higher population of the initial state. When the initial state is above the ground state, the outgoing photon can have an energy higher than the incident photon. This process is called anti-Stokes scattering in which a molecule or lattice is left in a lower energy state. These processes are illustrated in Figure 1. The energy difference in the initial and final states represents the vibrational energy of the lattice and is reflected in a corresponding shift in the frequency of the scattered light from the incident frequency. According to scattering theory, which will be discussed later on and shown experimentally, the spectral shapes of these Raman modes are described by Lorentzian profiles given by

$$g(v) = \frac{A\left(\frac{\delta v}{2}\right)^2}{(v - v_0)^2 + \left(\frac{\delta v}{2}\right)^2} = \frac{A}{\left(\frac{v - v_0}{\delta v/2}\right)^2 + 1} = \frac{A}{4\left(\frac{v - v_0}{\delta v}\right)^2 + 1} \tag{1}$$

in which v_0 is the center frequency, A is the mode amplitude, and δv is the spectral full

width at half maximum (FWHM) of the vibrational Raman line.
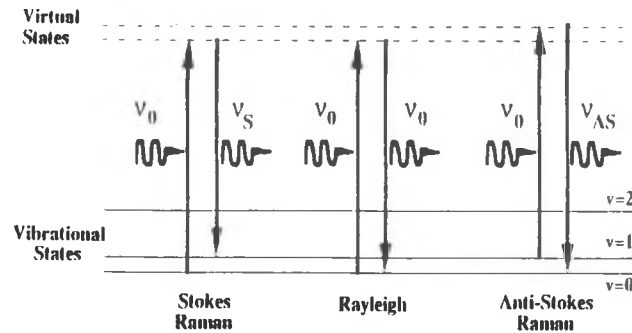
Figure 1. (a) Inelastic Raman scattering (Stokes) showing energy gain by the medium. (b) Elastic Rayleigh scattering. (c) Inelastic Raman scattering showing energy loss by the medium (anti-Stokes).

The Lorentzian profile is characteristic of resonance in the vibrational mode of the lattice.

Its lineshape is symmetric and occurs for a lattice structure of crystallites larger than

~100 nm.

The lineshape of the vibrational modes can vary in many ways depending upon the

way in which the crystallite lattice is altered. Under compressive or tensile stress, there is

a symmetry breaking causing a reduction in the symmetry of the crystallite lattice such that

splitting of the modes and the appearance of new modes can occur.[3] The characteristics of

individual modes can vary as well. The modes can shift in position away from the incident

frequency due to applied or internal stress. The compressive stresses due to grinding can

broaden the linewidth of these modes due to lowered crystal symmetry caused by these stresses and due to a large variance in the distribution of the stresses in the local vicinity.

The Raman effect can be described by considering polarizability theory. The incident electromagnetic field affects the charge distribution of a molecule or lattice periodically and induces an alternating dipole moment which radiates light, hence the Raman scattering effect. This dipole moment is given by

$$\vec{\mu} = \overleftrightarrow{\alpha} \cdot \vec{E} \tag{2}$$

in which $\overleftrightarrow{\alpha}$ is the polarizability matrix. The applied electromagnetic field is given by

$$\vec{E} = \vec{E}_0 \cos(2\pi\nu t) \tag{3}$$

The polarizability can be described by

$$\overleftrightarrow{\alpha} = \overleftrightarrow{\alpha}_0 + \sum \overleftrightarrow{\alpha}_n \cos(2\pi\nu_n t) \tag{4}$$

and consists of static and dynamic polarizabilities, $\overleftrightarrow{\alpha}_0$ and $\overleftrightarrow{\alpha}_n$, respectively, in which ν_n is the rotational or vibrational frequency of the structure. Inserting Equations (3) and (4) into Equation (1), we obtain

$$\vec{\mu} = \vec{E}_0 \cdot \overleftrightarrow{\alpha}_0 \cos(2\pi\nu t) + \tfrac{1}{2}\vec{E}_0 \cdot \sum \overleftrightarrow{\alpha}_n \{\cos 2\pi(\nu - \nu_n)t + \cos 2\pi(\nu + \nu_n)t\} \tag{5}$$

where the first, second, and third terms correspond to the Rayleigh, Stokes Raman, and anti-Stokes Raman effects, respectively. Due to the tensor nature of the polarizability, one can write the dipole moment as

$$\begin{aligned}
\mu_x &= \alpha_{xx}E_x + \alpha_{xy}E_y + \alpha_{xz}E_z \\
\mu_y &= \alpha_{yx}E_x + \alpha_{yy}E_y + \alpha_{yz}E_z \\
\mu_z &= \alpha_{zx}E_x + \alpha_{zy}E_y + \alpha_{zz}E_z
\end{aligned} \tag{6}$$

The total power radiated from an oscillating dipole moment is shown[4] from classical physics to be

$$P = N\frac{16\pi^4\nu^4}{(4\pi\varepsilon_0)\,3c^3}|\overline{\mu}|^2 \tag{7}$$

where N is the number of atoms, $\overline{\mu}$ is the time-averaged dipole moment, ν is the frequency of the radiated light, ε_0 is the electric permittivity in free space, and c is the speed of light. Equation (7) clearly indicates the presence of Raman peaks in the scattered light at the frequencies shown in Equation (5).[5] Using quantum mechanics, one can determine the Raman selection rules governing the allowable energy state transitions of a scattering medium and thus determine the allowable modes.

The Raman lines on the Stokes Raman side are more intense than their "twins" on the anti-Stokes Raman side as illustrated in Figure 2. This can be explained from the fact that the populations of the energy levels depend on the absolute temperature according to the Boltzmann distribution. The intensity ratio of the Stokes Raman lines to their corresponding anti-Stokes Raman lines is directly proportional to the ratio of the population of states in terms of the Boltzmann distribution given by[1]

$$\frac{\text{Stokes line intensity}}{\text{Anti-Stokes line intensity}} \propto \left(\frac{\nu_0 - \Delta\nu}{\nu_0 + \Delta\nu} \right)^4 \exp\left(\frac{h\,\Delta\nu}{k\,T} \right) \tag{8}$$
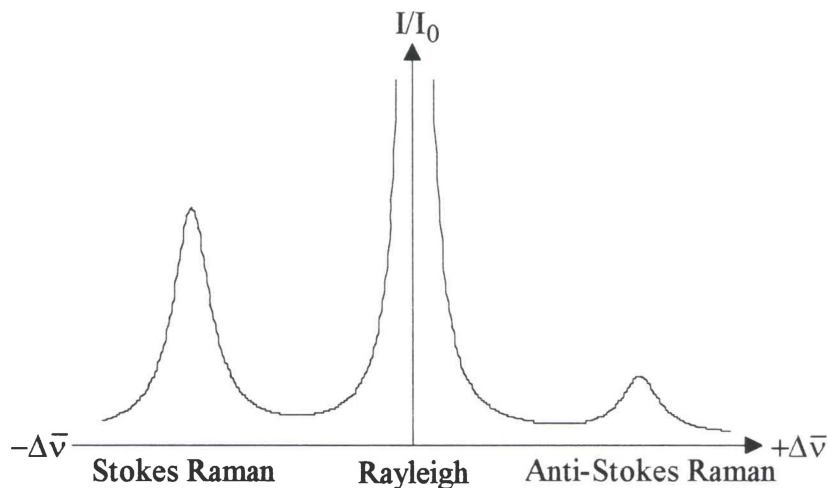
Figure 2. Comparison of the relative intensities of the Stokes and anti-Stokes Raman scattering lines.

where v_0 is the incident light frequency, Δv is the frequency shift, h is Planck's constant, k is Boltzmann's constant, and T is the absolute temperature.

The Raman shift in the Stokes Raman regime can be found using

$$\Delta\bar{v} = \left(10^8 \text{ cm}^{-1}\cdot\text{\AA}\right)\left(\frac{1}{\lambda_i} - \frac{1}{\lambda_s}\right) \tag{9}$$

where λ_i and λ_s are the incident and scattered light wavelengths, respectively, in Å and $\Delta\bar{v}$ is the Raman shift expressed in cm^{-1}. Multiplying by c gives the actual frequency shift in Hertz.

Raman Scattering in Crystals

The modes of a lattice can either be optical, acoustical, or silent (inactive). Acoustical modes are propagating modes in which atoms vibrate with adjacent atoms as in a linear elastic band. Optical modes are those modes in which neighboring atoms vibrate or rotate against each other. Optical modes can be either Raman active, infrared (IR) active, or both depending on the symmetry of the lattice. If inversion symmetry exists, then the Raman and IR modes are mutually exclusive, whereas in the absence of inversion symmetry, there is no restriction on the Raman and IR active modes. The relative strengths, however, can be quite different in the two spectra. Raman modes involve the change in polarizability which is essentially a change in the charge distribution during the vibration of a particular mode. Infrared modes are due to a change in the dipole moment with vibration. In other words, the centers of positive and negative charge displace relative to each other to form an oscillating dipole during the vibration.

For a crystalline structure with a total of N atoms containing n atoms in m molecules per unit cell, there will be $3N$ normal modes of vibration contained in $3n$ branches on the dispersion curve: $3n$-3 branches are optical modes and three are acoustic modes. All optical modes are either external or internal. External (lattice) vibrations for a crystalline structure are either translational or quasi-rotational modes of molecular groups within the lattice, whereas internal vibrations are vibrations of the atoms within a molecular group. Of the $3n$-3 optical modes, $3n$-$6m$ are internal modes and $6m$-3 are external modes. Of the $6m$-3 external (optical) modes, $3m$ are rotational modes and $3m$-3 are translational.[6] A diagram of the distribution of these modes is shown in Figure 3.
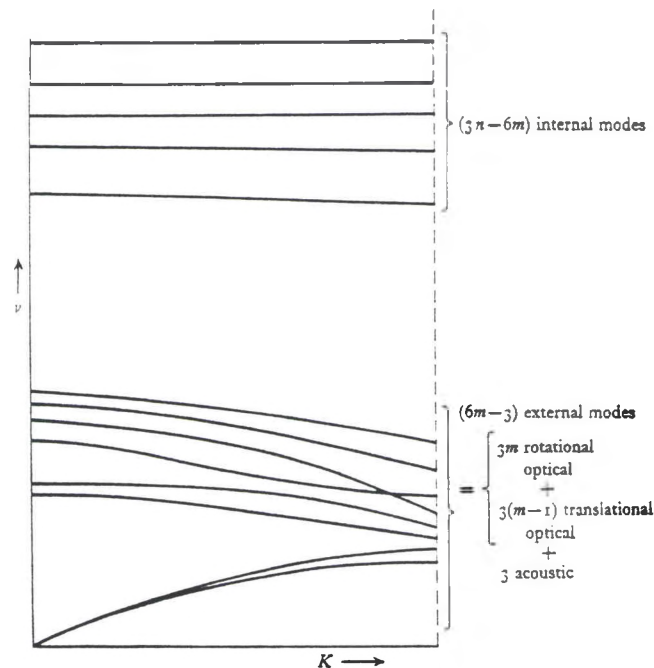
Figure 3.   Dispersion relation diagram for a molecular crystal containing n atoms in m molecules per unit cell [Reference 6].

Group theory can be used to analyze and categorize the vibrations of polyatomic molecules within a crystalline structure to simplify the complexity of this lattice dynamic. This is done by relating the selection rules for Raman scattering to the symmetry of the lattice structures and not to the forces that bind the atomic lattice together. In equilibrium, often the nuclei of these polyatomic molecules have symmetry elements such as reflection planes, rotation axes, centers of inversion, etc. Each symmetry element can be associated with a symmetry operation. These operators taken as a set define what is known as a mathematical point group. Each molecule or unique lattice site may be assigned a point group so that the normal modes of the molecule or the entire unit cell, respectively, may be analyzed using group theory. Determining the number and symmetry properties of the normal vibrations in a lattice structure involves finding its point group, obtaining the symmetry operations and irreducible representations, and finally associating the normal vibrations with each irreducible representation. Table 1 shows a list of point groups compiled by Sherwood.[6] The general notations for vibrations are A (symmetric), B (antisymmetric), E (doubly degenerate), and F (triply degenerate).[1]

The polarizability of a molecule from Equation (2) can be expanded by considering the displacement vector $\Delta q_n(t)$ as it vibrates at frequency ω_l using

$$\alpha_{ij}(t) = \alpha_{ij} + \sum_k \left. \frac{\partial \alpha_{ij}(t)}{\partial q_k(t)} \right|_{\Delta q_{ij}=0} \Delta q_{ij}(t) + \ldots \tag{10}$$

The first order term is responsible for Rayleigh scattering, whereas the second order term causes birefringence and the Pockel's effect in addition to the Raman effect. Assuming only the kth component is non-zero, the polarizability can be described by

$$\alpha_{ij}(t) = \alpha_{ij} + (\nabla_k \alpha_{ij}) q_k \cos(\omega_1 t + \beta) \tag{11}$$

where the component of the change in polarizability with respect to the change in displacement of the nuclei is given by

$$\nabla_k \alpha_{ij} = \frac{\partial \alpha_{ij}}{\partial q_k} \qquad (12)$$

Table 1. Mode symmetry groupings and symmetry elements.[a]

Classification on basis of optical refraction	Systems	Class		Symmetry elements
		International	Schönflies	
Anisotropic — Biaxial	Triclinic	$\bar{1}$	C_1	E
		$\overline{\bar{1}}$	C_i	$E\ i$
	Monoclinic	m	C_s	$E\ \sigma_h$
		2	C_2	$E\ C_2$
		$2/m$	C_{2h}	$E\ C_2\ i\ \sigma_h$
	Orthorhombic	$2mm$	C_{2v}	$E\ C_2\ \sigma'_v\ \sigma''_v$
		222	D_2	$E\ C_2\ C'_2\ C''_2$
		mmm	D_{2h}	$E\ C_2\ C'_2\ C''_2\ i\ \sigma_h\ \sigma'_v\ \sigma''_v$
Anisotropic — Uniaxial	Tetragonal	$\bar{4}$	C_4	$E\ 2C_4\ C_2$
		$\overline{4}$	S_4	$E\ 2S_4\ C_2$
		$4/m$	C_{4h}	$E\ 2C_4\ C_2\ i\ 2S_4\ \sigma_h$
		$\underline{4}mm$	C_{4v}	$E\ 2C_4\ C_2\ 2\sigma'_v\ 2\sigma_d$
		$\overline{4}2m$	D_{2d}	$E\ C_2\ C'_2\ C''_2\ 2\sigma_d\ 2S_4$
		422	D_4	$E\ 2C_4\ C_2\ 2C'_2\ 2C''_2$
		$4/mmm$	D_{4h}	$E\ 2C_4\ C_2\ 2C'_2\ 2C''_2\ i\ 2S_4\ \sigma_h\ 2\sigma'_v\ 2\sigma_h$
	Rhombohedral (Trigonal)	3	C_3	$E\ 2C_3$
		$\bar{3}$	S_6	$E\ 2C_3\ i\ 2S_6$
		$3m$	C_{3v}	$E\ 2C_3\ 3\sigma_v$
		32	D_3	$E\ 2C_3\ 3C_2$
		$\bar{3}m$	D_{3d}	$E\ 2C_3\ 3C_2\ i\ 2S_6\ 3\sigma_d$
	Hexagonal	$\bar{6}$	C_{3h}	$E\ 2C_3\ \sigma_h\ 2S_3$
		6	C_6	$E\ 2C_6\ 2C_3\ C_2$
		$6/m$	C_{6h}	$E\ 2C_6\ 2C_3\ C_2\ i\ 2S_3\ 2S_6\ \sigma_h$
		$\bar{6}m2$	D_{3h}	$E\ 2C_3\ 3C_2\ \sigma_h\ 2S_3\ 3\sigma_v$
		$6mm$	C_{6v}	$E\ 2C_6\ 2C_3\ C_2\ 3\sigma_v\ 3\sigma_d$
		622	D_6	$E\ 2C_6\ 2C_3\ C_2\ 3C'_2\ 3C''_2$
		$6/mmm$	D_{6h}	$E\ 2C_6\ 2C_3\ C_2\ 3C'_2\ 3C''_2\ i\ 2S_3\ 2S_6\ \sigma_h\ 3\sigma_d\ 3\sigma_v$
Isotropic	Cubic	23	T	$E\ 4C_3\ 4C_3^2\ 3C_2$
		$m3$	T_h	$E\ 4C_3\ 4C_3^2\ 3C_2\ i\ 8S_6\ 3\sigma_h$
		$\bar{4}3m$	T_d	$E\ 8C_3\ 3C_2\ 6\sigma_d\ 6S_4$
		432	O	$E\ 8C_3\ 3C_2\ 6C'_2\ 6C_4$
		$m3m$	O_h	$E\ 8C_3\ 3C_2\ 6C_2\ 6C_4\ i\ 8S_6\ 3\sigma_h\ 6\sigma_d\ 6S_4$

[a] Reference 6.

This expression is one element of the 3 x 3 matrix representing the change in polarizability. It can be used to find the number and polarization properties of the modes that can appear. Collectively, the elements defined by Equation (12) can be expressed in a reduced form as a Raman matrix whose elements are proportional to the change-in-polarizability matrix. The Raman irradiance, excluding temperature-dependent factors, is given by[6]

$$I(\Gamma_j) \propto (v_0 \pm v_j)^4 \sum_j \left| \vec{e_s} \cdot \overleftrightarrow{R} (\Gamma_j) \cdot \vec{e_i} \right|^2 \tag{13}$$

where $\overleftrightarrow{R}$ is the Raman tensor. The vectors $\vec{e_i}$ and $\vec{e_s}$ are the incident and scattered polarizations, respectively. The Γ_j term is the jth irreducible representation of the point group.

Raman Wavevector Propagation in Crystals

The frequency shift in the Raman effect is depicted through conservation of momentum in Figure 4 showing a single photon incident on a crystal. Note that the incident and scattered photon propagation directions are arbitrarily oriented. In practice, the angle between these two directions is typically 90° or 180°. The 180° configuration is referred to as the 180° backscattering geometry and was used for this research. In addition, the incident and scattered polarizations may be selected to determine the Raman active modes which appear, according to Equation (13). In Figure 4, the incident photon of wavevector $\vec{k_i}$ is annihilated and a scattered photon of wavevector $\vec{k_s}$ and a phonon of wavevector $\vec{q}$ are created. Thus, momentum conservation requires

$$\vec{k_i} = \vec{k_s} + \vec{q} \tag{14}$$

Thus, for the 180° backscattering geometry, the wavevectors $\vec{k}_i$, $\vec{k}_s$, and $\vec{q}$ are collinear. The direction of the phonon determines the modes of oscillation observed. The maximum value for the phonon wavevector $\vec{q}$ is simply $\left|\vec{q}\right|_{max} = \frac{2\pi}{a}$, where a is the lattice constant.
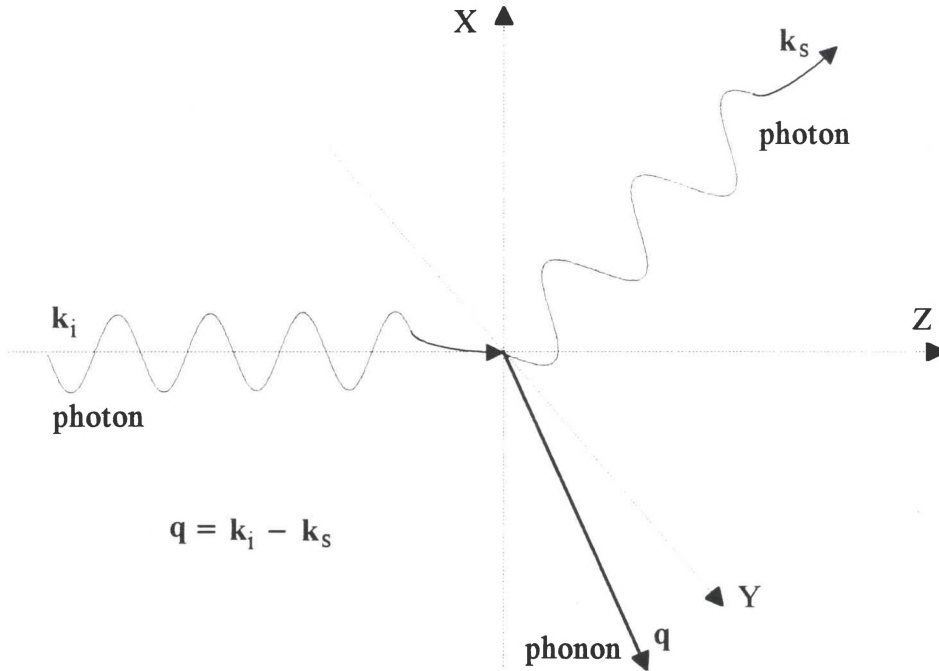
Figure 4. Wavevector conservation in Raman scattering.

This value defines the Brillouin zone boundaries of the dispersion relation for a diatomic lattice structure such as SiC, as shown in Figure 5. There are two branches for this dispersion relation: an optical branch and an acoustic branch. Since $\left|\vec{k}_i\right|$ and $\left|\vec{k}_s\right|$ are small in comparison to $\left|\vec{q}\right|_{max}$ (λ_i and λ_s are much larger than a), then, from Equation (14), $\left|\vec{q}\right|$ is very near zero, near the center of the Brillouin zone.

Many crystals are anisotropic, meaning that their optical properties aren't equivalent in all directions. Uniaxial crystals have one optic axis (c-axis) to which all symmetry properties are assigned. The crystalline axis (c-axis) is usually assigned the z axis as its symmetry axis. Lattice vibrations parallel to the phonon propagation direction

are longitudinal (L) modes, while those perpendicular to this direction are known as transverse (T) modes. In some cubic crystals, the T and L modes are degenerate.
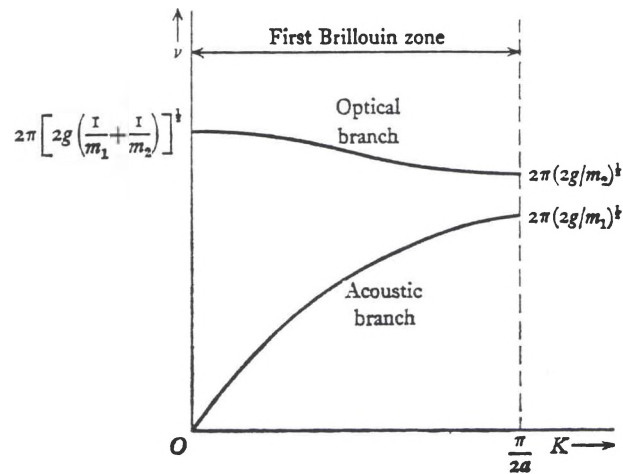
Figure 5. Dispersion relation of an infinite one-dimensional diatomic lattice structure in the first Brillouin zone. The frequencies at the zone boundaries are shown for $m_1 > m_2$ in which m_1 and m_2 are the atomic masses and g is the second derivative of the interatomic potential function [Reference 6].

The electromagnetic radiation interacting with a crystalline medium is composed of oscillating fields, both magnetic and electric, which, in isotropic media, are perpendicular to each other and to the direction of propagation. The electric field is used to define the polarization of the radiation. The field can be decomposed into vertical and horizontal components of polarization. The ratio and phases of these components determine the type and degree of polarization of the radiation. The polarization of the exciting light determines the nature of the excited Raman modes in the crystal. Thus, analysis of individual modes can be performed simply by selecting the polarization of the incident and scattered light.[6]

This polarization dependence of vibrational modes is discussed by Sherwood[6] for cubic and uniaxial crystals. Long range electrostatic forces give rise to longitudinal-transverse splitting in polar cubic crystals. Polar crystal structures have electric dipole moments associated with their vibrational modes. In uniaxial crystals, short range atomic forces must also be considered since they produce anisotropy in the force constants. Variations in the relative magnitudes of these two forces can cause changes in the nature of the vibrational modes. The vibrational frequencies parallel and perpendicular to the c-axis are denoted by $\nu_{\parallel}$ and $\nu_{\perp}$, respectively.

Figure 6 shows phonons in the x-y plane excited by radiation propagating in the plane.
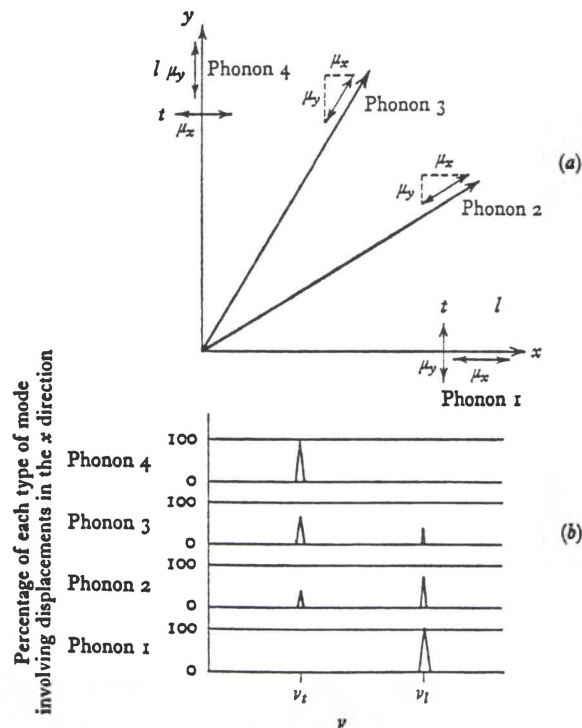
Figure 6. (a) The polarization of phonons propagating in the x-y plane of a uniaxial (or cubic) crystal for incident light in the x-y plane assuming that longitudinal-transverse splitting is much greater than short range crystal anisotropy (for a uniaxial crystal). (b) Resolution into longitudinal and transverse phonons that involve displacements in the x direction [Reference 6].

If the short range forces are much greater than the longitudinal-transverse splitting, then these forces act to confine propagation along one of the crystal axes. This effect causes the wave to have a mixed transverse and longitudinal mode. Taking θ as the angle $\vec{q}$ makes with respect to the c-axis, the mixed phonon frequencies in the x-z plane, which contains the c-axis, are given by

$$\nu_{\parallel}^2 = (\nu_{\parallel T})^2 \sin^2\theta + (\nu_{\parallel L})^2 \cos^2\theta \tag{15}$$

where $\nu_{\parallel T}$ and $\nu_{\parallel L}$ are the frequency components of vibrations parallel to the c-axis which are decomposed along directions perpendicular and parallel to the phonon propagation direction, respectively. The mixed phonon frequencies in the x-y plane are given by

$$\nu_{\perp}^2 = (\nu_{\perp T})^2 \cos^2\theta + (\nu_{\perp L})^2 \sin^2\theta \tag{16}$$

where $\nu_{\perp T}$ and $\nu_{\perp L}$ are the frequency components of vibrations perpendicular to the c-axis which are decomposed along the directions perpendicular and parallel to the phonon propagation direction, respectively. If, for example, $\nu_{\perp T}$ and $\nu_{\parallel T}$ are Raman active based on group theory selection rules, then the mixed modes represented by Equations (15) and (16) will appear in the Raman spectrum.

If the short range forces are much smaller than the long range electrostatic forces, then phonons in the x-y plane will resolve into longitudinal and transverse modes as shown in Figure 6, but phonons propagating in the x-z plane will be mixed. These phonon modes will be mixtures of $\nu_{\perp}$ and $\nu_{\parallel}$ components for both the transverse and longitudinal cases, as demonstrated in Figure 7. The transverse frequency is given by

$$\nu_T^2 = (\nu_{\parallel T})^2 \sin^2\theta + (\nu_{\perp T})^2 \cos^2\theta \tag{17}$$

and the longitudinal frequency is given by

$$\nu_L^2 = (\nu_{\parallel L})^2 \cos^2\theta + (\nu_{\perp L})^2 \sin^2\theta \tag{18}$$

From Equations 15-18, it is possible to find the orientation of the crystal axis from Raman spectral data.
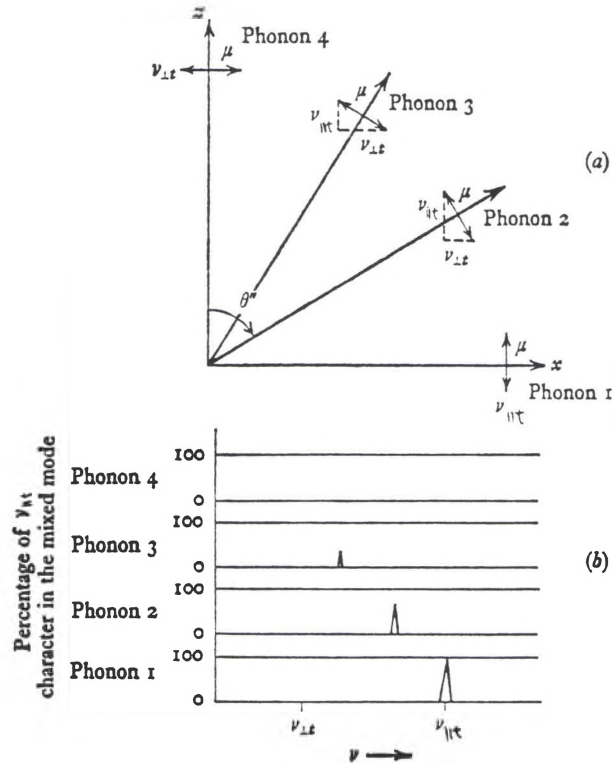
Figure 7. (a) The polarization of transverse phonons propagating in the x-z plane of a uniaxial crystal for incident light polarized parallel and perpendicular to the c-axis assuming that short range crystal anisotropy is much greater than longitudinal-transverse splitting. (b) The frequency of the mixed modes of $\nu_{\perp T}$ character [Reference 6].

Cubic and Hexagonal Silicon Carbide

Silicon carbide has a number of different polytype structures which differ in the stacking arrangements of hexagonal planes along the c-axis called close packing.[7] Silicon carbide occurs in nature as cubic, hexagonal, or rhombohedral structures. This thesis is concerned primarily with hexagonal polytypes, but the cubic structure was also considered. In the Ramsdell structural notation of crystals, here represented by nA, the letter A represents the type of crystalline structure. Cubic, hexagonal, and rhombohedral

structures are denoted by C, H, and R, respectively. The n indicates the number of stacked double layers per unit cell. The cubic form of SiC is also referred to as β-SiC whereas the hexagonal forms of SiC are referred to collectively as α-SiC. The cubic lattice of this diatomic molecular structure forms a face-centered-cubic (fcc) structure of cations and another one of anions in which the two fcc structures are displaced by one-fourth of the unit cell body diagonal, as shown in Figure 8.[8]
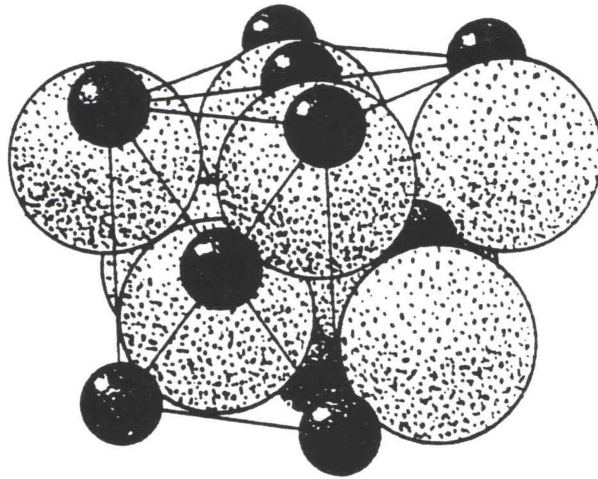
Figure 8. A face-centered-cubic lattice represented by ZnS [Reference 8].

This arrangement is also known as a ZnS arrangement or a zinc blende structure. This cubic structure has T_d^2 point group symmetry, the 2 referring to the particular space group. The unit cell coordinates (a, b, c) of the atomic nuclei in fractions of the lattice parameters are described by

$$R: 0\ 0\ 0;\ 0\ \tfrac{1}{2}\ \tfrac{1}{2};\ \tfrac{1}{2}\ 0\ \tfrac{1}{2};\ \tfrac{1}{2}\ \tfrac{1}{2}\ 0$$
$$X: \tfrac{1}{4}\ \tfrac{1}{4}\ \tfrac{1}{4};\ \tfrac{1}{4}\ \tfrac{3}{4}\ \tfrac{3}{4};\ \tfrac{3}{4}\ \tfrac{1}{4}\ \tfrac{3}{4};\ \tfrac{3}{4}\ \tfrac{3}{4}\ \tfrac{1}{4} \qquad (19)$$

where R is the cation and X is the anion.

The hexagonal lattice, represented by Figure 9, demonstrates the hexagonal-close-packed (hcp) structure.
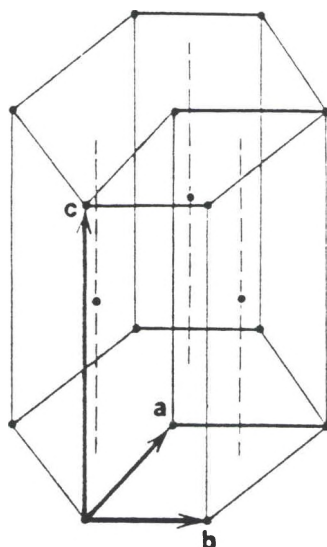
Figure 9. The hexagonal-close-packed (hcp) structure with primitive unit cell [Reference 7].

Notice that the cell consists of three smaller primitive unit cells. A diatomic molecular structure like SiC is represented in Figure 10.
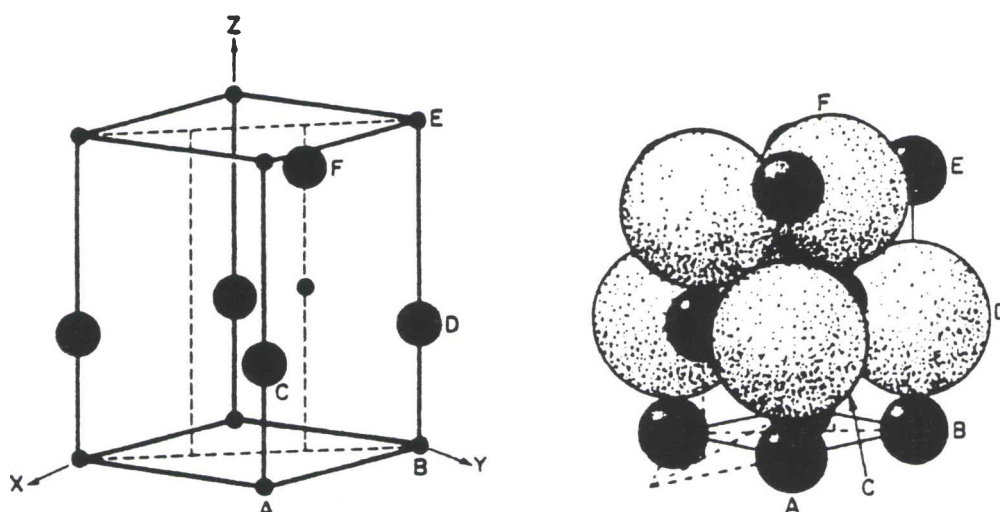
Figure 10. A hexagonal structure represented by ZnO [Reference 8].

This figure depicts ZnO and is often referred to as a Wurtzite structure.[9] The hexagonal unit cell has C_{6v}^4 point group symmetry, where the *6* means it has 6-fold rotational symmetry about the c-axis and the *v* means that its vertical reflection planes contain the c-axis. The superscript *4* indicates the space group with which it is associated. If the diatomic structure is close-packed and the anions and cations are of equal radius, then the packing efficiency, assuming that the atoms are hard spheres, is equivalent to that of diamond, 34% by volume. A drawing of a hexagonal-close-packed (hcp) arrangement of spheres in a layer is shown in Figure 11.
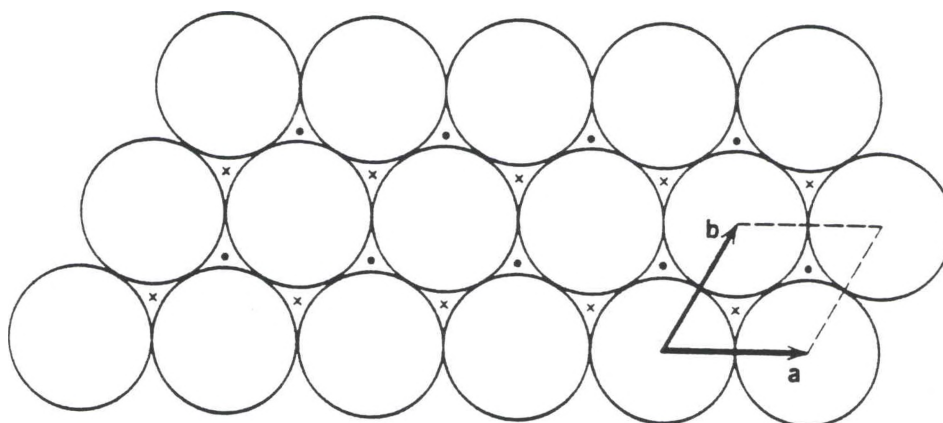
Figure 11. A layer of spheres in the plane of a close-packed hexagonal lattice. One set of wells is marked by dots and the other set is marked by crosses. The base of the hexagonal primitive unit cell is also shown [Reference 7].

If, during stacking, the third layer spheres lie above spheres of the first layer, a local hcp structure is formed, whereas if the third layer spheres lie above the empty "wells" in the first layer, a fcc structure is formed. For the fcc structure, the layer of Figure 11 cuts obliquely across the unit cell cube so that three local spheres lie at a cube corner and two neighboring face centers, respectively, as shown in Figure 12.

Figure 13 demonstrates the stacking arrangements for several SiC polytypes. In diatomic SiC, the C atom hexagonal structure is displaced from the Si atom hexagonal structure along the direction perpendicular to the stacking planes. This vertical axis is the c-axis of the crystal.
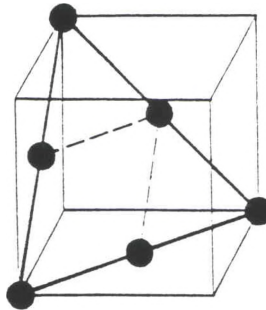
Figure 12. A close packed plane in the fcc structure. Only those atoms in the plane are shown. A two-dimensional hexagonal cell is also depicted [Reference 7].

(For 6H SiC, this displacement is 1/8 of the vertical cell dimension.) Together the Si and C atoms form a vertical series of double layers (in 6H SiC, there are six double layers per unit cell height).
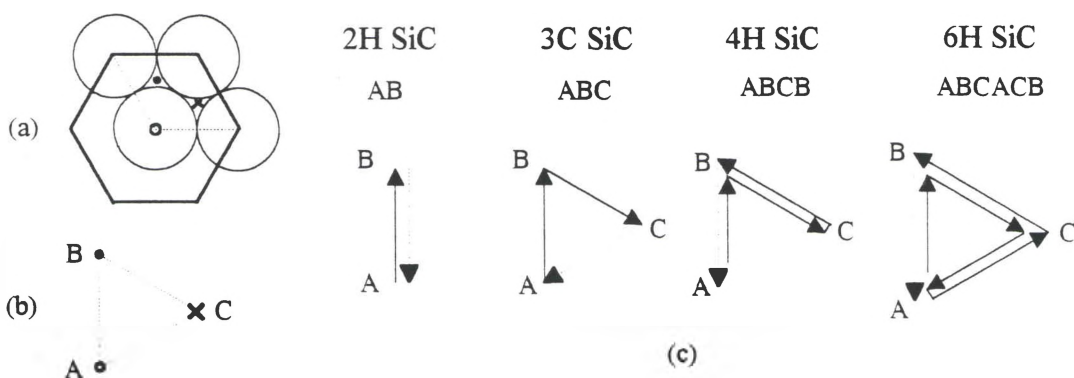
Figure 13. Stacking pattern for several SiC polytypes: (a) base of hexagonal pseudocell with a dashed primitive cell inset (b) stacking triangle formed by center sphere A and well positions B and C of the primitive cell (c) some polytype stacking patterns representing planar displacement of each double layer relative to the first double layer as the layers are stacked vertically.

Each Si atom is surrounded by four C atoms in a tetrahedral formation (and vice versa). The cubic (β) form of SiC has 3 molecules and 3 double layers in its hexagonal pseudocell with a cell width of 3.073 Å and a cell height of 7.57 Å. (In Cartesian coordinates, the fcc cell has a cell dimension of 4.348 Å and contains four molecules.) In contrast, 6H SiC has 6 molecules and 6 double layers per hexagonal pseudocell with cell width and height dimensions of 3.073 Å and 15.08 Å, respectively.[8] The β (or 3C) SiC unit cell coordinates (a, b, c) in fractions of the hexagonal primitive cell dimensions are given by

$$\text{Si: } 0\ 0\ 0;\ \tfrac{1}{3}\ \tfrac{2}{3}\ \tfrac{1}{3};\ \tfrac{2}{3}\ \tfrac{1}{3}\ \tfrac{2}{3}$$
$$\text{C: } 0\ 0\ \tfrac{1}{4};\ \tfrac{1}{3}\ \tfrac{2}{3}\ \tfrac{7}{12};\ \tfrac{2}{3}\ \tfrac{1}{3}\ \tfrac{11}{12} \tag{20}$$

The 6H SiC unit cell coordinates (a, b, c) in fractions of the hexagonal primitive cell dimensions are given by[8]

$$\text{Si: } 0\ 0\ 0;\ \tfrac{1}{3}\ \tfrac{2}{3}\ \tfrac{1}{6};\ \tfrac{2}{3}\ \tfrac{1}{3}\ \tfrac{1}{3};\ 0\ 0\ \tfrac{1}{2};\ \tfrac{2}{3}\ \tfrac{1}{3}\ \tfrac{2}{3};\ \tfrac{1}{3}\ \tfrac{2}{3}\ \tfrac{5}{6}$$
$$\text{C: } 0\ 0\ \tfrac{1}{8};\ \tfrac{1}{3}\ \tfrac{2}{3}\ \tfrac{7}{24};\ \tfrac{2}{3}\ \tfrac{1}{3}\ \tfrac{11}{24};\ 0\ 0\ \tfrac{5}{8};\ \tfrac{2}{3}\ \tfrac{1}{3}\ \tfrac{19}{24};\ \tfrac{1}{3}\ \tfrac{2}{3}\ \tfrac{23}{24} \tag{21}$$

Illustrations of these two configurations are shown in Figure 14. The covalent radii of Si and C are 1.17 Å and 0.77 Å, respectively.[10] The lengths of the Si-Si and the C-C molecular bonds are both 3.09 Å and the length of the Si-C molecular bonds is 1.89 Å.[8]

Feldman et al., in a 1968 paper,[9] presented a detailed study of Raman scattering in 6H SiC in which they confirmed much of their Raman mode predictions experimentally. Polytype 6H has 12 atoms per unit cell (6 molecules) with 33 long wavelength optical modes ($3N$-3). Of these modes, 18 are quasi-rotational and 15 are translational. The normal modes for the structure are $6(A_1+B_1+E_1+E_2)$ of which three are acoustical.
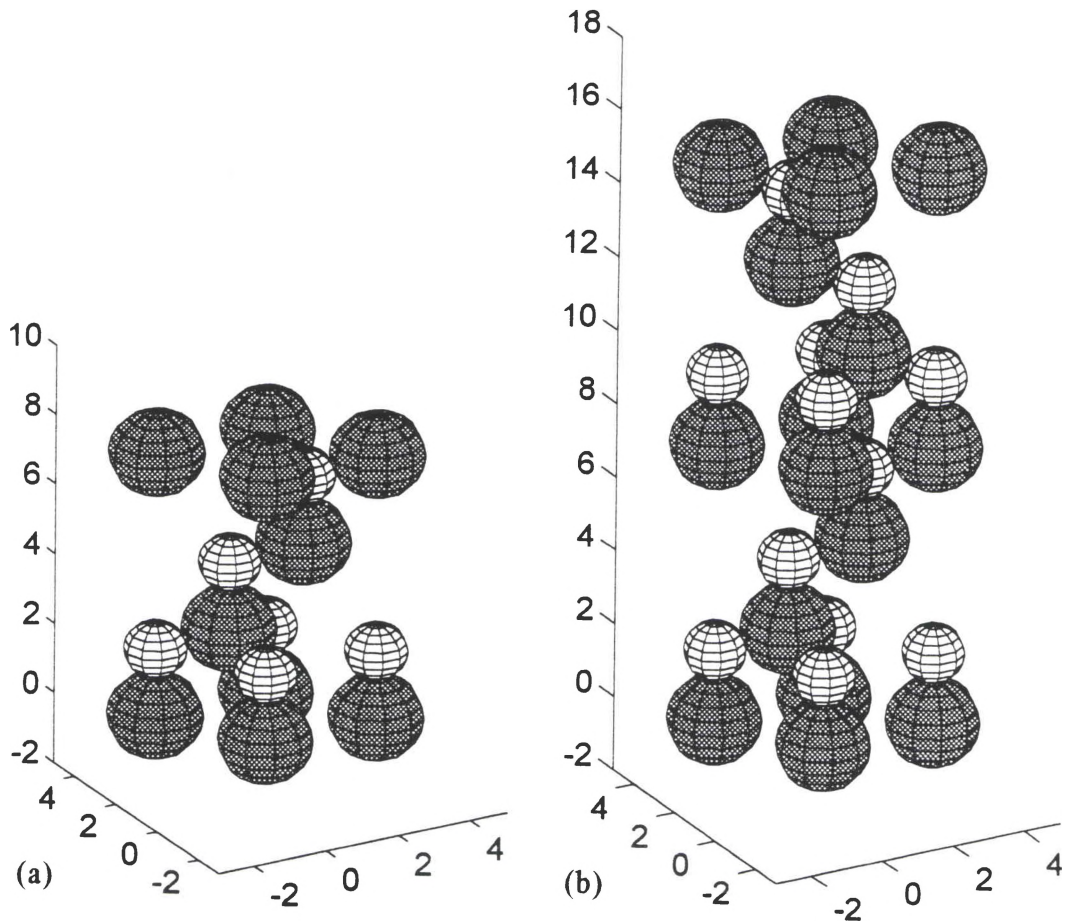
Figure 14. Diagrams of (a) 3C and (b) 6H SiC polytype primitive cell structures. The large atoms are Si and the small atoms are C. The units are in Å.

As mentioned previously, the dominance of a long range field or short range crystal anisotropy determines the grouping of optical modes in polar uniaxial crystals. Strong modes appear when the long range electrostatic force is much greater than crystal anisotropic forces. Weak modes appear when the opposite is true. Strong modes are often two orders of magnitude more intense than weak modes in Raman spectra. The strong modes are of a mixed symmetry type like (A_1+E_1) in 6H SiC where there is a large frequency separation in the transverse and longitudinal modes due to the long range field. The weak modes, on the other hand, are either axial (parallel) or planar (perpendicular)

with respect to the c-axis and have a large frequency separation due to crystal anisotropy, yet contain mixed longitudinal-transverse components.[9]

Due to the linear stacking of the hexagonal planes in 6H SiC (C_{6v}^{4}), the large zone of the dispersion curve extends only along the axial direction of the unit cell (parallel to the c-axis). The large zone contains all of the long wavelength modes along this direction and ends at $\frac{6\pi}{a}$, where a is the lattice vector. Since $\frac{2\pi}{a}$ is the reciprocal lattice vector, the pseudomomentum vectors q=0, $\frac{2\pi}{a}$, $\frac{4\pi}{a}$, and $\frac{6\pi}{a}$ are the same as q=0 in the Brillouin zone. The momentum scale can then be reduced to a range x from 0 to 1 having values in which Raman measurements can be made at x=0, 0.33, 0.67, and 1. Table 2 shows the distribution and symmetry type of the phonon modes of 6H SiC.

Table 2. Distribution and symmetry type of 6H SiC phonon modes.[a]

Branch	x=0.00	x=0.33	x=0.67	x=1.00
Axial Optic	A_1	--	$2 A_1$	--
Planar Optic	E_1	$2 E_2$	$2 E_1$	E_2

[a] Reference 9.

The strong modes occupy x=0. The other modes in which x≠0 are weak. The A_1 modes exist at x=0 or x=0.67 on the axial optic branch. The E_1 modes also exist at x=0 or x=0.67, but fall on the planar optic branch. The E_2 modes belong to the planar optic branch at x=0.33 or x=1. The B_1 modes (antisymmetric and represented by dashes) are not observed in either Raman or infrared measurements.[9]

CHAPTER III

EXPERIMENTAL SETUP AND TECHNIQUES

Experimental Setup

The laser Raman microprobe used for this research was designed and built by P. P. Yaney and former graduate students at the University of Dayton. Currently, two lasers can be used as sources in the setup shown in Figure 15.
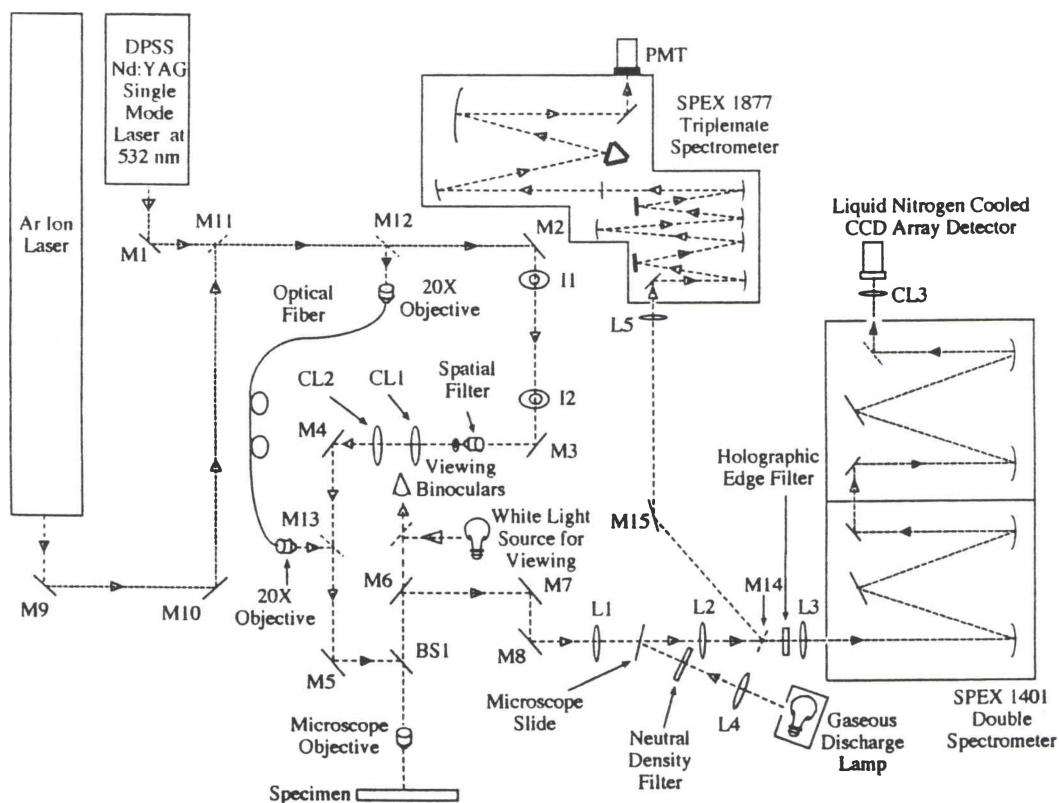
Figure 15. Laser Raman microprobe experimental setup (M=mirror, L=lens, CL=cylindrical lens, and BS=beam splitter).

25

Primarily, a continuous wave (cw) diode-pumped solid-state (DPSS) frequency-doubled neodymium:yttrium aluminum garnet (Nd:YAG) single-mode laser operating at 532 nm was used for incident light on a specimen due mainly to its narrow bandwidth (<2 MHz). This laser had a power of about 50 mW (measured at 49.4 mW upon reflection from two high-reflectance mirrors). It replaced a pulsed Nd:YAG used in past years. The other laser used was a cw Ar ion laser which can generate up to 2 W of radiant power. It has discrete wavelength selection capability in the range of 458 nm to 514.5 nm, with the strongest lines at 488 nm and 514.5 nm. These inhomogeneously broadened lines have widths of about 6 GHz for multi-longitudinal-mode operation. Wavelength selection is achieved by using a prism within the laser cavity for chromatic dispersion of the light. A wavelength may then be selected by tilting the cavity mirror accordingly. An etalon may also be used to narrow the line's spectral width to about 3 MHz for single-longitudinal-mode operation.

Upon reflection from mirrors M1 and M2, the beam from the Nd:YAG passes through the irises I1 and I2 used for alignment. After passing the beam through a spatial filter assembly, a 15 mm cylindrical lens CL1 is located slightly more than 15 mm from the spatial filter so that when the final microscope objective is focused at infinity and the corresponding image appears at the specimen surface, the laser beam is slightly defocused along the orientation of the 15 mm cylindrical lens. A second cylindrical lens having a 40 mm focal length, CL2, is located exactly 40 mm from the spatial filter and positioned transverse to the orientation of CL1 so that the final microscope objective sharply focuses the beam at the specimen surface along the orientation of CL2. This cylindrical lens

combination and final microscope objective, in effect, produce a narrow elliptical line of laser light on the specimen surface.

The purpose of a line of laser light rather than a circular spot is twofold. First, it integrates out the variations in spectral features along the length of the line. Thus, by making multiple measurements at non-overlapping locations on the specimen surface, the resulting mean values of the spectral parameters (e.g., Raman shift and linewidth) are characteristic of a microscopically-significant area of the specimen surface. Second, the use of a line greatly reduces the laser irradiance at the specimen surface. The typical laser power at the surface using a 35 μm x 2 μm elliptical line of laser light is about 7.1 mW, giving an irradiance of about 13 kW/cm^2. For a 2 μm diameter spot produced using the fiber optic system, the power at the surface is typically 2.4 mW, giving an irradiance of about 76 kW/cm^2, a six-fold increase. The use of line illumination removes the problem of laser heating of the specimen surface which can result in melting the surface or thermally perturbing the Raman spectrum.

By inserting mirror M11 between mirrors M1 and M2, the Ar ion laser may be used instead. By adding mirrors M12 and M13 to the system, an alternate path for the beam is used to substitute an optical fiber for the cylindrical optics in order to focus a laser "dot" onto the specimen. This path consists of launching the light into a single-mode, polarization-preserving fiber using a 20x objective and collimating the exiting light from the fiber using another 20x objective. The path reenters the system using mirror M13. After reflection from mirror M5, the light is reflected downward from beam splitter BS1 (70/30 transmission/reflection) in a 180° backscattering geometry. The incident laser line

(or spot) is focused onto the specimen by a microscope objective which is typically a 60x extra-long-working-distance (ELWD) objective having a 0.7 numerical aperture. The scattered and reflected light is collected by the microscope objective and transmitted through the beam splitter to the spectrometer. Lenses L1 and L2 (200 mm focal lengths) provide a secondary focus of the reflected laser light which can be used to excite an internal Raman source for wavelength calibration. In this work, a microscope slide was used to introduce the emission spectrum from a gaseous discharge lamp into the spectrograph for calibration. Lens L4 (64 mm focal length) images the lamp tube onto the slide with a magnification of about four (the object-to-image distance is about 40 cm). A neutral density filter of 1.4 O.D. (T=3.9%) was used to attenuate the lamp emission intensity. Viewing binoculars are provided to examine the focus of the laser line (or spot) on the specimen surface. A white light source, S1, with a diffuser is used to illuminate the surrounding specimen surface in order to determine the quality of focus on the specimen surface and to observe the local structure and the surface flaws which could affect the quality of the measurements. A Corning C. S. No. 3-66 sharp-cut colored glass filter is used to properly attenuate the scattered radiation on the specimen surface for safe viewing. A Physical Optics Corp. RHE 532.1D holographic edge filter is used to reject light at 532 nm at normal incidence. An additional benefit is that this filter may reject light of other wavelengths by rotating the filter (for instance, when using the Ar ion laser).

Lens L3 is a 50 mm camera lens used to focus the light onto the entrance slit of the Spex 1401 double spectrometer, which has a focal length of 0.85 m and uses two 1200 lines/mm reflection gratings blazed at 500 nm. If single-channel PMT detection is

desired, mirror M14 is placed between lenses L2 and L3 to send and focus the light via mirror M15 and lens L5 onto the entrance slit of a Spex 1877 0.6 m Triple Spectrometer to which the PMT is attached. The grating scan is motor driven and computer-controlled via a SPEX CD2A Compudrive unit. The PMT detection system is used mainly for taking spectral survey scans of specimens.

The data from both the CCD and PMT detection systems were analyzed using Igor Pro 2.0 software package on an accelerated Macintosh IIsi computer. This package is very versatile and allows the creation of functions and macros for experimental procedures in analyzing and graphing data. Function and macro procedures were designed to calibrate the data and perform statistical curve fits for determining characteristic parameters of Raman lines such as Raman shift, linewidth, and relative strength. These procedures are listed in Appendix B.

Approaches Used in Acquiring and Calibrating Spectral Data

PMT Detection System

When trying to determine the Raman modes of interest for a particular solid material, it is useful to initially scan a broad range of the spectrum (e.g., 100 cm^{-1} to 1000 cm^{-1}). Referring to Figure 15, mirrors M9 and M10 and lens L5 collect the scattered light onto the entrance slit of the Spex 1877 0.6 m Triple Spectrometer for dispersion and detection of the Raman signal. The thermoelectrically cooled (-30° C) Hamamatsu R943-02 PMT converts photons to an amplified signal which was fed into a photon counter and finally sent to a computer using data acquisition hardware and software. This

PMT has a GaAs photocathode with a dark count of about 10 cps (at -20° C).[11] The spectral range of the photocathode is 160 to 930 nm with optimum sensitivity over the range of 300 to 800 nm.[11] The CD2A Compudrive Unit controls the scan of the 1200 lines/mm grating and was usually scanned in increments of 0.1 Å (0.35 cm^{-1} at 532 nm). The initial slit leads to a subtractive double spectrometer which functions as a pre-filter and which is used to reject light such as the incident laser wavelength outside of its passband. The entrance slit width and height were typically 0.5 mm and 2 mm, respectively. The middle slit of the pre-filter was typically opened all the way to 8 mm to give a 45 nm passband. Finally, the entrance and exit slits of the "third" dispersing spectrometer were usually set to the same width, typically between 100 and 200 μm. The PMT was operated at 1600 V. The collected data were calibrated using known spectral emission lines from gaseous discharge lamps such as mercury and calibrated laser lines. This was done prior to the experiments by making a calibration curve to correct the Compudrive unit wavelength reading to actual wavelength.

The Spex 1877 Triplemate Spectrometer used for survey scans of specimens was calibrated using the 488 nm and 514.5 nm Ar ion laser lines and the 546.1 nm Hg atomic line. The calibration was also used to determine the Nd:YAG 532 nm wavelength. Four short 0.4 nm scans of each line were made in increments of 0.01 nm with a one second exposure time and 5 μm spectrometer entrance/exit slit widths, with the exception of the Hg line in which 15 μm entrance/exit slit widths were used. All three laser lines were properly attenuated to avoid saturating the PMT detector. The light from the three laser lines was focused onto tetragonal ZrO_2 powder with the 60x ELWD microscope objective

since this powder is a good scatterer and produces minimal Raman signal. The results of this study are shown in Figure 16. Note the determined wavelength of the Nd:YAG laser. Later spectral data obtained using the PMT detection system were adjusted according to the calibration of this study.
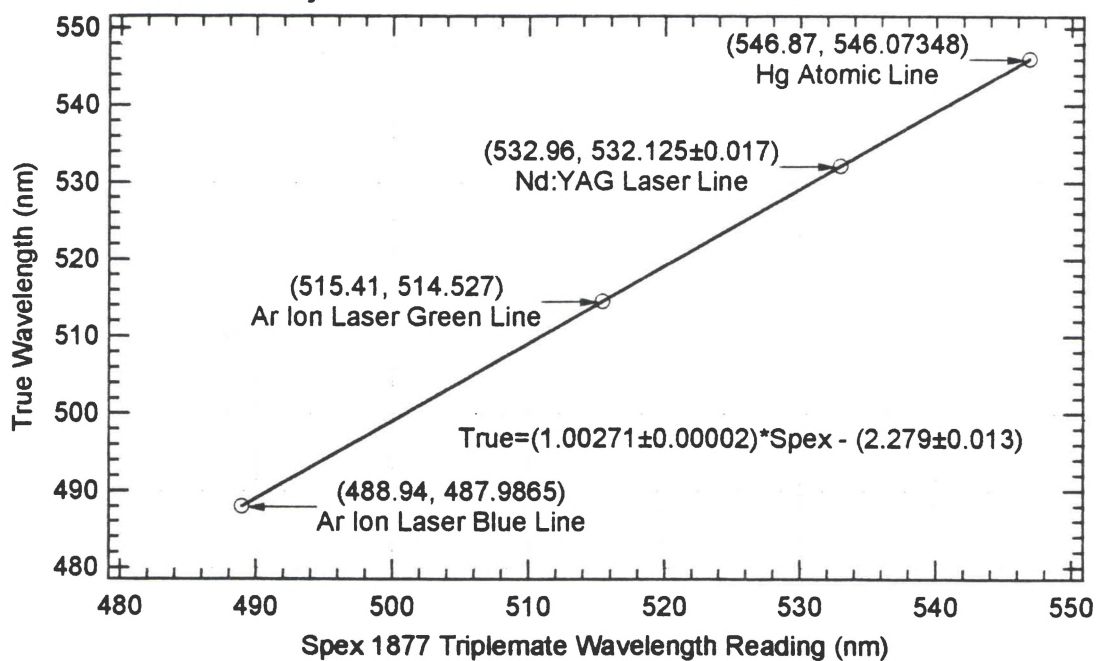
Figure 16. Calibration curve of the Spex 1877 Triplemate Spectrometer. The (x, y) paired coordinates designate the Spex 1877 wavelength reading (Spex) and the actual wavelength (True), respectively. The Nd:YAG laser wavelength was computed based on the linear regression of the data from the two Ar ion lines and the Hg line. The linear regression equation is also shown.

CCD Array Detection System

The CCD array detection system was used to examine Raman spectra in detail. As shown in Figure 15, scattered light was imaged onto the entrance slit of the Spex 1401 double spectrometer using a 50 mm camera lens. The entrance slit is typically set to 50 μm for optimum spectral resolution. The reciprocal linear dispersion has been

measured to be 0.493 nm/mm.[12]   Since each pixel in the CCD Array is 23 μm in dimension, the wavelength dispersion can be expressed as 0.13 Å per detector element or 0.398 cm^{-1} per detector element at 533.6 nm. A discussion on the linearity of wavelength dispersion in spectrometers is given in Appendix C. Based on extensive work by S. Ernst and P. Yaney,[13] the resolution was within that of one pixel, 0.13 Å or 0.398 cm^{-1} at 533.6 nm assuming the illumination was "source-limited." However, this result in no way restricts the precision of Raman line measurements since the irradiance of their Lorentzian profiles is smooth and their linewidths are an order of magnitude larger than the resolution. The CCD array by Princeton Instruments consists of 576 pixel columns and 384 pixel rows. The useable region of the CCD array for measurements was limited to 250 pixel columns and 210 pixel rows centrally located on the larger array. Horizontally, this useable region was defined by a maximum center slit width of 3 mm within the double spectrometer. Vertically, this region was defined by the length of the light on the entrance slit set by the line of laser light and the magnification. The vertical columns of pixels record spatial information about the scattered light. In other words, the vertical profile of the scattered light corresponds with the positions of the exciting light on the specimen perpendicular to the direction in which light is dispersed into a spectrum. This description is easy to see when the line of laser light from the cylindrical optics is considered. The length of this line, typically 35 μm using the 60x ELWD microscope objective, provided spatial information vertically on the array for positions on the specimen covered by the line's length. The width of the line was about 2 μm and light in this direction was dispersed by the spectrometer to provide spectral information horizontally at each "point"

corresponding to a pixel row covered by the line. In this way, a vertical array of spectra was obtained.

The CCD resolution at the specimen surface can be determined by considering the magnification factors in the intermediate optical system. Lenses L1 and L2 have 200 mm focal lengths and the camera lens has a 50 mm focal length. Blackshire[12] determined that the demagnification factor from the focus between lenses L1 and L2 to the CCD array is 4.85. Since the 60x ELWD microscope objective has a 3.49 mm focal length, the magnification from the specimen surface to this focus is 57.3. So the total magnification was 11.8, giving a 23 μm pixel at the CCD array an image size of 1.95 μm at the specimen surface. Thus, each vertical pixel on the CCD array corresponded to 2 μm on the specimen surface.

The polarization of light exiting the Nd:YAG laser was vertical such that the polarization was parallel to the length of the laser line illumination. The incident and collected light polarizations could be controlled with the use of linear polarizers. To maximize the incident light signal in polarization studies, a half-wave plate (HWP) was used to align the incident polarization angle to the transmission axis of the incident light polarizer. The response of a grating spectrometer is typically maximum when the polarization of the incident light is perpendicular to the grating grooves (i.e., the slit length), all other factors being equal. In backscattering from powders and microscopically rough polycrystalline surfaces, the scattered light is often completely depolarized. Thus, the Raman scattering from these types of specimens is usually independent of the polarization of the light incident on the specimen.

The use of the liquid-nitrogen-cooled CCD array provides many benefits over the PMT detection system. With the use of the double spectrometer, high resolution was achieved for detailed study of Raman spectra over a range of about 70 cm^{-1} at a Raman shift of 790 cm^{-1} using 532 nm light. The grating was not scanned as with the PMT detection system. Instead, the grating remained stationary during data collection since the array detector is multi-channel, both spatially and spectrally. In addition, the signal-to-noise ratio (SNR) was very good due to the -100° C temperature of the detector. Integrating the signal over longer exposure times increases the SNR since noise increases by the square root of its amplitude, whereas signal increases simply by its amplitude. The SNR was also increased by binning the signals of each pixel vertically into a "super" pixel whose width was one pixel but whose height depended on the binning factor. Typically, the light that fell within the central 40 rows of the array, namely rows 172 through 212, were binned using a binning factor of 40 (This corresponds to a maximum line length of 80 μm). Only one spectrum was obtained using this technique, yet this spectrum represented the composite spectrum due to the entire length of the laser line.

A narrow range spectrum of the specimen was obtained by first determining the setting of the spectrometer grating which corresponds to the center of the desired spectrum. This setting corresponded to the approximate center pixel (Pixel 200 horizontally). The spectrum could be calibrated by using a known reference such as an atomic line. Two reference lines are needed to determine the wavelength dispersion (Å per pixel element) in a given spectral region. Knowing the wavelength dispersion of this region prior to taking the experimental spectrum required just one reference line for

spectral position calibration. Once the wavelength scale was found, the spectrum was easily scaled to wavenumbers. Since the spectral range was about 70 cm^{-1}, the wavelength dispersion was assumed to be constant over this region, although it does decrease slightly with increasing wavelength. The spectrum of an atomic line was fitted with a triangle function to obtain a subpixel determination of the line's pixel position for accurate spectrum calibration. Once the spectrum was accurately calibrated in wavenumbers, the Raman lines in the spectrum were fitted to Lorentzian profiles using the curve fitting routines listed in Appendix B. These procedures were used to determine the Raman shift, linewidth, and line strength of each Raman line with fitting uncertainties. A linearly-sloped (tilted) background was also taken into consideration during the fitting routines.

The wavelength values of these atomic spectral lines were precise to less than 0.001 Å and were taken from the American Institute of Physics Handbook.[14] A least squares triangle fit of the atomic spectral line from the CCD data was used as an interpolation technique to precisely determine the center wavelength position of the atomic line. Due to the few data points (three or four pixels) defining the position of the atomic line, this method was considered the best since it assumes a simple symmetric profile. This triangle function is given by

$$\text{triangle}(p) = A \, \Lambda\!\left(\frac{p - p_0}{\Delta p}\right) + B \tag{22}$$

where B is the background in counts, A is the amplitude in counts, p is the pixel scale of the CCD array, p_0 is the center position of the atomic line in pixels, and Δp is the FWHM of the triangle function in pixels. The unit triangle function $\Lambda(x)$ is defined as

$$\Lambda(x) = \begin{cases} 1 - |x| & |x| \leq 1 \\ 0 & \text{otherwise} \end{cases} \tag{23}$$

Typically, only the maximum three or four pixels were used in the triangle fit due to aberrations at the "wings" of the triangle near the base, so that a fit of the nearby background is unnecessary. However, if only three pixels were used for the triangle fit, no fitting errors in the three parameters could be obtained since three pixels absolutely define a symmetric triangle. A scheme was devised to determine the uncertainty of the atomic line center position (the spectral peak offset uncertainty) as shown in Figure 17.
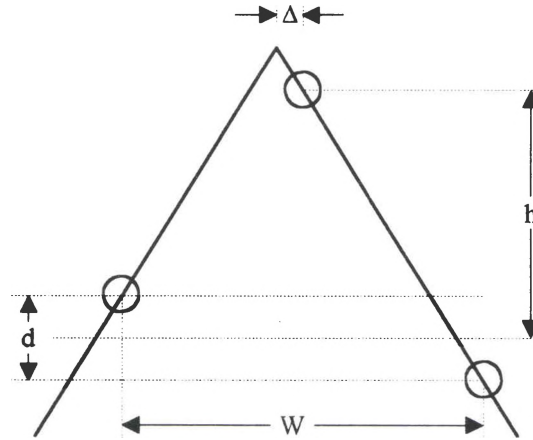
Figure 17. Determination of the spectral peak offset Δ and its uncertainty for an atomic spectral line using the absolute count difference d between the two outer pixels, the absolute count difference h between the central pixel count and the median count of the two outer pixels, and the pixel spacing W between the two outer pixels.

The offset Δ was determined through the use of similar triangles and is defined by

$$\Delta = \frac{d/2}{d/2+h}\left(\frac{W}{2} \pm \frac{\delta W}{2}\right) \tag{24}$$

where d is the absolute count difference between the outer two pixels, W is the pixel spacing between the outer two pixels, and h is the absolute count difference between the central pixel count and the median count of the two outer pixels. For three pixels, the pixel spacing W of the triangle illumination could be as large as three pixels or as small as

one pixel and still cause three pixel positions to "light up." This statement means that the pixel spacing W is 2 ± 1 pixels wide. The offset Δ with its uncertainty is then

$$\Delta = \frac{d/2}{2\,(d/2 + h)}(2 \pm 1) \text{ pixels} \qquad (25)$$

The behavior of the spectral peak offset as a function of the $\frac{d}{2h}$ ratio is shown in Figure 18.
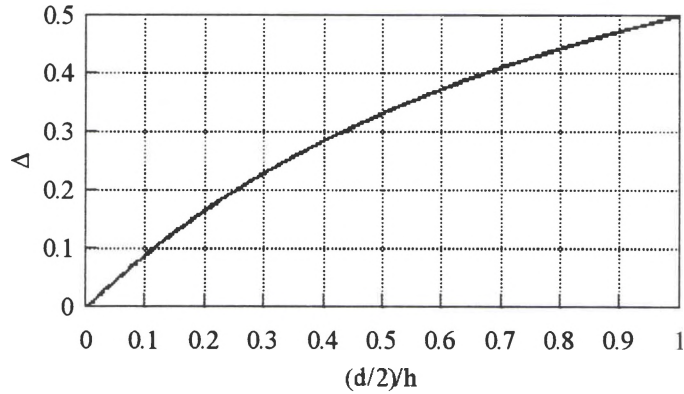
Figure 18. Behavior of the spectral peak offset Δ of an atomic line from the center pixel as a function of the pixel locations relative to the triangle fit.

The wavelength of the incident laser line was determined by using the known wavelengths of atomic spectral lines for calibration within the 70 cm^{-1} range of the CCD array detector. Ideally, two atomic spectral lines, one on either side of the laser line, were used with a fairly large spacing for higher precision. After performing triangle fits of the atomic lines and the laser line for subpixel determination of their positions on the CCD array, linear interpolation was performed to determine the laser wavelength. Usually, the spectrometer was stepped, incrementing the position of each run by 1 cm^{-1} or 2 cm^{-1}, for 20 runs to obtain a statistical average of the laser wavelength.

Atomic spectral lines were then chosen within the 70 cm^{-1} region of interest for determining the wavelength dispersion (in units of nm per pixel element). For the majority

of the studies of 6H SiC ceramic, this region was at the 790 cm^{-1} Raman shift from the 532 nm laser line where the Raman modes of the planar optic branch occur. The spectral lines were typically chosen close together for a higher precision determination of the wavelength dispersion, since this parameter decreases slowly with increasing wavelength (see Appendix C). After performing triangle fits of the atomic lines in this region, the pixel spacing and the known wavelength spacing were used to determine the wavelength dispersion at the median of the two atomic line wavelengths. The spectrometer was usually stepped, again incrementing the position of each run by 1 cm^{-1} or 2 cm^{-1}, for 20 runs to obtain a statistical average of the wavelength dispersion for this region.

From the discussion on wavelength dispersion linearity of spectrometers in Appendix C, the pixel scale of a typical run may be rescaled to wavelength using the known wavelength dispersion and a known reference spectral line according to

$$\lambda_i = \lambda_r + D_\lambda \cdot (p_i - p_r) \tag{26}$$

where λ_i is the wavelength in nm at pixel p_i, λ_r is the reference line wavelength in nm, p_r is the position of the reference line in pixels, and D_λ is the wavelength dispersion in nm/pixel. Knowing the incident laser wavelength, the Raman shift in cm^{-1} can be found according to

$$\Delta\bar{v}_i = (10^7 \text{ cm}^{-1} \cdot \text{nm}) \left(\frac{1}{\lambda_{las}} - \frac{1}{\lambda_i} \right) \tag{27}$$

where $\Delta\bar{v}_i$ is the wavenumber position at pixel p_i, λ_{las} is the laser wavelength in nm, and λ_i is the wavelength at pixel p_i in nm. A schematic drawing of the laser line, a Raman line (such as the 788 cm^{-1} TO line), and a reference line such as neon is shown in Figure 19. A summary of the results for several laser wavelengths and the wavelength dispersion of some regions of interest are given in Table 3.
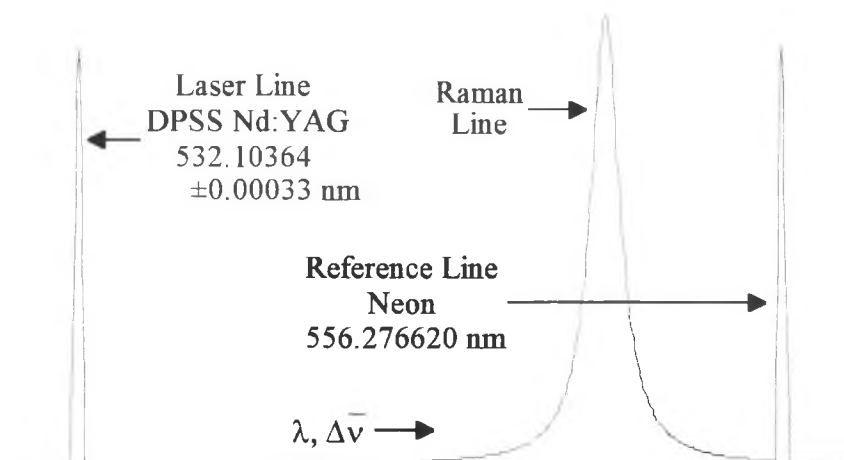
Figure 19. Schematic illustration in the Stokes regime of the laser line (532 nm Nd:YAG), Raman line, and atomic reference line (neon) indicated by the arrows. The arrow from the wavelength (wavenumber shift) label indicates the direction of increasing wavelength (wavenumber shift).

Table 3. Determination of laser wavelengths and wavelength dispersion of some spectral regions of interest.

Nd:YAG	D_λ at 52.5 cm^{-1}	Reference Lines	D_λ at 806.1 cm^{-1}	Reference Lines	Calibration Line
532.10364± 0.00033 nm	0.01134179± 0.00000088 nm/pixel	Ne 533.07775 nm 534.10938 nm	0.0113039± 0.0000045 nm/pixel	Xe 555.2385 nm 556.6615 nm	Ne 556.27662 nm
Ar ion	D_λ at 36.3 cm^{-1}	Reference Lines	D_λ at 796.9 cm^{-1}	Reference Lines	Calibration Line
487.98502± 0.00026 nm	0.0114543± 0.0000029 nm/pixel	Ne 488.49170 nm 489.21007 nm	0.0113612± 0.0000019 nm/pixel	Ne 507.42007 nm 508.03852 nm	Ne 508.03852 nm

CHAPTER IV

RAMAN STUDIES OF SILICON CARBIDE SINGLE CRYSTAL AND MACHINED POLYCRYSTALLINE SPECIMENS

Typical Stokes Raman Spectra of 6H SiC Specimens

A survey spectrum of both single crystal and polycrystalline ceramic was performed to determine the Raman active modes from 100 cm^{-1} to 1000 cm^{-1} using the 532 nm Nd:YAG laser. These spectra are shown in Figure 20.
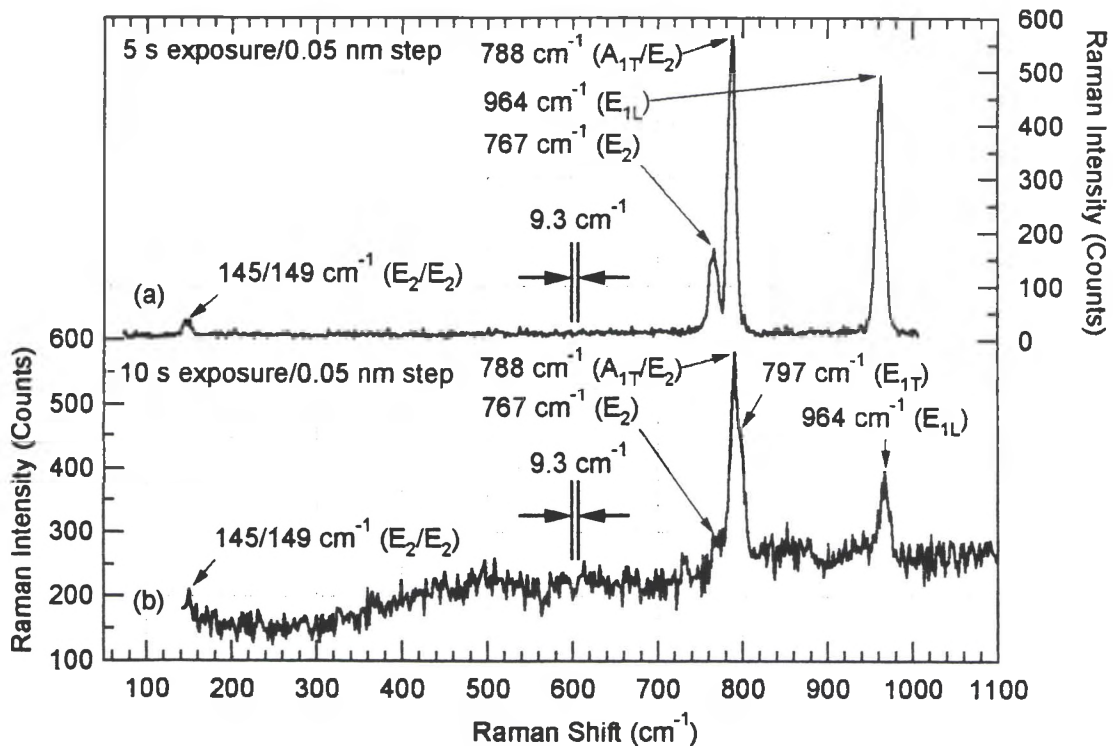
Figure 20. Survey spectra of 6H SiC (a) single crystal and (b) polycrystalline ceramic.

The visible modes are labeled along with their Raman shift. Both scans were from 100 cm^{-1} to 1000 cm^{-1} in increments of 0.05 nm (1.7 cm^{-1}). The entrance and exit slits of the Triplemate spectrometer were set to 200 μm with the limiting aperture in the pre-filter set to 8 mm and the entrance slit to the pre-filter having dimensions of 0.8 mm x 2 mm. The 200 μm entrance/exit slits give a resolution of 0.28 nm (9.3 cm^{-1}). The grating ruling is 1200 lines/mm. The 60x ELWD microscope objective was used for illuminating each specimen surface with a line of 532 nm light. The c-axis of the single crystal specimen was about 3° off the backscattering axis of the Raman microprobe, hence the phonon propagation direction was nearly parallel to the crystalline axis. Since no polarizers were used for selecting the polarization of the scattered light, scattered light polarized both parallel and perpendicular to the incident polarization could be detected. The exposure time per step was five seconds for the single crystal specimen and ten seconds for the polycrystalline ceramic specimen. Distinct Raman lines at 145/149 cm^{-1}, 767 cm^{-1}, 788 cm^{-1} and 964 cm^{-1} were observed for the single crystal specimen, corresponding to the E_2/E_2, A_{1T}/E_2, E_2, and A_{1L} modes, respectively. These identifications are based on the work of Feldman et al.[9] The E_2 modes at 145 cm^{-1} and 149 cm^{-1} are planar acoustic modes, the E_2 modes at 767 cm^{-1} and 788 cm^{-1} are planar optic modes, and the A_{1L} mode at 964 cm^{-1} is a longitudinal optic (LO) mode. In the case of perfect alignment along the c-axis, mode selection rules indicate that A_1 modes should appear for parallel configurations, yet because of the mixed mode frequency results of Equation (17), the A_{1T} mode, a transverse optic (TO) mode, should not appear in the perfect case. The A_{1T} mode does appear in the data due to the 3° tilt in the c-axis. Therefore, the A_{1T}/E_2 designation

was used to indicate that both modes were actually present at 788 cm^{-1}. The other spectrum is a survey of a polycrystalline 6H SiC specimen that was processed with creep feed grinding at 88.9 mm per minute. The 767 cm^{-1}, 788 cm^{-1}, and 964 cm^{-1} Raman lines were again observed. As in the single crystal case, the 788 cm^{-1} line is a superposition of the A_{1T} and E_2 modes; however, the 797 cm^{-1} Raman line, an E_{1T} mode, is also present. These other modes appeared because, for a polycrystalline material, the resultant Raman spectrum represents the "composite" of the spectra from each unique crystallite geometry in the structure. The 767 cm^{-1}, 788 cm^{-1}, and the 797 cm^{-1} Raman lines (consisting of four modes: the E_2, A_{1T}/E_2, and E_{1T} modes, respectively) were the primary objects of study for this thesis. The use of the CCD array detection system allowed high precision measurements of these Raman lines, on the order of 0.02 cm^{-1}, to relate changes in linewidth or Raman shift to macroscopic characteristics of the material, particularly the relative levels of residual surface stress produced by grinding processes. The spectra of these specimens were examined in the 790 cm^{-1} region using the CCD detection system as shown in Figure 21. The middle slit of the double spectrometer was set to 3 mm, the entrance slit was set to 50 μm, and the exposure time was three minutes for both the single crystal and the polycrystalline 6H SiC specimens mentioned above. The single crystal specimen gave strong E_2 modes at 767 cm^{-1} and 788 cm^{-1} only since the incident and scattered light polarization are crossed and phonon propagation is parallel to the c-axis of the crystal.
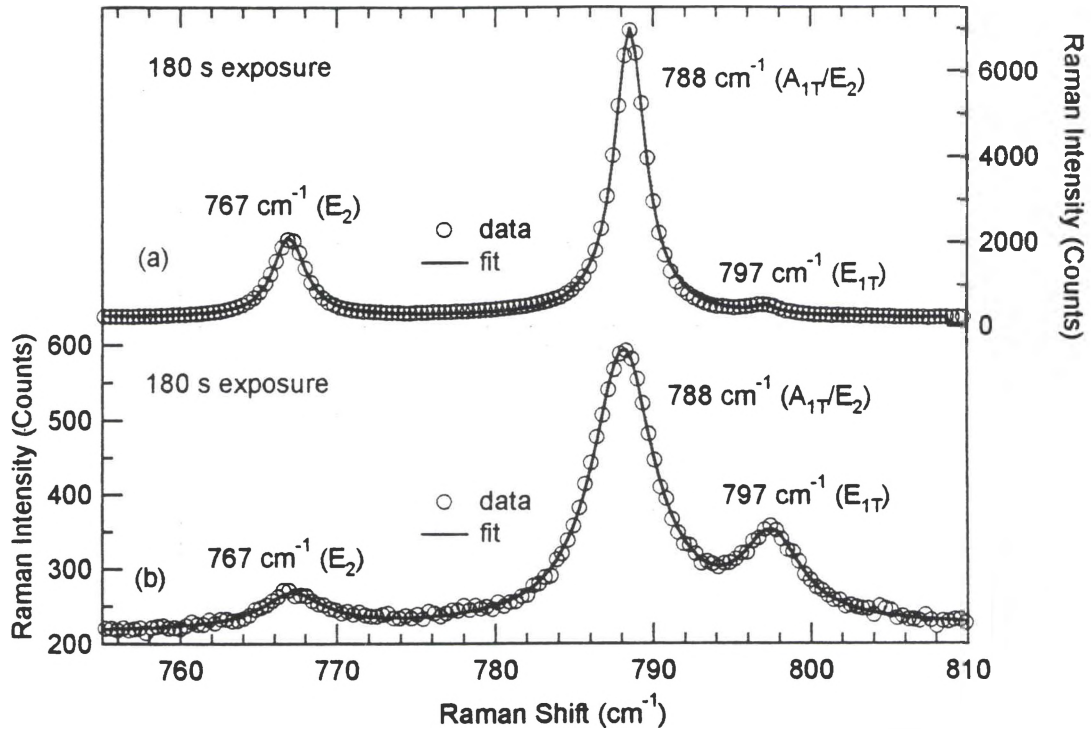
Figure 21. Typical Raman spectrum in the 790 cm^{-1} region of 6H SiC (a) single crystal and (b) polycrystalline ceramic.

There is a hint of the mode at 797 cm^{-1} due to the large angle of scattered light collected by the microscope objective. The polycrystalline specimen, however, has namely three distinguishable modes since the c-axis of each crystallite can be arbitrarily oriented with respect to the phonon propagation direction. These modes are the E_2 (767 cm^{-1}), A_{1T}/E_2 (788 cm^{-1}), and E_{1T} (797 cm^{-1}) modes. The polarization dependence of these modes will be discussed more thoroughly in the next section dealing with 4H and 6H SiC single crystal specimens.

Studies of 4H and 6H SiC Single Crystal Specimens

The polarization dependence of the modes on the planar optic branch of two small single crystal wafers was examined for comparison with those of polycrystalline

specimens. In order to properly identify the modes for a particular configuration, the Raman tensor of each vibrational mode of the C_{6v}^4 structure must be operated on by the incident and scattered field polarizations to determine whether a particular mode is active. Raman tensor analysis is discussed in Appendix D. Table 4 lists the possible configurations used in this study and their resultant phonon symmetries.

Table 4. Polarization and propagation symbols used for determining phonon symmetry in the 4H and 6H SiC single crystal study. Note that a prime symbol used with a propagation direction is used to denote propagation in the opposite direction.

Polarization symbol	Phonon symmetry	Propagation symbol	Phonon propagation angle θ
- (x x) -	A_1 , E_2	z (- -) z'	0°
- (y y) -	A_1 , E_2		
- (x y) - or - (y x) -	E_2		
- (y y) -	A_1 , E_2	x (- -) x'	90°
- (z z) -	A_1		
- (y z) - or - (z y) -	E_1		
- (x x) -	A_1 , E_2	y (- -) y'	90°
- (z z) -	A_1		
- (x z) - or - (z x) -	E_1		

Note that the four-letter symbol of Damen et al.[15] is used to represent the propagation directions and polarizations of the incident and scattered light relative to the crystal c-axis. The outer two letters are the incident and scattered photon propagation directions, respectively, and the inner two letters are the incident and scattered photon polarization directions, respectively. A prime symbol used with a propagation direction is used to denote propagation in the opposite direction. Note that backscattering along the x or the y directions yields the same results since the crystal is uniaxial.

A series of spectra were obtained from the nitrogen-doped 6H SiC single crystal specimen to obtain a basis for comparison with the Raman spectra of the polycrystalline specimens used in the grinding studies described in the next section. The cylindrical optics of the Raman microprobe system were employed to illuminate the specimen surface with an elliptical laser line 35 μm in length and 2 μm in width. A weighted statistical averaging of the Raman shifts, linewidths, and relative strengths of the Raman lines in each spectrum gave a statistical measure of each quantity for comparison with other specimens (see Appendix E). The spectra were obtained in the $z(xy)z'$ configuration, producing the E_2 modes at 767 cm^{-1} and 788 cm^{-1}. The E_{1T} mode also appeared weakly at 797 cm^{-1} due to the large 0.7 NA of the microscope objective. Another n-type 6H SiC single crystal specimen by CREE was examined and similar results were obtained.

The spectra of the single crystal specimens for the polarization study were obtained with the same settings with the exception of the incident and scattered light polarizations and the orientation of the c-axis. The exposure time was three minutes and the entrance slit width was 50 μm. The 60x ELWD microscope objective focused 532 nm light onto the specimen surface. Since the normal to the wafer plane defined the c-axis, the backscattering geometry of the Raman microprobe allowed phonon propagation parallel or perpendicular to the c-axis. Phonon propagation perpendicular to the c-axis was achieved by focusing the elliptical laser line onto the edge of the wafer so that the wafer normal was perpendicular to the propagation direction. For phonon propagation parallel to the wafer c-axis, the wafer surface was illuminated with a laser "spot" rather than an elliptical laser line in order to obtain a well-defined polarization of the incident

light. The first specimen studied was an ATMI 6H SiC single crystal specimen with a nitrogen dopant level of 3×10^{16} cm^{-3}. Figures 22(a) and 22(b) demonstrate spectra of the 790 cm^{-1} region in parallel and crossed (incident/scattered) polarizations, respectively, for phonon propagation parallel to the c-axis. Note that both the A_1 and E_2 modes are allowed for uncrossed polarizations, but only the E_2 modes are allowed for crossed polarizations. Other modes may appear, however, due to the large 0.7 NA of the microscope objective, which allows other excitation field components to produce "unallowed" phonon modes. The change in strength of each mode with polarization/orientation, however, can usually indicate if its existence is "allowable" in the strictest sense. For example, a relatively weak mode would tend to indicate that its appearance is due to the large NA of the collection optics, but this is not always true. Feldman et al.[9] has observed an angular dependence of the frequency of the strong modes on the phonon propagation direction due to crystal anisotropy. The theory behind this observation was discussed briefly in Chapter II in which these modes contain mixtures of components parallel (axial) and perpendicular (planar) to the c-axis for both the transverse and longitudinal frequencies. The transverse and longitudinal mode frequency variations of 6H SiC, from Equations 17 and 18, are described, respectively, by

$$\bar{v}_T^2(\theta) = (788)^2 \sin^2\theta + (797)^2 \cos^2\theta \tag{28}$$

$$\bar{v}_L^2(\theta) = (964)^2 \cos^2\theta + (970)^2 \sin^2\theta \tag{29}$$

where θ is the phonon propagation angle with respect to the crystal c-axis. Thus, the A_{1T} (788 cm^{-1}) line of Figure 22(a) is not allowed since the phonon propagation angle is parallel to the c-axis.
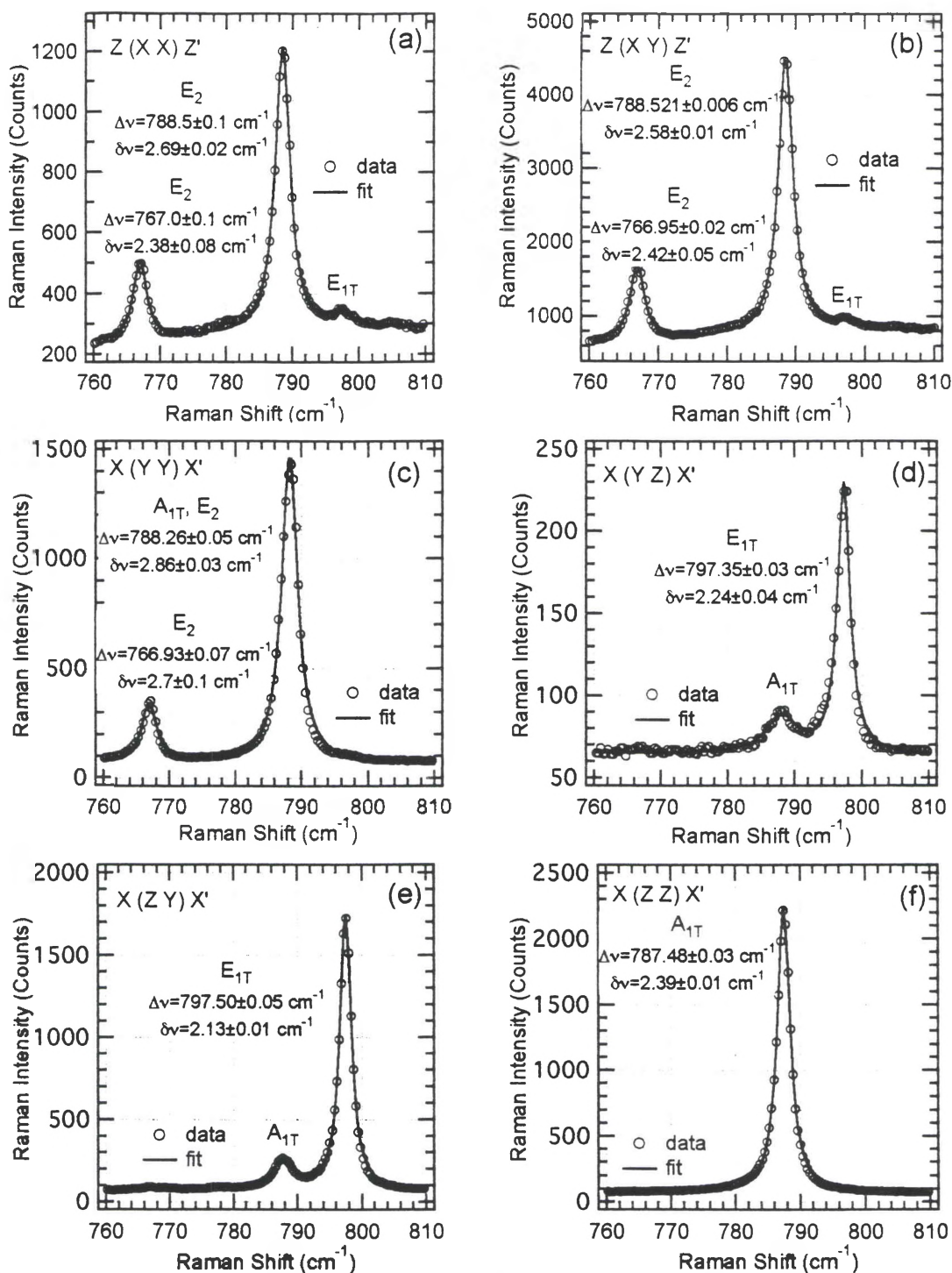
Figure 22. The Raman spectra of the 790 cm^{-1} region of 6H SiC single crystal using a backscattering geometry in six different polarization configurations for incident/scattered light: (a) parallel and (b) crossed with propagation along c-axis; (c) parallel to each other and orthogonal to c-axis, (d) crossed (perpendicular/parallel), (e) crossed (parallel/perpendicular), and (f) parallel to each other and parallel to c-axis with propagation orthogonal to c-axis.

The bumps in Figures 22(a) and 22(b) at 797 cm^{-1} represent E_{1T} modes "leaked" through the microscope objective's large NA. Figures 22(c)-(f) represent the four parallel/perpendicular polarization configurations for phonon propagation orthogonal to the c-axis. Figure 22(c) demonstrates the superposition of the A_{1T} and E_2 modes at 788 cm^{-1} in addition to the E_2 mode at 767 cm^{-1}, both incident and scattered polarizations being orthogonal to the c-axis. When both polarizations are parallel to the c-axis as shown in Figure 22(f), only the A_{1T} mode is allowed at 788 cm^{-1}. Finally, in Figures 22(d) and 22(e), the crossed polarization configuration allows only the E_{1T} mode at 797 cm^{-1}. However, the very strong A_{1T} mode "leaks" through the imperfect polarizations. Notice the dramatic decrease in Raman signal strength in Figure 22(d) relative to Figure 22(e) due to the fact that the spectrometer is least responsive to light polarized parallel to the grating grooves.

A similar study was conducted using an ATMI 4H SiC single crystal specimen (n-type). This polytype has the same point group symmetry as 6H SiC.[8] Figures 23(a) and 23(b) represent parallel and crossed polarization configurations of the Raman spectrum with the phonon propagation direction parallel to the c-axis. Again, the E_2 mode at 777 cm^{-1} is allowed but the A_{1t} mode at 783 cm^{-1} isn't present in Figure 23(a) due to the 0° phonon propagation angle. Bumps at 797 cm^{-1} hint at the E_{1T} mode being suppressed in this configuration. The Raman spectra of Figures 23(c)-(f) were taken in the four parallel/perpendicular polarization configurations with a phonon propagation angle of 90°.
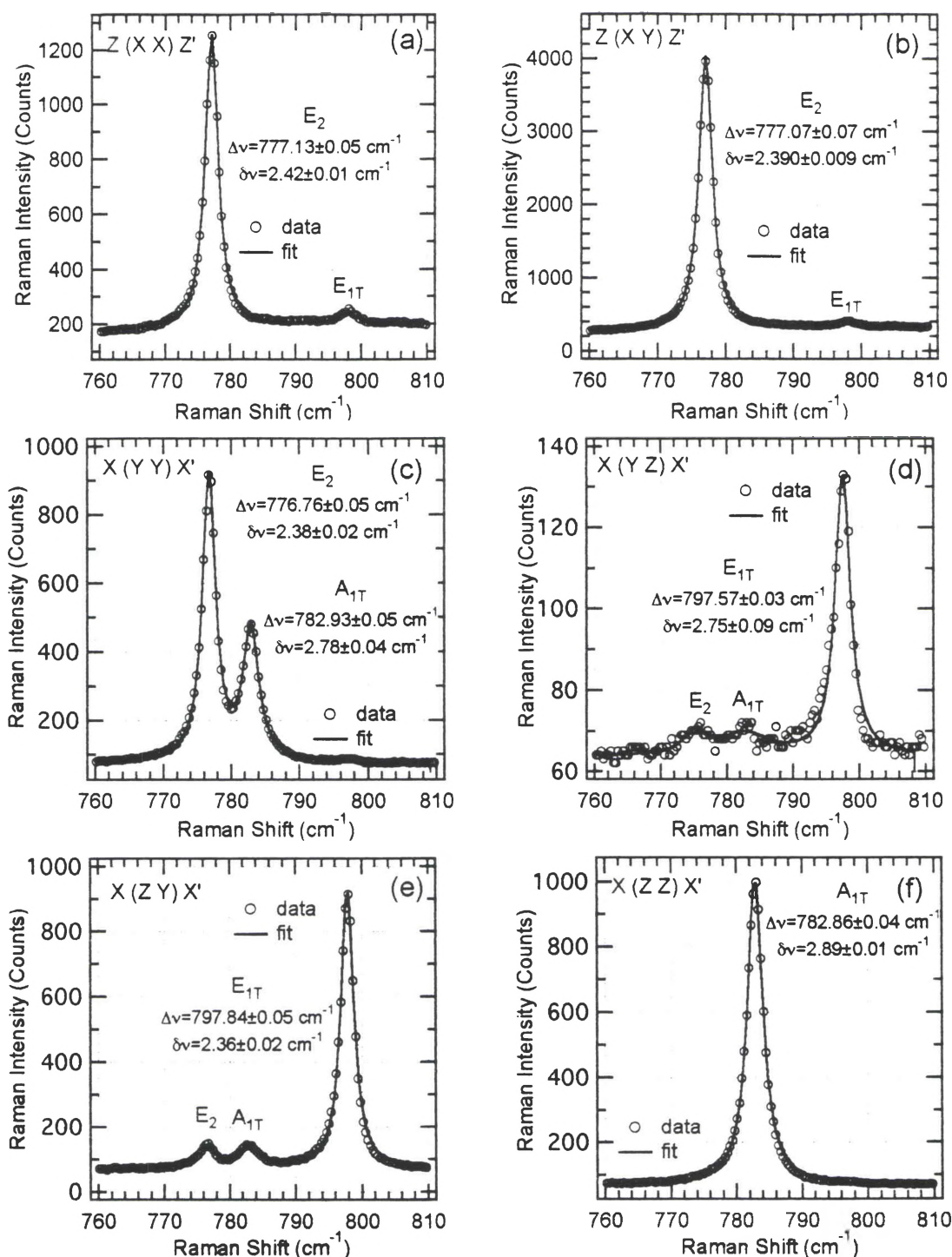
Figure 23. The Raman spectra of the 790 cm^{-1} region of 4H SiC single crystal using a backscattering geometry in six different polarization configurations for incident/scattered light: (a) parallel and (b) crossed with propagation along c-axis; (c) parallel to each other and orthogonal to c-axis, (d) crossed (perpendicular/parallel), (e) crossed (parallel/perpendicular), and (f) parallel to each other and parallel to c-axis with propagation orthogonal to c-axis.

Figure 23(c) allows both the E_2 and A_{1T} modes at 777 cm^{-1} and 783 cm^{-1}, respectively, for both polarizations orthogonal to the c-axis. Figure 23(f) allows only the A_{1T} mode at 783 cm^{-1} for both polarizations parallel to the c-axis. Finally, Figures 23(d) and 23(e) allow only the E_{1T} mode at 797 cm^{-1}, with the E_2 and A_{1T} modes suppressed at 777 cm^{-1} and 783 cm^{-1}, respectively, for crossed polarization configurations. Again, notice the reduction in signal strength of Figure 23(d) relative to Figure 23(e) due to the spectrometer's reduced response to light polarized parallel to the grating grooves. From the studies of the 6H SiC single crystal, it is easily seen that, for a polycrystalline ceramic, the resultant Raman spectrum is a superposition of all possible orientations and polarizations. By considering Figures 22(a)-(f), "composite" Raman lines occur at 767 cm^{-1} (E_2), 788 cm^{-1} (A_{1T}/E_2), and 797 cm^{-1} (E_{1T}). The frequencies (in cm^{-1}) of the strong modes observed by Feldman et al.[9] are given in Table 5 while their weak modes are given in Table 6.

Table 5. Frequency dependence (in cm^{-1}) of the strong phonon modes in 6H SiC on the phonon propagation angle θ. One mode is longitudinal (L) and two modes are transverse (T_1 and T_2). E_{1T} is doubly degenerate at $\theta=0°$.[a]

	$\theta=90°$	$\theta=45°$	$\theta=0°$
L	E_{1L} 970	$(A_1+E_1)_L$ 967	E_{1L} 964
T_1	E_{1T} 797	E_{1T} 797	E_{1T} 797
T_2	A_{1T} 788	$(A_1+E_1)_T$ 792	E_{1T} 797

[a] Reference 9.

The results of these single crystal studies will later be used to show that the 4H SiC polytype exists in some instances along the surfaces of the polycrystalline hexagonal SiC specimens studied.

Table 6. Frequencies (in cm^{-1}) of weak phonon modes in 6H SiC, assigned to $x=q/q_{max}$ in the large zone. B_1 modes are forbidden (F.) and two components of optic doublets were not observed (N.O.).[a]

Branch	x=0.33	x=0.67	x=1.00
Axial Optic	B_1 F. B_1 F.	A_1 889 A_1 N.O.	B_1 F.
Planar Optic	E_2 788 E_2 N.O.	E_1 777 E_1 769	E_2 766
Axial Acoustic	B_1 F. B_1 F.	A_1 508 A_1 504	B_1 F.
Planar Acoustic	E_2 149 E_2 145	E_1 241 E_1 236	E_2 262

[a] Reference 9.

Grinding Studies of 6H SiC

The presence of residual surface stresses on 6H SiC specimens subjected to different grinding processes was studied based on measurements of changes in Raman shift and linewidth of the 767 cm^{-1}, 788 cm^{-1}, and 797 cm^{-1} Raman lines. These studies focused particularly on the measurements of the 788 cm^{-1} Raman line due to its large line strength and its stability. The 767 cm^{-1} Raman line is a weak mode and therefore measurements of this line would not reflect systematic errors associated with its weaker intensity and the background profile. The 797 cm^{-1} Raman line can represent one or two modes, both E_{1T} TO modes (see Table 5). The first TO mode is stationary, whereas the second TO mode varies with the phonon propagation angle. This "doubling" of two strong modes could also produce systematic errors in the measurements of this line. Therefore, the 788 cm^{-1} Raman line was selected for optimum measurement of changes in position and linewidth. As mentioned in Chapter II, these changes can be related to the deformation of the lattice

structure due to the compressive forces involved during ceramic material processing. Anastassakis[3] evaluates the effect uniaxial stresses have in shifting and splitting vibrational modes as a result of lattice deformation. Assuming the deformation is elastic, the stress σ and strain ε are proportional and related by Young's modulus E ($\sigma=E\varepsilon$). A change in the Raman shift can be related to a corresponding change in the stress or strain according to

$$\frac{\delta\Delta\nu}{\nu_0} = \kappa\,\frac{\delta V}{V} \cong 3\,\kappa\varepsilon = 3\,\kappa\frac{\sigma}{E} \qquad (30)$$

where $\delta\Delta\nu$ is the change in Raman shift, ν_0 is the frequency, δV is the change in volume, V is the volume, and κ is the phonon deformation potential. By making these assumptions, the relative residual surface stresses may be estimated simply from precise measurements of these changes in Raman shift and linewidth.

These grinding studies were conducted on specimens processed according to nine different methods. An "as-sintered" specimen was used as a reference for the measurement of relative residual stresses incurred from processing. The remaining specimens began the processing procedure with baseline (conventional) grinding as specified by ASTM C 1161-90 standards.[16] Grinding processes (in no particular order) include: baseline grinding along the parallel and at a 15° bias, creep feed grinding, ultrasonic grinding, polishing, heat treatment, and oxidation. The relative residual surface stress was measured for specimens which underwent each of these finish processing methods to ascertain the residual surface stress generated. The effect of machining treatment on flexural strength was also measured. A description of each process is described in the following section.

Processing Methods

The baseline (conventional) and creep feed grinding processes are illustrated in Figure 24.

(a) baseline grinding: large feed rate and small infeed
(b) creep feed grinding: small feed rate and large infeed
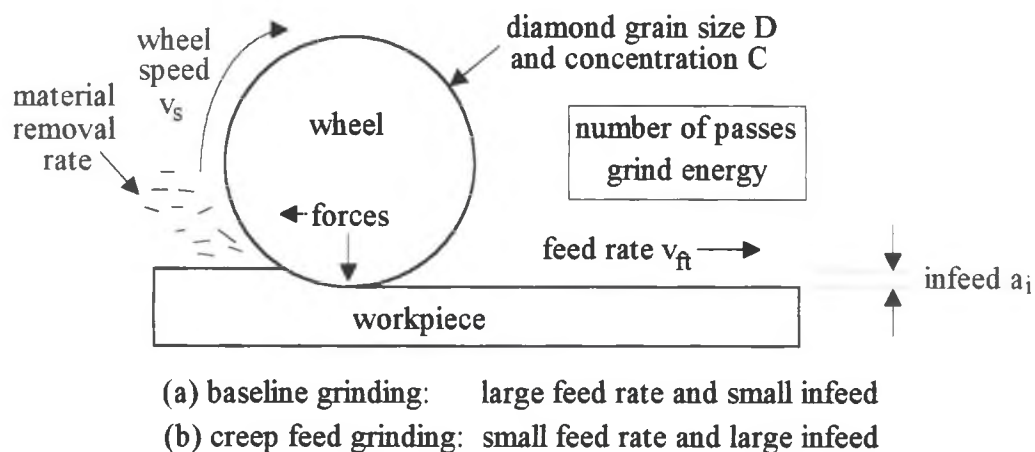
Figure 24.   The (a) baseline (conventional) and (b) creep feed grinding processes. Other grinding parameters are depicted in addition to the feed rate and infeed.

Each process involves the use of a grinding wheel on a workpiece until the desired grind depth is achieved. Typically, the cutting surface of the grinding wheel consists of diamond grains of characteristic grit size which are resin, metal, or vitrified bonded to the grind surface of the wheel.[17] (Grit size is a measure of abrasive grain diameter and refers to the maximum number of mesh holes per inch in which a wire mesh will pass certain size granular particles.) The grind infeed a_i refers to the depth of the grind wheel per pass along the workpiece. The feed rate v_{ft} refers to the speed at which the workpiece is fed through the grinding wheel. Finally, the cutting speed v_s refers to the wheel speed at the contact between the grinding wheel and the workpiece. The main distinction between conventional grinding and creep feed grinding lies in the choice of infeed and feed rate

values. Conventional grinding is characterized by small infeeds and high feed rates, whereas creep feed grinding involves low feed rates with larger infeeds. Of course, conventional grinding requires more passes than creep feed grinding to remove the same amount of material. The specific material removal rate is defined as the product of the infeed and feed rate, giving the workpiece volume removed per wheel width per unit time,[2] as evident from Figure 24. The material removal rates of both methods may be matched for optimum efficiency by defining the creep feed grinding infeed or feed rate. One noticeable difference between the two methods is the contact length l_c between the wheel and the workpiece. This contact length is given by

$$l_c = r\cos^{-1}\left(1 - \frac{a_i}{r}\right) \approx \sqrt{2a_i r} \text{ for } a_i << r \qquad (31)$$

where r is the radius of the grinding wheel and a_i is the infeed. The larger contact length (or area) due to the increased infeed results in more diamond grain cutting edges with smaller chip thicknesses being produced. Creep feed grinding requires higher rigidity due to the high normal forces, yet because of the increased number of cutting edges, the normal force per cutting edge is lower than that of conventional grinding.[2] The grinding wheel direction typically travels opposite to the workpiece feed direction at the point of contact (up cut or tensile grinding as opposed to down cut or compressive grinding) to avoid compressive grinding and any further material deformation, although chip sizes are usually larger under tensile grinding.[18] The material removal efficiency is described by the grinding ratio. This ratio is the workpiece volume removed per volume of diamond layer. Since the removal efficiency per cutting edge is smaller for a larger infeed, the wear on each cutting edge is lower, leading to a higher grinding ratio (or overall higher removal

efficiency). In addition, the smaller chip thicknesses due to creep feed grinding result in increased material strength.[2] A smaller depth of cut h_c is produced by a smaller feed rate v_{ft} and a higher cutting speed v_s. On the other hand, an increase in the infeed results in a larger h_c, producing larger chip thicknesses. However, assuming that h_c is directly proportional to the material removal rate and the contact length l_c, then from Equation (31), h_c is more dependent on the feed rate v_{ft} than on the infeed a_p, giving smaller chip thicknesses for creep feed grinding than for conventional grinding at the same material removal rate.[2] The grain size and concentration of diamond on the grind wheel are also important considerations. A smaller diamond grain size D and a higher diamond concentration C leads to a lower depth of cut h_c when all other grind parameters are kept fixed. The effect different process parameters have on the depth of cut for a single cutting edge is illustrated in Figure 25.
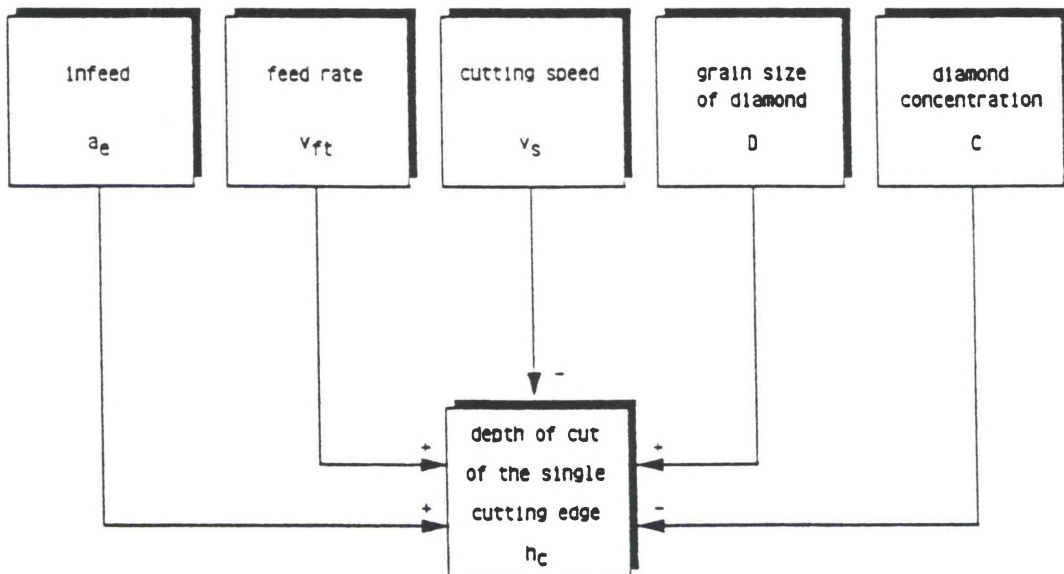
Figure 25. Effect different grinding process parameters have on the depth of cut for a single cutting edge. The sign indicates the effect when all other parameters remain constant [Reference 2].

The signs in Figure 25 indicate whether a particular parameter has a positive or negative effect on the depth of cut when all other parameters are held constant. Since the depth of cut is directly related to chip thickness, a lower depth of cut leads to higher surface, quality, smaller cracks in the material surface, and higher material strength.[2]

The ultrasonic grinding procedure is illustrated in Figure 26.
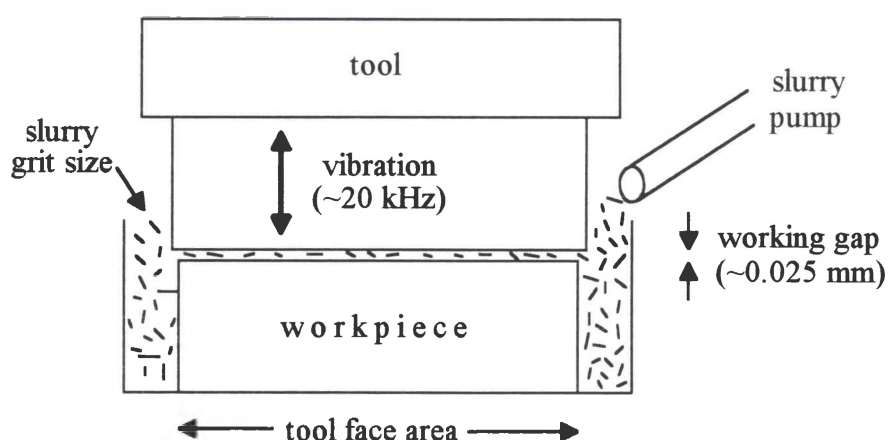
Figure 26. The ultrasonic grinding process (stationary).

A cutting tool in the shape of the cut to be made in the workpiece is ultrasonically vibrated up and down as a slurry of abrasive particles (usually boron carbide, silicon carbide, or alumina) is pumped between the tool and the workpiece. The tool is typically made of soft material like brass or bronze and operates at kHz frequencies very close to the surface of the workpiece. Hard tools are not used because they can fracture the abrasive particles. These particles actually perform the work of eroding the material since no pressure is applied directly from the tool to the workpiece. The average grinding pressure involved is typically less than 0.1 MPa.[17]

Highly polished grinding is achieved by repeating the baseline procedure using repeatedly smaller diamond grit sizes. The surface damage that was produced from a previous grinding process can be corrected by removing the damaged material, exposing more of the undamaged interior using finer grit size diamonds with a smaller depth of cut. However, the use of a finer grit size also introduces a certain amount of surface damage to the workpiece. A still finer grit size may then be used to remove the damaged material caused by the coarser grit procedure. In this pattern, surfaces may be more finely polished due to a decreasing depth of cut and a decreasing chip thickness, removing most of the damaged material introduced by the coarse grinding stages and thereby reducing the residual surface stress in the material.

Heat treatment is performed after the grinding of a ceramic specimen to enhance material strength. Oxidation involves heating a specimen to a specified high temperature in an air atmosphere over an extended period of time, usually on the order of weeks. Heat treatment is done over a short time frame such as a day. Oxidation, as the name implies, causes the buildup of an oxide layer over time. Heat treatment promotes the formation of a thin oxide layer to relieve the residual surface stress and heal flaws caused by machining. The oxidation of a specimen in service can initially have the same effect as a heat treatment. However, over time the oxide layer grows and defects can be generated in the surface.

The types of 6H SiC specimens studied can be divided into five groups: as-sintered (no processing), baseline (conventional), ultrasonic, highly polished, and creep feed. A brief description of each type of processing is described below. The baseline

group consists of four types of processed specimens: baseline grind parallel to the specimen bar's long dimension; baseline grind performed at a 15° bias from the bar's long dimension; parallel baseline grind followed by heat treatment for 24 hours at 1250 °C, and parallel baseline grind followed by oxidation for 500 hours at 1250 °C. The creep feed group consists of specimens machined at a feed rate of either 25.4 mm per minute or 88.9 mm per minute.

The baseline grind procedure consisted of a rough grind of course grit size (180 mesh) followed by a baseline finish of fine grit size (320 mesh). This procedure was performed on 6H SiC bars with the final dimensions of 45 mm x 4 mm x 3 mm. The grinding was done on both of the 45 mm x 4 mm planes. An overstock allowance of material was made for both surfaces such that the processed bar conforms to dimensional and processing standards outlined in ASTM C 1161-90.[16] A high feed rate and standard cutting speed were maintained for both grinding steps, although the stock removal was higher for the rough grind than for the finish grind according to ASTM standards. The stock removal is the product of the infeed and the number of passes made by the bar through the grind zone. These grinding passes were bi-directional with transverse positional indexing of the ceramic bar after every return pass. In other words, no grinding (or material removal) occurs during the return pass. The machining was performed in an up cut (or tensile) grinding configuration.

The creep feed grind procedure had a rough grind identical to that of the baseline grind procedure, yet differed in the finish grind. During the finishing step, the feed rate

was much slower and the infeed was much larger than those used in the finishing step of the baseline grinding procedure. All other machining parameters remained the same.

The ultrasonic grind procedure began with the same steps used in the baseline grind with the exception of the finishing step material removal. To conform with ASTM standards for dimensions of the modulus of rupture (MOR) bars, less material was removed during the baseline finishing step to allow overstock for the ultrasonic finish grind. The ultrasonic finish grind used the same grit size abrasive (320 mesh) in the slurry as that used in the baseline finish grind wheel. The ultrasonic finish grind was performed on a single side only.

The damage caused by grinding processes due to a single abrasive particle is illustrated in Figure 27.[19]
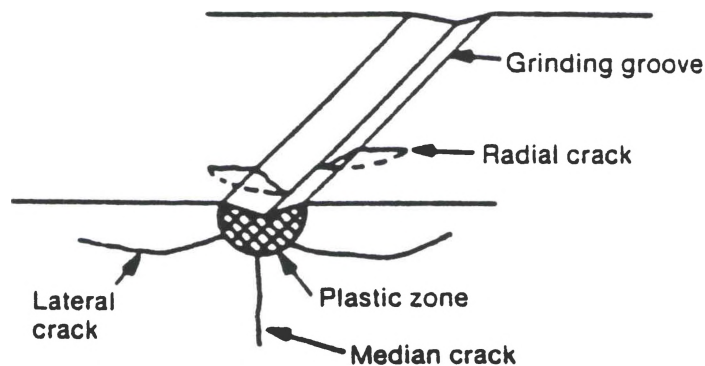
Figure 27. Diagram of cracks and material deformation that occur during grinding with a single abrasive particle [Reference 19].

Note that beneath the groove produced by the abrasive particle a deformed region of material extends radially below the surface and is referred to as the plastic zone. Three types of cracks extending from the plastic zone also appear: lateral cracks run parallel to the surface on both sides of the groove; median cracks open perpendicular to the surface

beneath the plastic zone; and radial cracks open perpendicular to both the groove and the surface, extending away from the plastic zone. The extent of damage caused by grinding in the form of material deformation and cracks determines the degradation in material strength.[16]

Hollstein and Pfeiffer[18] have shown experimentally that the reduced residual surface stresses associated with a smaller plastic deformation in creep feed grinding results in a higher characteristic strength of the material than that machined with conventional grinding techniques. The flexural strength of an MOR specimen is found using a four-point ¼-point bend fixture configuration as shown in Figure 28.
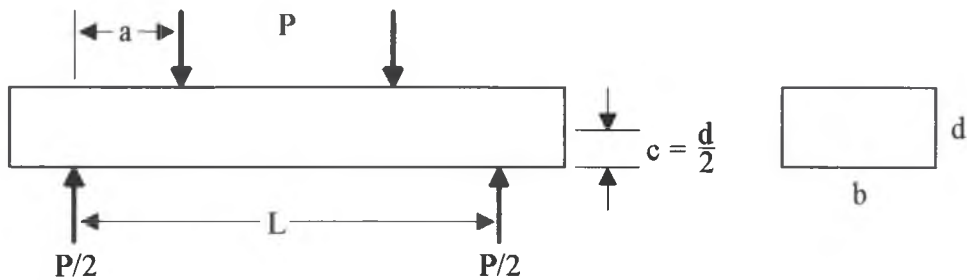
Figure 28. Four-point ¼-point bend fixture configuration for MOR bars.

The term "four-point" means that the fixture comes into contact with the bar at four points. The term "¼-point" means that the horizontal distance between the loading point and support point on one side of the fixture is one-fourth of the total span of the two support points. The flexural strength of the MOR specimen is given by

$$S = \frac{Mc}{I} = \frac{\left(\frac{P}{2}a\right)\left(\frac{d}{2}\right)}{\left(\frac{b\,d^3}{12}\right)} = \frac{3\,P\,a}{b\,d^2} \tag{32}$$

where M is the moment, c is the distance from the neutral axis to the tensile surface, and I is the moment of inertia. The b and d parameters are the specimen width and thickness, respectively. The P parameter represents the loading force on the test specimen. For a rectangular test specimen, $I = \frac{bd^3}{12}$ and $c = \frac{d}{2}$. The parameter a represents the horizontal distance between the loading point on one side and the support point underneath the bar on the same side. This value is typically ¼ of L, the distance between the two supporting points underneath the bar.[19]

Collecting Raman Data

By using the cylindrical optics of the Raman microprobe to focus an elliptical 532 nm line having dimensions of 35 μm by 2 μm onto a specimen surface, Raman spectra were obtained for different positions of the specimen with the CCD array detection system. With the use of micropositioner translation stages, the specimen could be stepped in both directions transverse to the objective optic axis. For the grinding studies of 6H SiC, the specimens were stepped in a plane transverse to the optic axis of the objective and in a direction perpendicular to the laser line's long dimension. The specimens were translated in increments of 25.4 μm (0.001") for a total of 21 runs covering a length of 0.51 mm (0.020"). (By automating the stepping process into smaller steps using an actuator-driven micropositioner, Raman spectra of a grid of positions can be obtained for use in image processing applications.) To obtain a "composite" spectrum of all the positions along the laser line length and to improve the signal-to-noise ratio (SNR), the photoelectrons of the central forty pixel rows of the CCD array were binned together

vertically. This technique provided an average Raman spectrum of that region on the specimen surface. By making 21 runs near the center of the specimen surface in a stepwise fashion, as shown in Figure 29, statistical averages of the Raman shifts, linewidths, and relative strengths of the Raman lines were obtained. A discussion on weighted statistical averaging is given in Appendix E. These data were derived from least squares fitting of each spectrum which yielded the mean and respective uncertainty of each parameter for each Raman line of a given specimen.
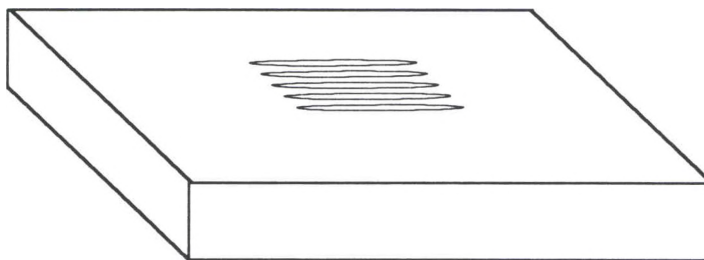
Figure 29. Stepwise statistical sampling of Raman spectra from a specimen in grinding studies.

A three minute exposure and a 50 μm spectrometer entrance slit width were used for each run. The 60x ELWD microscope objective with a 0.7 NA and a 3.49 mm focal length was used for focusing the elliptical laser line onto the specimen surface. The 767 cm^{-1} (E_2), 788 cm^{-1} (A_{1T}/E_2), and 797 cm^{-1} (E_{1T}) modes of 6H SiC were present for all 21 runs of each specimen studied. However, the appearance of the 777 cm^{-1} (E_2) and 783 cm^{-1} (A_{1T}) modes occurred on occasion due to the presence of 4H SiC polytype. The Raman data of these two lines were averaged according to the number of occurrences in the 21 runs.

Results

The analysis results of the Raman spectra from the processed 6H SiC specimens described in the previous section, the Raman shifts and linewidths of the 767 cm^{-1} (E_2), 788 cm^{-1} (A_{1T}/E_2), and 797 cm^{-1} (E_{1T}) Raman modes are compiled in Tables 7 and 8, respectively. The flexural strengths for seven types of processed 6H SiC specimens are listed in Table 9. The Raman shifts and linewidths are also graphed in Figures 30 and 31, respectively.

Table 7. Raman shift measurements of the three main Raman lines in the 790 cm^{-1} region for nine types of processed 6H SiC specimens. The average precision in the Raman shift of the 788 cm^{-1} line, based on fitting uncertainties, was ±0.004 cm^{-1}.

Specimen	767 cm^{-1} Raman Shift (cm^{-1})	788 cm^{-1} Raman Shift (cm^{-1})	797 cm^{-1} Raman Shift (cm^{-1})
As-Sintered	767.14±0.04	788.08±0.02	797.46±0.01
Heat Treated (Baseline/Parallel)	767.25±0.04	788.11±0.03	797.42±0.03
25.4 mm/min Creep Feed	767.16±0.04	788.14±0.03	797.39±0.02
Oxidized (Baseline/Parallel)	767.08±0.02	788.15±0.03	797.42±0.02
88.9 mm/min Creep Feed	767.18±0.03	788.15±0.03	797.40±0.02
Highly Polished	767.16±0.01	788.17±0.02	797.49±0.01
Baseline/Parallel	767.47±0.04	788.33±0.04	797.66±0.04
Baseline/15° Bias	767.39±0.04	788.33±0.03	797.64±0.03
Ultrasonic	767.65±0.04	788.48±0.03	797.69±0.03

Two to three specimens were evaluated from each of the machining treatments. There were eighteen specimens examined representing eight processes with the addition of an as-sintered specimen for reference. There was very little variation in the Raman data for specimens of the same process so that the Raman data for a process was averaged rather than for individual specimens.

Table 8. Raman linewidth measurements of the three main Raman lines in the 790 cm^{-1} region for nine types of processed 6H SiC specimens. The average precision in the Raman linewidth of the 788 cm^{-1} line, based on fitting uncertainties, was ±0.008 cm^{-1}.

Specimen	767 cm^{-1} Raman Linewidth (cm^{-1})	788 cm^{-1} Raman Linewidth (cm^{-1})	797 cm^{-1} Raman Linewidth (cm^{-1})
As-Sintered	4.15±0.07	4.34±0.03	3.52±0.04
Highly Polished	3.93±0.04	4.40±0.03	3.68±0.02
Heat Treated (Baseline/Parallel)	4.4±0.1	4.54±0.07	3.7±0.1
25.4 mm/min Creep Feed	4.49±0.07	4.64±0.04	3.95±0.04
88.9 mm/min Creep Feed	4.51±0.08	4.66±0.05	3.94±0.05
Oxidized (Baseline/Parallel)	4.4±0.1	4.74±0.05	4.08±0.05
Ultrasonic	4.9±0.1	4.95±0.06	4.5±0.1
Baseline/Parallel	5.5±0.1	5.27±0.08	4.7±0.1
Baseline/15° Bias	5.34±0.09	5.29±0.05	4.55±0.07

Table 9. Flexural strengths for seven types of processed 6H SiC specimens.[a]

Specimen	Flexural Strength (MPa)
Heat Treated (Baseline/Parallel)	418±6
Oxidized (Baseline/Parallel)	410±10
Baseline/15° Bias	387±5
Baseline/Parallel	380±10
1.0"/min Creep Feed (Parallel)	370±10
3.5"/min Creep Feed (Parallel)	370±10
Ultrasonic Grind	361±4

[a] Reference 20.

Distinct differences in the Raman data were observed for different processes, as when comparing the larger Raman shifts and linewidths from baseline grind specimens with the smaller Raman shifts and linewidths from as-sintered and highly polished specimens. These differences are attributed to differences in residual surface stress caused by surface processing of the specimens.
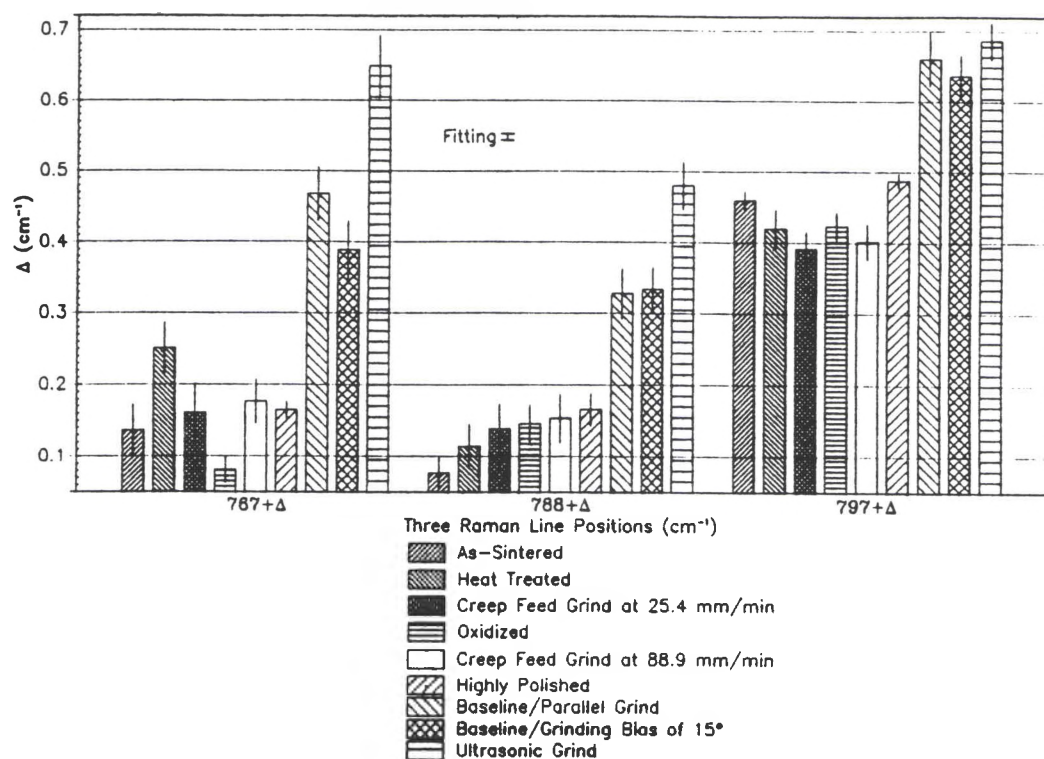
Figure 30. Raman shift measurements of the three main Raman lines in the 790 cm^{-1} region for nine types of processed 6H SiC specimens.
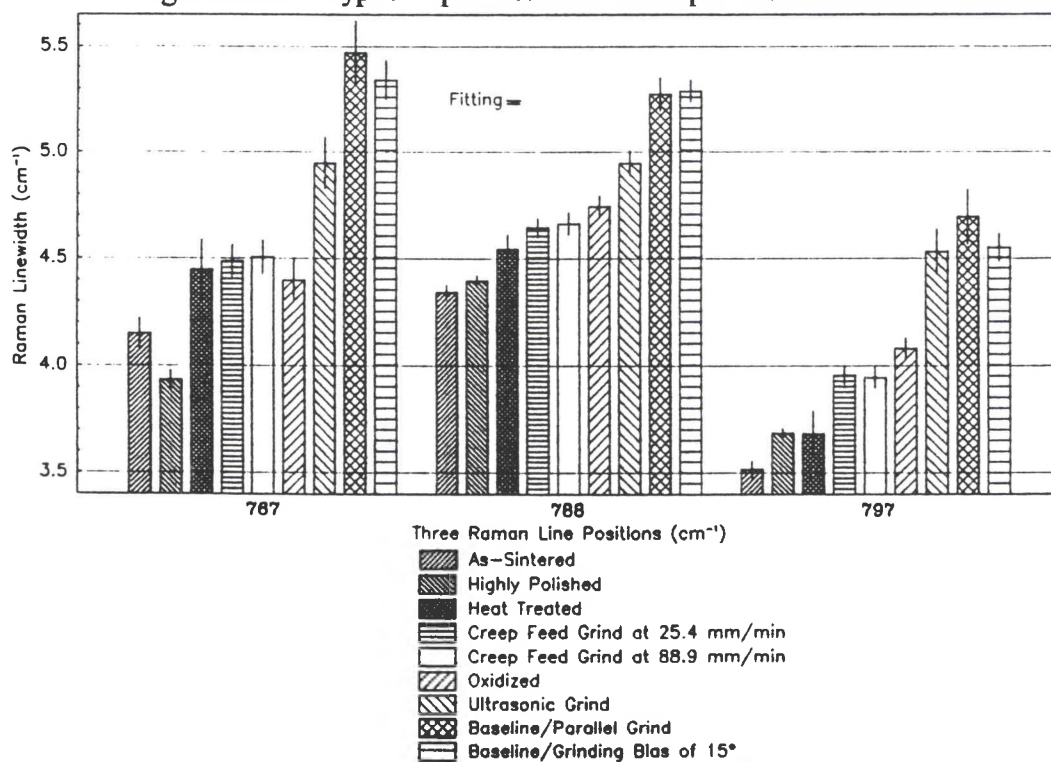
Figure 31. Raman linewidth measurements of the three main Raman lines in the 790 cm^{-1} region for nine types of processed 6H SiC ceramic specimens.

The more damage introduced by a grinding process, the more material deformation, resulting in higher compressive strains on the individual crystallites in the polycrystalline material. Raman lines tend to shift linearly away from the laser line toward higher frequencies with increasing compressive strain on the crystallite structure. In addition, the linewidths of these lines tend to broaden for several reasons. First, the Raman lines tend to broaden as they shift to higher frequencies since the increasing compressive strain reduces the symmetry in the crystallite structure, causing a broadening in the frequency band of each Raman mode. Second, the crystallites taken as a whole have a distribution of compressive strains which act to broaden the lines in the composite Raman spectrum. A third factor discussed in the laser penetration depth studies is that the composite Raman spectrum is integrated over the depth in which the laser light penetrates. The resultant spectrum is highly dependent on the damage profile of the material and varies with incident wavelength since longer wavelength light penetrates more deeply. If the relationship between wavelength and penetration depth is known, then the use of several incident wavelengths allows the determination of the actual Raman linewidths and the corresponding relative residual stresses as a function of depth beneath the surface.

Figures 30 and 31 show that creep feed grinding produces lower residual stresses than baseline grinding. Earlier, it was mentioned that each cutting edge in creep feed grinding produces a smaller force on the workpiece material, causing smaller chip thicknesses and a lower depth of cut by each cutting edge. This process minimizes the loss in strength caused by larger amounts of damage which lead to higher residual surface stresses. The baseline specimens which were heat treated or oxidized exhibit still lower

amounts of residual surface stress, probably since the heat treatment anneals cracks and flaws in the surface, thus relieving residual surface stresses. The thicker oxide layer of the oxidized specimen appears to reintroduce added surface stresses due to the difference in the coefficient of expansion between the oxide layer and the specimen surface. Also, with time and temperature cycling, oxidized specimens tend to exhibit pitting and devitrification, a process in which crystallite precipitates occur in the glassy oxide layer. Both processes contribute to the added residual surface stresses. However, the ultrasonic grind specimen appears to have highest amounts of residual stress, apparent from the large Raman shift, yet the linewidth is smaller than that of the baseline grind specimens, indicating that the variation in the residual surface stress was fairly small.

In order to more clearly understand the effect machining has on the residual surface stresses of 6H SiC, an analysis of just the 788 cm^{-1} (A$_{1T}$/E$_2$) mode was conducted because of its large line strength and stability, making experimental measurements less subject to systematic errors than those of the 767 cm^{-1} or 797 cm^{-1} Raman lines. The Raman shift and linewidth data of the 788 cm^{-1} line for eight processes are graphed in Figure 32 and Figure 33, respectively, relative to data from the as-sintered specimen. The trends in the Raman shifts and linewidths are the same here as they were in Figures 30 and 31 with regard to the residual surface stress produced by each type of process. As mentioned earlier, the material strength is inversely related to the residual stress present in the surface. The Raman shifts and linewidths of the 788 cm^{-1} Raman line for seven processes are graphed as a function of flexural strength in Figure 34 and Figure 35, respectively.
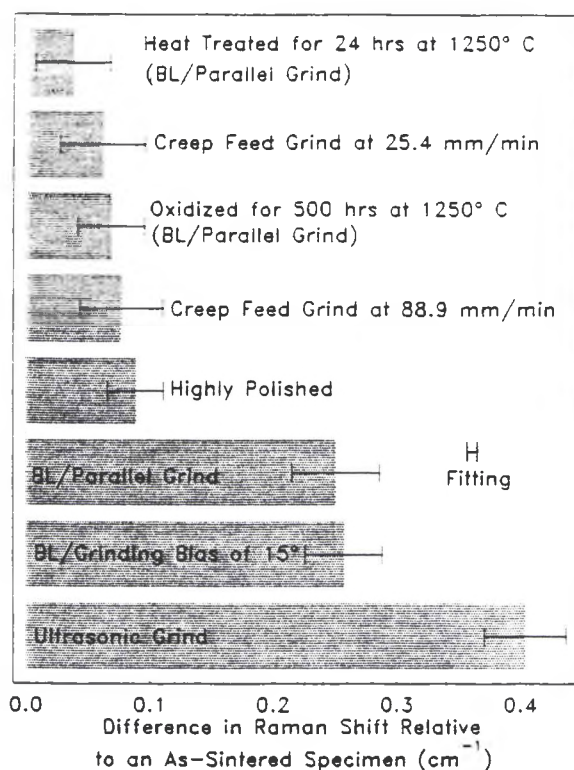
Figure 32. The 788 cm⁻¹ Raman line positions of eight processed 6H SiC specimens relative to an as-sintered specimen.
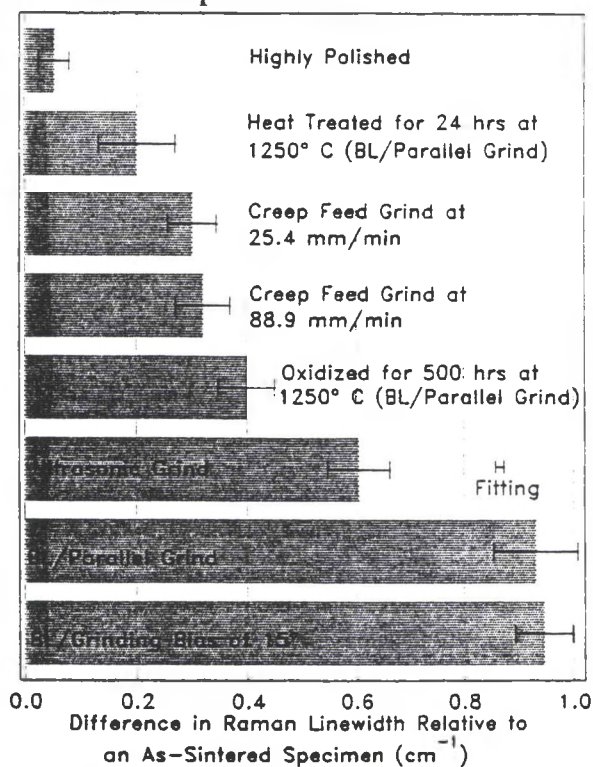
Figure 33. The 788 cm⁻¹ Raman linewidths of eight processed 6H SiC specimens relative to an as-sintered specimen.
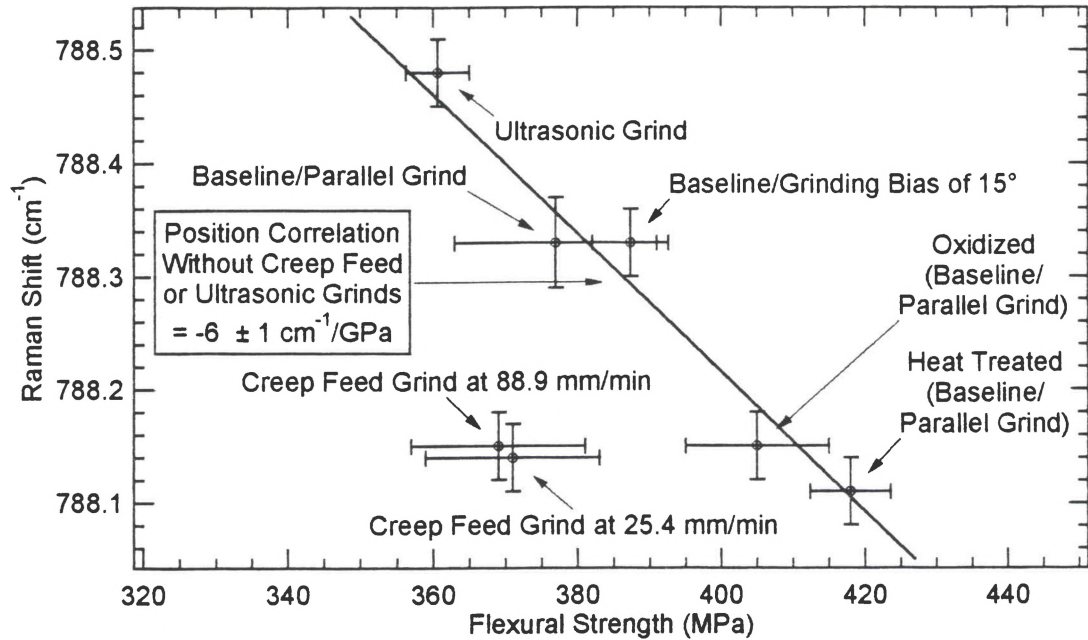
Figure 34. Correlation of the 788 cm^{-1} Raman shift with the flexural strength of seven types of 6H SiC specimens.
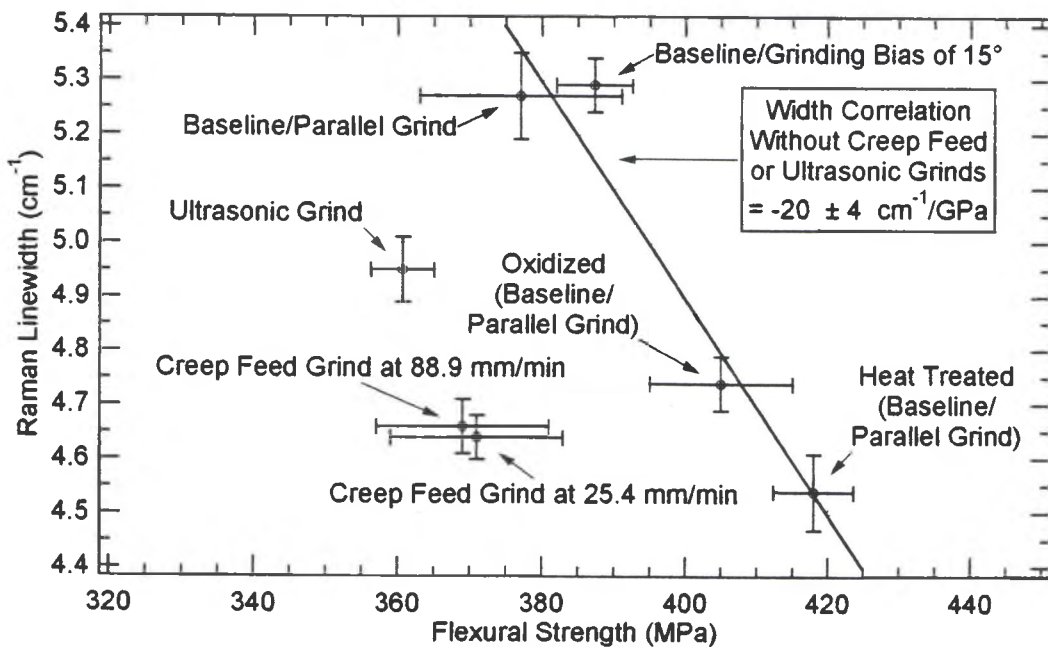
Figure 35. Correlation of the 788 cm^{-1} Raman linewidths with the flexural strength of seven types of 6H SiC specimens.

The flexural strength data of the as-sintered and highly polished specimens were unavailable at the time of this study.

The flexural strength of a material is the maximum tensile stress at the surface a modulus of rupture (MOR) bar can withstand at failure in the four-point-¼-point bend fixture.[19] Since the relative residual surface stresses due to machining can indicate the degradation in material strength, flexural strength data may be used for correlation. In addition to the uncertainties for each point in Figures 34 and 35, a correlation line is drawn for four baseline process specimens. The Raman shift/flexural strength correlation of Figure 34 is -6±1 cm^{-1}/GPa and the Raman linewidth/flexural strength correlation of Figure 35 is -20±4 cm^{-1}/GPa. These four processes are baseline grind parallel to the specimen long axis, baseline grind at a 15° bias to the specimen long axis, parallel baseline grind with oxidation, and parallel baseline grind with heat treatment. The flexural strength increases (and the relative residual surface stress decreases) with this ordering of processes. The ultrasonic grind and the two creep feed grind processes in general do not fall on this correlation (although the Raman shift of the ultrasonic grind does line up with the baseline correlation). The linewidth from the ultrasonic grind process may not fall on the correlation due to a reduced variation of the residual surface stress caused by uniformity in the up and down pounding of abrasive particles during ultrasonic grinding. The creep feed grind processes may form different correlations due to the difference in damage zones produced by creep feed and conventional grinding processes. The research of Hollstein and Pfeifer[18] support this assertion by graphing the damage distributions of

Al$_2$O$_3$ caused by different machining processes as shown in Figure 36. Note that the damage caused by conventional grinding is much deeper than that of creep feed grinding.
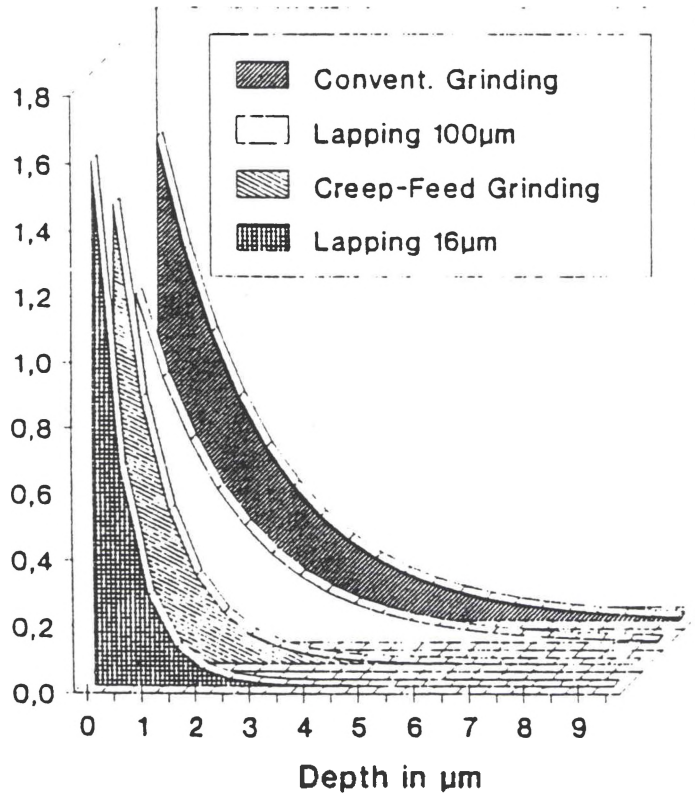
Figure 36. Damage distribution in the sub-surface area of Al$_2$O$_3$ [Reference 15].

Further support of this explanation is provided in Chapter V covering a comparison of the conventional and creep feed grind results using the Ar ion 488 nm wavelength for a smaller penetration depth, revealing the larger amounts of damage from each method closer to the surface. Overall, from Figures 34 and 35, creep feed grinding produces less residual surface stress than conventional grinding. However, when the baseline specimens were heat treated or oxidized, the amount of residual surface stress was greatly reduced, resulting in an increased flexural strength. Both processes reduce the residual surface stress due to the annealing of cracks and flaws. However, the oxidation process appears

to reverse the trend slightly by reintroducing added residual surface stresses caused by the difference in the coefficient of expansion between the oxide layer and the specimen surface and by other effects such as pitting and devitrification. Based on these studies, if creep feed grind specimens were to undergo the same heat treatment or oxidation processes, a similar reduction in residual surface stress along with an increase in flexural strength would be observed.

CHAPTER V

OTHER STUDIES OF 6H SILICON CARBIDE

Comparison of Hexoloy SA SiC Vintage 1995 With Hexoloy SA SiC Vintage 1988

Several Raman spectra were taken of Hexoloy SA SiC Vintage 1988, the manufactured specimens researched by Jennings.[21] This study was conducted namely to confirm the similarity of the Raman spectra with that shown in his experimental data and also to demonstrate that both manufactured specimens were hexagonal SiC due to the resemblance in Raman spectra. This study adequately demonstrated that both manufactured specimens were hexagonal SiC.

General Survey of the 790 cm^{-1} Raman Spectral Region of 6H SiC Using Different Experimental Configurations

A study of the three main Raman modes in the 790 cm^{-1} region of 6H SiC was performed for a variety of experimental conditions in order to note any differences in the Raman spectra. Later research revealed that the Raman shifts and linewidths of the 788 cm^{-1} (A_{1T}/E_2) line were slightly smaller for creep feed machined specimens than for those machined using baseline grinding. Differences in the Raman spectra at different positions on the same specimen can be attributed to statistical variations in the orientations and positions of the grains, surface defects, and surface profile variations. The differences

73

in the Raman spectra due to the polarization configuration of the incident and scattered light (parallel or crossed) were negligible due to the random orientation of the c-axis of each crystallite in the polycrystalline material and to the multiple paths taken by the incident and scattered light resulting from the grain boundaries. This study revealed the statistical nature of the Raman data for different positions on the specimen surface and the absence of orientational or polarization dependence. However, the study also confirmed differences in the Raman data which can be attributed to differences in the residual surface stresses due to different machining methods.

Study of the 790 cm^{-1} Raman Spectral Region From the Unprocessed Ends of Some 6H SiC Specimens

Studies of the ends of several specimens were conducted to obtain Raman spectra of unprocessed ceramic material to be used as a "reference" for changes in the Raman shift and linewidth of Raman lines evident in the spectrum of processed ceramic material. This effort was an attempt to arrive at a measure of the relative residual surface stress due to machining. The ends of the specimens were broken but not machined. This study was conducted before an as-sintered (unprocessed) specimen was obtained. The procedure in this study involved taking a series of runs which "mapped" the central region of the specimen end. Raman shift and linewidth data could then be averaged to obtain "composite" Raman data to be used as a reference. Unfortunately, due to the rough surface profile, fluorescence regions (which greatly increase the background and reduce the SNR), random grain orientations, and random surface stresses, the collected Raman

data did not yield very favorable results when compared with spectra obtained from the as-sintered specimen. Seventeen runs in a "star" grid pattern were made on the ends of both the baseline and 88.9 mm per minute creep feed grind specimens, as shown in Figure 37.
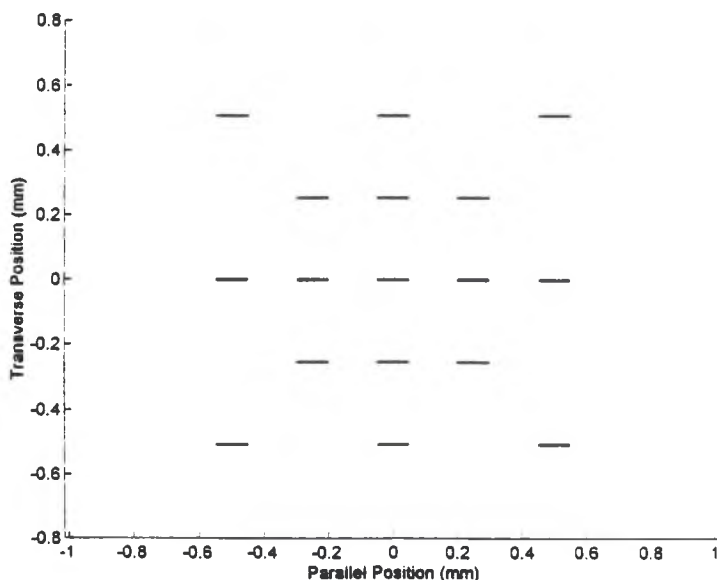
Figure 37. "Star" grid pattern of runs performed on the ends of two 6H SiC specimens. The narrow horizontal rectangles depict the position and orientation of the line of laser light illumination and its polarization.

The grid was 1 mm on a side with horizontal and vertical spacings of 0.25 mm. The runs were performed using 532 nm laser light. The incident light was focused using a 60x ELWD microscope objective. The runs had an exposure time of three minutes and the spectrometer entrance slit was set to 50 μm.

Although not very favorable when compared with the results from the as-sintered specimen, the Raman shift and linewidth data of the 788 cm^{-1} line were plotted as a function of position on the unprocessed ends of two specimens as shown in Figure 38 and Figure 39, respectively.
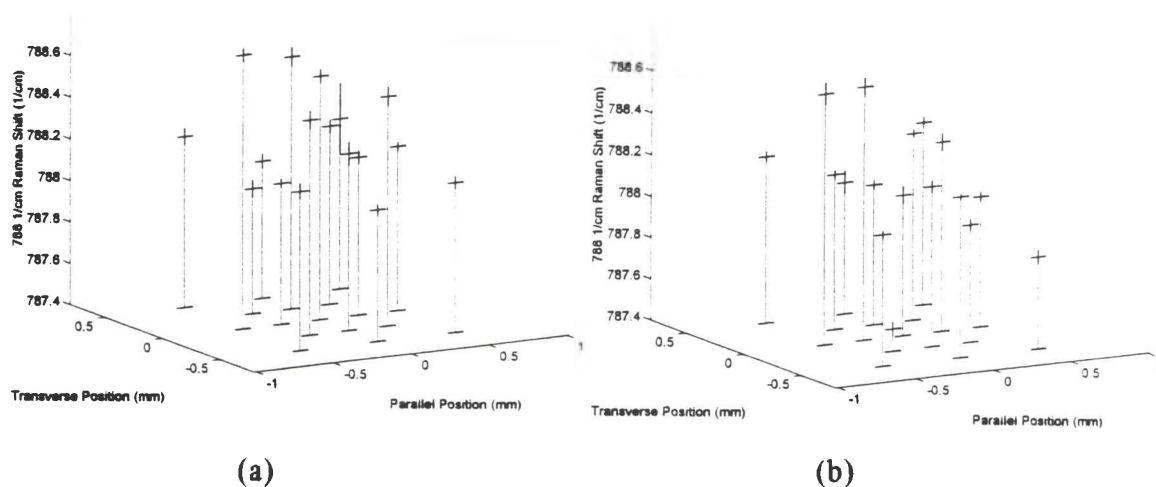
Figure 38. The 788 cm⁻¹ Raman shift mapping over the unprocessed ends of (a) the first and (b) the second of two 6H SiC specimens. The horizontal lines depict both the line of laser illumination and the Raman shift values while the dark vertical lines define the uncertainty in each of these values.
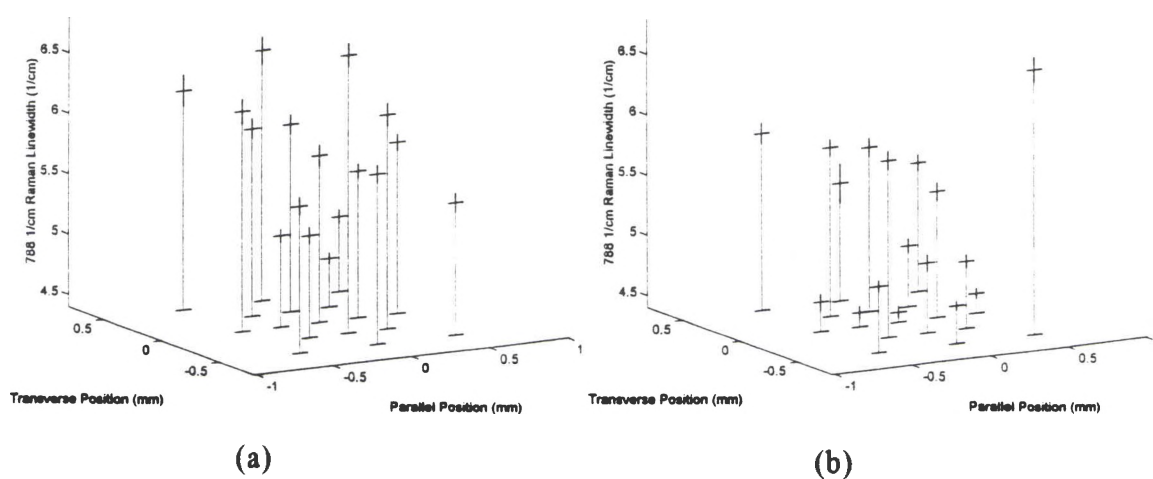
Figure 39. The 788 cm⁻¹ Raman linewidth mapping over the unprocessed ends of (a) the first and (b) the second of two 6H SiC specimens. The horizontal lines depict both the line of laser illumination and the linewidth values while the dark vertical lines define the uncertainty in each of these values.

The statistical average of the Raman shift and linewidth measurements was

788.17±0.03 cm^{-1} and 5.2±0.1 cm^{-1}, respectively. For comparison, the Raman shift and

linewidth measurements for an as-sintered 6H SiC specimen was 788.08±0.02 cm^{-1} and

4.34±0.03 cm^{-1}, respectively. The average Raman shift of this study was not much larger

than that of the as-sintered specimen. However, the linewidth was much broader than that

of the as-sintered specimen, indicating that the as-sintered specimen serves as a much

better reference for comparison to machined specimens.

Study of the Presence of 4H SiC Polytype in a 6H SiC Specimen

The appearance of the 777 cm^{-1} (E$_2$) mode characteristic of 4H SiC polytype

prompted a study of the extent of its presence along the surface of a 88.9 mm per minute

creep feed grind specimen. The cross-like pattern of these runs is shown in Figure 40.
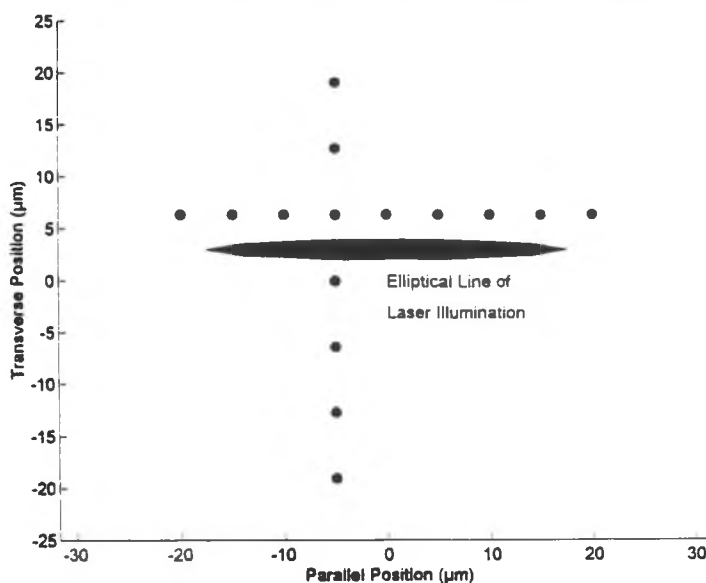
Figure 40. "Cross" grid pattern of runs performed on a 6H SiC ceramic specimen to examine the presence of 4H SiC polytype. The "dots" denote the positions of the runs and the narrow horizontal elliptical line denotes the orientation and polarization of the line of laser light illumination at each "dot."

Raman spectra of the positions transverse to the bar long dimension are shown vertically and those taken of positions parallel to the bar long dimension are shown horizontally. The spacing of these positions transverse to the long dimension was approximately 6.4 μm and the spacing parallel to the long dimension was approximately 5 μm. The extreme points of the cross pattern represent the positions at which the 777 cm^{-1} line no longer appeared. This study was used to estimate the size of the local region containing 4H polytype near the specimen surface. An elliptical line of 532 nm laser light was focused at each position of the surface using the 60x ELWD microscope objective. A three minute exposure was made at each point using a 50 μm spectrometer entrance slit width. Based on research conducted by Nakashima et al.,[20] the appearance of the 777 cm^{-1} (E_2) mode indicates the presence of 4H SiC polytype, as mentioned in the single crystal studies of Chapter IV. The 783 cm^{-1} (A_{1T}) mode was probably not observed since it is typically much weaker based on these single crystal studies. The Raman shift, linewidth and relative intensity of the 777 cm^{-1} (E_2) mode is graphed as a function of position in Figures 41(a), 41(b), and 41(c), respectively. Note how the intensity of the Raman line peaks near the center of the cross pattern, indicating the central location of the 4H polytype presence. The extent of this region is approximately 40 μm in each direction. This study revealed that the occurrence of 4H polytype in this specimen was fairly localized. The Raman shift and linewidth data stayed fairly the same throughout the region. Further studies could reveal more about the density of the 4H polytype at these sites and the density of these sites over the entire surface of specimens.
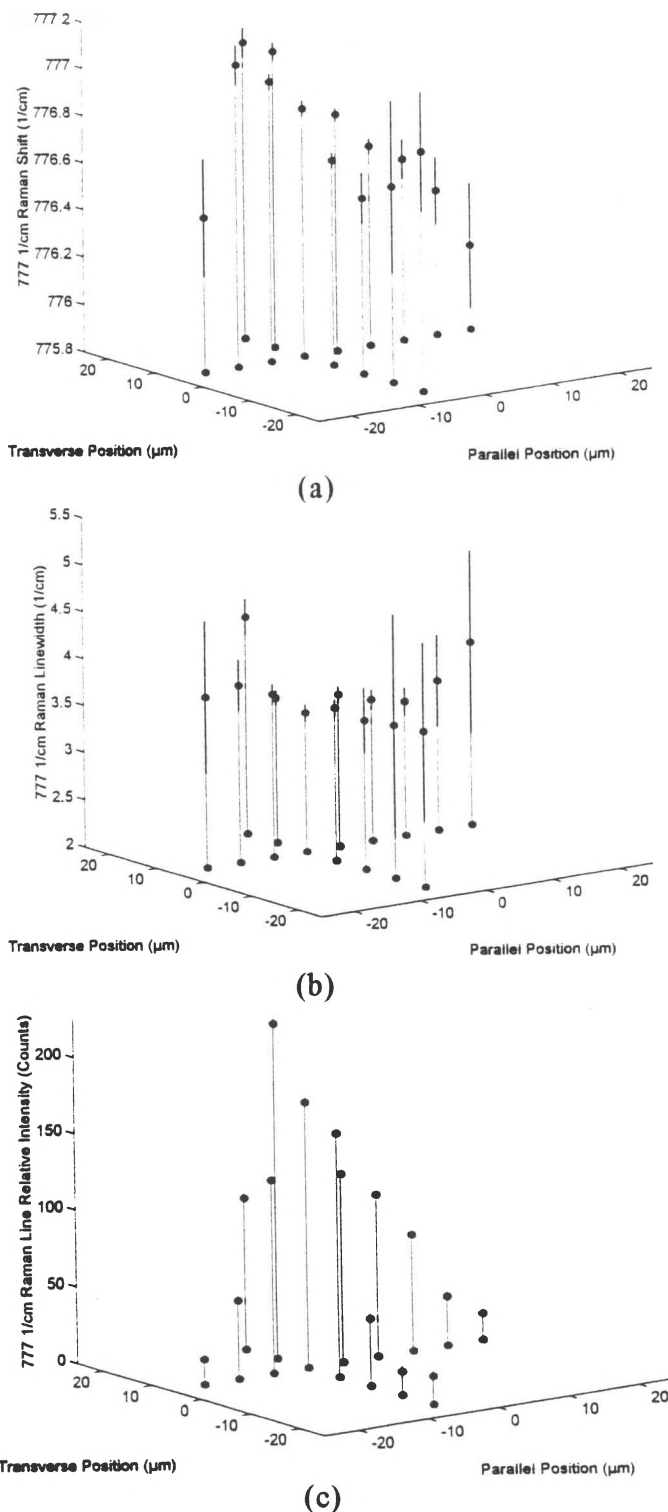
Figure 41. The 777 cm⁻¹ (a) Raman shift, (b) linewidth, and (c) relative intensity mappings of a 4H SiC polytype region of a 6H SiC specimen. The horizontal lines depict the line of laser illumination at the specimen surface and the "dots" with dark vertical lines through their centers define the values with respective uncertainties.

Laser Penetration Depth Studies on 6H SiC

A study of the Raman modes in the 790 cm^{-1} region was conducted on the unprocessed side of a 6H SiC specimen using six wavelengths of the Ar ion laser. Statistically significant data were not obtained since a single run was obtained at each wavelength. However, the study was still useful in that atomic lines of several discharge lamps were identified as reference lines in three critical spectral regions of 6H SiC for each wavelength: at the laser line (0 cm^{-1}); at the transverse optic region (760 cm^{-1}-800 cm^{-1}); and at the longitudinal optic region (970 cm^{-1}). The rationale for this study comes from the knowledge that the damage profile (the plastic zone) is a decreasing function with depth beneath the surface. This effect results from the fact that the grinding process introduces greater damage in a material closer to the surface.[23]

Laser light penetrates the surface of the material based on the extinction coefficient of the material. The intensity falloff can be described by

$$I(z) = I_0 \exp\left[-\alpha(\lambda, d) \cdot z\right] = I_0 \exp\left[-z/\tau\right] \tag{33}$$

where I_0 is the intensity at the surface, z is the depth beneath the surface, λ is the wavelength, d is the grain size of the material, α is the extinction coefficient due to absorption and scattering, and τ is the penetration depth of the laser light. As can be seen in Equation (33), the penetration depth τ is typically defined as the inverse of the extinction coefficient α. Since light penetrates more deeply into materials at longer wavelengths, the extinction coefficient α decreases with increasing wavelength. Also, since materials of larger grain size have an overall lower density, light can penetrate these materials more deeply than for materials having a smaller grain size. Therefore, the

extinction coefficient α decreases with increasing material grain size d. The strain distribution is a decreasing function which sometimes is described by a simple exponential decay given by

$$S(z) = S_0 \exp(-\rho z) \tag{34}$$

where S_0 is the strain at the surface and ρ is the strain falloff. Based on a discussion by Pfeiffer,[23] the total strain distribution $S_T(\tau)$ representing the integrated strain distribution seen by X-ray diffraction techniques and weighted by the absorption exponential function for X-ray penetration is given by

$$S_T(\tau) = \frac{\int_0^\infty S(z)I(z)dz}{\int_0^\infty I(z)dz} = \frac{\int_0^\infty S(z)\exp(-z/\tau)dz}{\int_0^\infty \exp(-z/\tau)dz} \tag{35}$$

Using the simple exponential decay for the strain distribution given in Equation (34), we obtain an integrated strain distribution $S_T(\tau)$ given by

$$S_T(\tau) = \frac{S_0}{\rho\tau + 1} \tag{36}$$

so that $S_T(0)=S_0$, the strain at the surface. Equation (34) can be rewritten in terms of the penetration depth τ.

$$S(\tau) = S_0 \exp(-\rho \tau) \tag{37}$$

Solving for the product $\rho\tau$ in Equation (36) and substituting this expression into Equation (37), we obtain the actual strain distribution in terms of the integrated (measured) strain distribution:

$$S(\tau) = S_0 \exp\left[1 - \frac{S_0}{S_T(\tau)}\right] = S_T(0)\exp\left[1 - \frac{S_T(0)}{S_T(\tau)}\right] \tag{38}$$

Thus, by measuring the relative residual stresses in materials as a function of wavelength and by knowing the relationship between the wavelength and its penetration depth into the

material, an accurate description of the integrated strain distribution may be obtained. The actual strain distribution of the material may then be computed.

The information gained from this penetration depth study is included in Table 10. Essentially, the atomic line wavelengths useful as references in the $0\ cm^{-1}$, $760\ cm^{-1}$-$800\ cm^{-1}$, and $970\ cm^{-1}$ regions from each laser line are listed for future use. If the laser wavelength and wavelength dispersion of each region are accurately determined, then twenty or more spectra for each wavelength may be obtained to determine the statistical measures of the relative residual stresses as a function of penetration depth. The reference atomic lines were selected assuming a maximum spectral range on the CCD array of $70\ cm^{-1}$.

Raman spectra from 21 runs using the 488 nm line of the Ar ion laser on both baseline grind and 88.9 mm per minute creep feed grind 6H SiC specimens were examined for comparison with those obtained using 532 nm laser light from the Nd:YAG laser. Neon atomic spectral lines were used to determine the Ar ion 488 nm wavelength and the wavelength dispersion at the $790\ cm^{-1}$ region for 6H SiC. The 488.49170 nm and 489.21007 nm neon lines were used to determine the laser wavelength. The 507.42007 nm and 508.03852 nm neon lines were used to determine the wavelength dispersion in the $790\ cm^{-1}$ region. The spectrometer entrance slit width was 50 µm and the exposure was three minutes for each run. The incident light was focused using the 60x ELWD microscope objective and the stepping interval along the specimen surface was 25.4 µm (0.001"). The results from this study, along with data obtained using the 532 nm Nd:YAG laser, are summarized in Table 11.

Table 10. Reference atomic lines used in several spectral regions of 6H SiC for the laser penetration depth study.

λ (nm)	ν (cm⁻¹)	reference lines[a] at 0 cm⁻¹	reference lines[a] at 780 cm⁻¹	reference lines[a] at 970 cm⁻¹
457.936 (Ar ion laser)	21,837.11	Ne 457.50620 Ne 458.2035 Ne 458.24521	Ne 474.95754 Ne 475.27320	Ne 478.89270 Ne 479.0217
476.488 (Ar ion laser)	20,986.89	Ne 474.95754 Ne 475.27320	Ne 494.49899 Ne 495.70335 Ne 495.7123	Ne 499.4913 Ne 500.51587 Ne 501.1003
487.9865 (Ar ion laser)	20,492.370	Ne 488.49170 Ne 489.21007	Ne 507.42007 Ne 508.03852	Ne 510.47011 Ne 511.36724 Ne 511.65032 Ne 512.22562
496.509 (Ar ion laser)	20,140.62	Ne 495.70335 Ne 495.7123 Ne 497.3538	Ar 516.22847 or Xe 516.2711 **For D_λ** Ne 515.0077 Ne 515.19610 Ne 515.44271 Ne 515.66672 Ne 515.89018	Ne 520.38962 Ne 520.88648 Ne 521.05672 Ne 521.43389 Ne 522.23517 Ne 523.40271
501.717 (Ar ion laser)	19,931.56	Ne 500.51587 Ne 501.1003 Ne 502.2864 Ne 503.13504 Ne 503.5989	Ne 522.23517 Ne 523.40271	Ne 527.40393 Ne 528.00853
514.527 (Ar ion laser)	19,435.33	Ne 514.49384 Ne 515.0077 Ne 515.19610 Ne 515.44271 Ne 515.66672 Ne 515.89018	Ar 537.34951 **For D_λ** Ne 536.00121 Ne 537.23110 Ne 537.49774	Ar 541.04750 Ar 542.13492 **For D_λ** Ne 540.05616 Ne 541.26490 Ne 541.85584
532.10364 (Nd:YAG laser)	18,793.3275	Ne 533.07775 Ne 534.10938	Ne 556.27662 **For D_λ** Xe 555.2385 Xe 556.6615	Ar 560.67328 **For D_λ** Ar 558.87213 Ar 559.74783

[a] Reference 14.

Table 11. Raman shift and linewidth measurements of the 788 cm^{-1} Raman line of creep feed and baseline grind specimens using 488 nm and 532 nm wavelengths.

Specimen	767 cm^{-1} Raman Shift (cm^{-1})	767 cm^{-1} Linewidth (cm^{-1})	788 cm^{-1} Raman Shift (cm^{-1})	788 cm^{-1} Linewidth (cm^{-1})	797 cm^{-1} Raman Shift (cm^{-1})	797 cm^{-1} Linewidth (cm^{-1})
88.9 mm/min Creep Feed (532 nm)	767.18 ±0.03	4.51 ±0.08	788.15 ±0.03	4.66 ±0.05	797.40 ±0.02	3.94 ±0.05
88.9 mm/min Creep Feed (488 nm)	767.06 ±0.03	3.69 ±0.08	788.31 ±0.04	4.88 ±0.06	797.56 ±0.04	3.60 ±0.05
Baseline/ Parallel (532 nm)	767.47 ±0.04	5.5 ±0.1	788.33 ±0.04	5.27 ±0.08	797.66 ±0.04	4.7 ±0.1
Baseline/ Parallel (488 nm)	767.45 ±0.07	4.0 ±0.1	788.44 ±0.04	5.7 ±0.1	797.74 ±0.05	4.7 ±0.2

These results are graphed in Figure 42, which demonstrates the Raman shift and linewidth of the 788 cm^{-1} line as a function of wavelength for both the baseline and creep feed grind specimens. Note how the relative residual stress decreases with increasing wavelength (or increasing penetration depth). This result confirms the assertion that baseline grinding creates a deeper damage zone than does creep feed grinding.

Fluorescence Studies of 6H SiC Specimens

Throughout the research on 6H SiC specimens, it was observed that certain regions at the surface of the specimens (or to be more accurate, within the penetration depth of the illuminating light) exhibited unusually high backgrounds (reducing the SNR of the Raman spectra) in the 790 cm^{-1} region using CCD array detection.
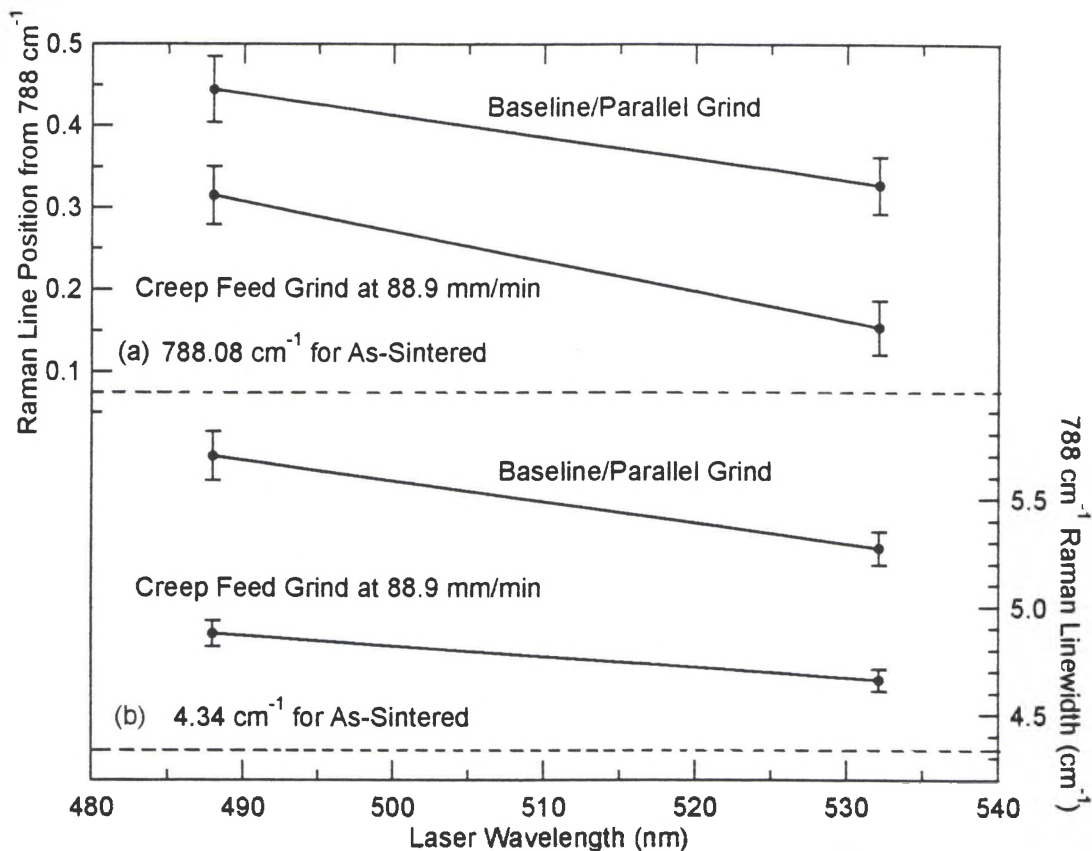
Figure 42. The 788 cm^{-1} (a) Raman shift and (b) linewidth as a function of wavelength for both baseline and creep feed grind 6H SiC specimens. Note that the dashed lines represent the values for an as-sintered specimen.

A broadband background which increased with wavelength was also observed in some survey spectra using the PMT detection system. These high backgrounds were attributed to fluorescence in the material caused by regions containing trace amounts of rare earths or other materials which are known to fluoresce. An excellent example of this effect is shown in Figure 43, where survey spectra of both fluorescence and non-fluorescence sites of a 6H SiC specimen were made using a ten second count time, 200 μm entrance/exit slits on the 1877 Triplemate spectrometer, and an elliptical line of 532 nm light focused onto an unmachined face using the 60x ELWD microscope objective. Note the broadband regions which could be used to identify the fluorescing material.
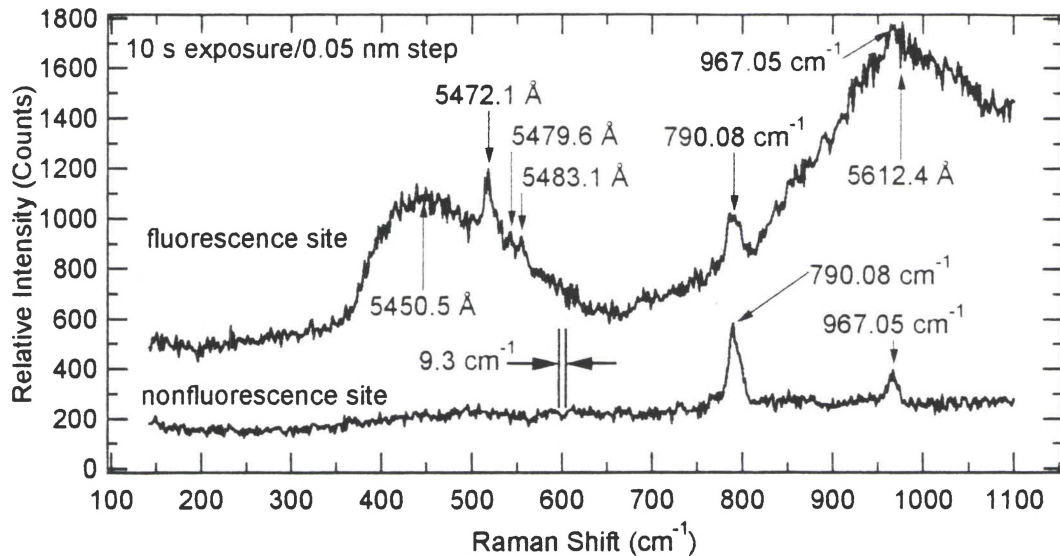
Figure 43. Survey spectra of both (a) fluorescence and (b) non-fluorescence sites on a 6H SiC specimen.

Unfortunately, efforts to repeat these measurements were for the most part unsuccessful. Moreover, the fluorescence features in Figure 43 could not be identified unambiguously. Due to the small locality of these fluorescence sites (typically 30 μm or less), positioning of the translation stages is often difficult due to operator error in positioning the specimen reference corner, backlash or "play" in the stages themselves, and other positioning factors. Often, a fluorescence site was observed by looking for regions in which the incident laser line induced the surrounding region to "light up." This effect was observed often for creep feed grind specimens and was prominently noticed by dousing the white light illumination so that the orange-red fluorescence could be observed in addition to the scattered laser light. Usually, the fluorescence occurred at smooth "glassy" regions which were about 20 μm in size. These regions would "light up" as the illumination moved closer. Fluorescence at neighboring regions from the illumination

occurred from a "channeling" effect of the light within the surface layer of 6H SiC in which the light penetrated. The grain boundaries could act as tiny multi-faceted mirrors, scattering light in all directions beneath the surface. Another source of these fluorescent materials may be from the grinding wheel itself. Trace amounts of fluorescent material may originate from abrasive particles used in the grinding wheel. Fluorescence sites were sometimes "hunted" by looking for regions which "light up" near the area of illumination, but spectra of these regions did not always reveal the presence of fluorescence. In addition, the "lighting up" effect observed in these regions appeared to fade with time during illumination, indicating that the fluorescence effect dissipates or "bleaches" with prolonged illumination. Other studies of the fluorescence effect were conducted using the PMT detection system, but no conclusive results were obtained.

More study of this effect in 6H SiC must be conducted to adequately characterize the fluorescence behavior. The study should concentrate on accurately recording the positions of fluorescence and confirmation of the locations of these fluorescence sites through repeated measurements. Survey scans of these regions could then reveal fluorescence patterns in the spectra characteristic of certain materials. While for many experiments fluorescence is a nuisance to be avoided, these studies could lead to the regular detection of trace substances present during the manufacture of SiC and help to eliminate contaminants introduced during the manufacturing/machining process.

CHAPTER VI

PROTOTYPE GALVANOMETER SCANNER FOR
THE RAMAN MICROPROBE SYSTEM

Operation and Considerations For Computer Control

Based on a proposal by Ernst and Yaney,[13] the addition of a scanner into the

Raman microprobe system was considered. The previous system consisted of a cylindrical

optics configuration for focusing an elliptical line of laser light onto the specimen surface.

This line was typically 35 μm by 2 μm wide. A line of illumination was used to avoid

excessive specimen heating, yet the small width allows high spatial resolution in one

dimension for measuring the relative residual surface strains evident from Raman spectra.

The scanner technique allows for the acquisition of spectra for each position along the

length of illumination using the CCD array detector. If the corresponding spectra from

these positions were binned together, a "composite" spectrum from the illuminated region

would be obtained, representing the statistical average for that region and the equivalent

of the elliptical line illumination technique.

A scanner system has several advantages over the cylindrical optics system.

First, the system would linearly scan a focused laser spot 1 to 2 μm in diameter over the

specimen surface. This technique would uniformly illuminate the scanned region, whereas

the nonuniformity in the laser line illumination method is due to its Gaussian irradiance

profile. The scanner system would also reduce specimen heating since the scanning can be computer controlled. A galvanometer scanning system was selected because of its high precision and its adaptability to computer control.

In the microprobe system, laser light is focused onto the specimen with a microscope objective lens which also collects the Raman scattered light. The scattered light passes through the same objective in the opposite direction to the incoming laser light. The laser light is inserted into the 180° backscattering configuration by means of a 70/30 (transmission/reflection) beam splitter oriented at 45° above the objective which directs the laser light into the objective and passes the "back" scattered light on to the spectrometer and detector. For the scanning system, a modified scanner element was proposed to replace the 70/30 beam splitter. This scanner element would consist of a glass window with a central elliptical mirror "spot" which could reflect more than 90% of the incident laser light onto the specimen and transmit about 98% of the scattered light that lies outside of the mirror boundary. In this design, the mirror spot would be made as small as possible to optimize transmission of the scattered light. The clear surfaces would be AR-coated to avoid Fabry-Perot interference effects. For the Raman microprobe system, the AR-coatings will be designed for s-light (polarized orthogonal to the plane of incidence) at 45° incidence using a 523 nm wavelength (this wavelength is midway between the 532 nm light of the Nd:YAG laser and the 514.5 nm light of the Ar ion laser). The s-light design polarization was selected since, in the Raman microprobe system, the laser beams from both the Nd:YAG and the Ar ion lasers are s-polarized at the beam splitter. The galvanometer scanner system is illustrated in Figure 44.
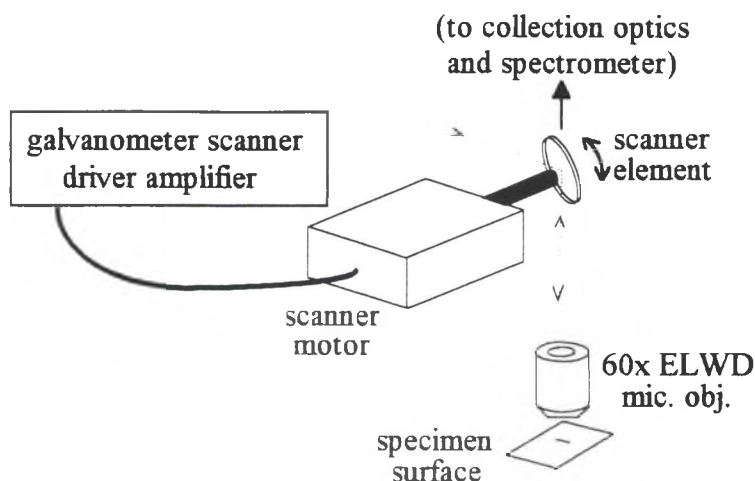
Figure 44. Galvanometer scanner system of the laser Raman microprobe.

As shown in Figure 44, the laser spot is scanned along the specimen surface in a line contained in the plane of incidence defined by the laser light on the scanner element. Since the scan direction projects perpendicular to the slit long dimension, a dove prism rotated about its axis by 45° is used to rotate the scan line and its polarization by 90°, as shown in Figure 45.
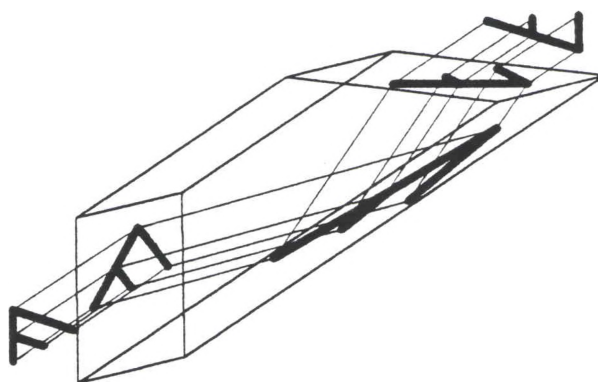
Figure 45. Dove prism configuration used with the galvanometer scanner for rotating the scattered light scan path to coincide with the long dimension of the spectrometer entrance slit.

This places the polarization perpendicular to the slit in the normal setup which gives optimum response of the spectrometer. Normal setup is parallel polarization when studying a single crystal specimen. The incident light polarization is not as much of a concern when studying polycrystalline specimens since scattered light from this material is depolarized. The entrance and exit faces of the dove prism are broad band AR-coated for 45° incidence for s- and p- polarizations. The base is uncoated since minimal losses will occur due to total internal reflection (TIR).

The galvanometer scanner can operate up to 70 Hz with a maximum scan range of 50°. The angular deflection is linear with input voltage, given as 5°/V. The limiting factor in the scan length is the 4.9 mm back (entrance) aperture of the 60x ELWD microscope objective that is currently used to focus the spot onto the specimen.

The size of the laser beam on the scanning element is determined by the optical fiber system used to divert the laser beam around the cylindrical optics and re-direct it onto the scanning element as a laser spot rather than a line. A 20x 0.4 NA objective launches the 0.7 mm diameter beam of 49 mW power and 532 nm wavelength into the polarization-preserving fiber. The fiber NA is 0.1 and defines the angular divergence of light exiting the fiber. A "matched" fiber system was originally used which featured two F-1015 High Precision Steering Lens Fiber Couplers from Newport.[24] These fiber couplers have a long focal length (254 mm) AR-coated negative lens that steers the beam for precision alignment. The 20x microscope objectives have an 8.3 mm focal length and are used with the beam steering lenses for launching and collecting the light in the optical fiber system. The effective focal length of the coupler system using the 20x microscope

objective is 7.4 mm.[24]   Table 12 outlines the spot sizes obtained at both the scanner

element and at the specimen surface using both a 20x and a 40x objective in the output

fiber coupler (assuming Gaussian propagation following the output fiber coupler).   The

light is focused onto the specimen surface using a 3.49 mm 60x ELWD microscope

objective.

Table 12. Spot diameters at the scanner element and at the specimen surface for 20x and 40x objectives in the output fiber coupler of the optical fiber system. The light is focused onto the specimen surface using a 3.49 mm 60x ELWD microscope objective.

objective magnification	NA	f	coupler e.f.l.	scanner element spot diameter	specimen surface spot diameter
20x	0.4	8.3 mm	7.4 mm	1.49 mm	1.59 μm
40x	0.65	4.3 mm	3.78 mm	0.76 mm	3.11 μm

The spot diameter at the scanner element was calculated using

$$s_1 = 2 f_{coupler} \tan \left[\sin^{-1}(NA_{fib}) \right] \qquad (39)$$

where $f_{coupler}$ is the effective focal length of the fiber coupler system. The spot diameter at

the specimen surface is given by

$$s_2 = \frac{4\lambda f_{60x \, ELWD}}{\pi \, s_1} \qquad (40)$$

where $f_{60x \, ELWD}$ is the focal length of the 60x ELWD microscope objective.

The total length of the path traced by the laser spot on the specimen surface is

given by

$$L = 2 f_{60x \, ELWD} \tan(\theta_{max}) \qquad (41)$$

where θ_{max} is the maximum scanner deflection angle of the beam from the center of the

scan path (one-half of the maximum scan range).   Of course, the scanner element

physically rotates by exactly half the scanner deflection angle due to the Law of Reflection.

A study was conducted to compare the operation of the galvanometer scanner system with that of the prior Raman microprobe system. The configurations studied include laser line illumination with the beam splitter and laser spot illumination from the optical fiber with both the beam splitter and the scanner element. The latter two studies involved cases with and without the inclusion of the dove prism. Finally, the scanner operation was studied in scanning mode with the dove prism in place. The performance of these configurations was based on the quality of the resultant Raman spectra. The Raman spectra of a 6H SiC single crystal specimen in the 790 cm^{-1} region for all six configurations are shown in Figure 46. Figure 46(a) shows the Raman spectrum obtained using the beam splitter and laser line focused onto the specimen with the 60x ELWD microscope objective. The spectrum was taken with a three minute exposure time using a 50 μm spectrometer entrance slit width. Next, Figure 46(b) shows the Raman spectrum using the optical fiber system to produce a 2-3 μm spot on the specimen surface. The dove prism was then inserted and aligned to rotate the image of the scattered light by 90°. The Raman spectrum using this configuration is shown in Figure 46(c). Of course, this step should ideally have no effect other than to rotate the polarization by 90°, since the spot is symmetrical, but this configuration was included to determine the decrease in signal due to losses in the dove prism. The Raman spectra using the scanner element were obtained both without and with inclusion of the dove prism, as shown in Figures 46(d) and 46(e), respectively. The exposure time for all the Raman spectra taken with the scanner element

was increased to ten minutes to obtain better signals. The scanner element for this study was simply a glass window. (A determination as to the feasibility of several scanner element designs such as the elliptical mirror "dot," was necessary before an actual design could be implemented and tested.) Assuming 4% reflectance per surface and an incident power on the window of 13 mW (from the fiber), the incident power on the specimen was less than 1 mW. Thus, the 6H SiC single crystal specimen was chosen for its high Raman line strengths compared with polycrystalline SiC specimens so that substantial signals could be observed with relatively weak light incident on the specimen. Based on the data from Table 12, the size of the beam at the glass window is approximately 1.49 mm using the 20x objective in the output fiber coupler. Assuming that the scanning window is located 120 mm from the 60x ELWD objective's back aperture and taking into account the laser beam diameter, the maximum possible angular scan range is then roughly 1.6°. Since the focal length of the 60x ELWD objective is 3.49 mm, the maximum effective scan length on the scan surface is approximately 100 μm. The Raman spectra of Figures 46(d) and 46(e) demonstrate the "channeled spectrum" effect[25] caused by Fabry-Perot interference between the glass window's two surfaces. The Raman lines show this effect but are still distinguishable. Again, the line strengths are slightly lower in Figure 46(e) due to losses in the dove prism. Figure 46(f) was taken while the scanner was operating at 1 Hz frequency using a built-in ramp generator in the scanner driver amplifier. The exposure time was fixed at ten minutes but the entrance slit was increased to 100 μm to detect more of the signal.
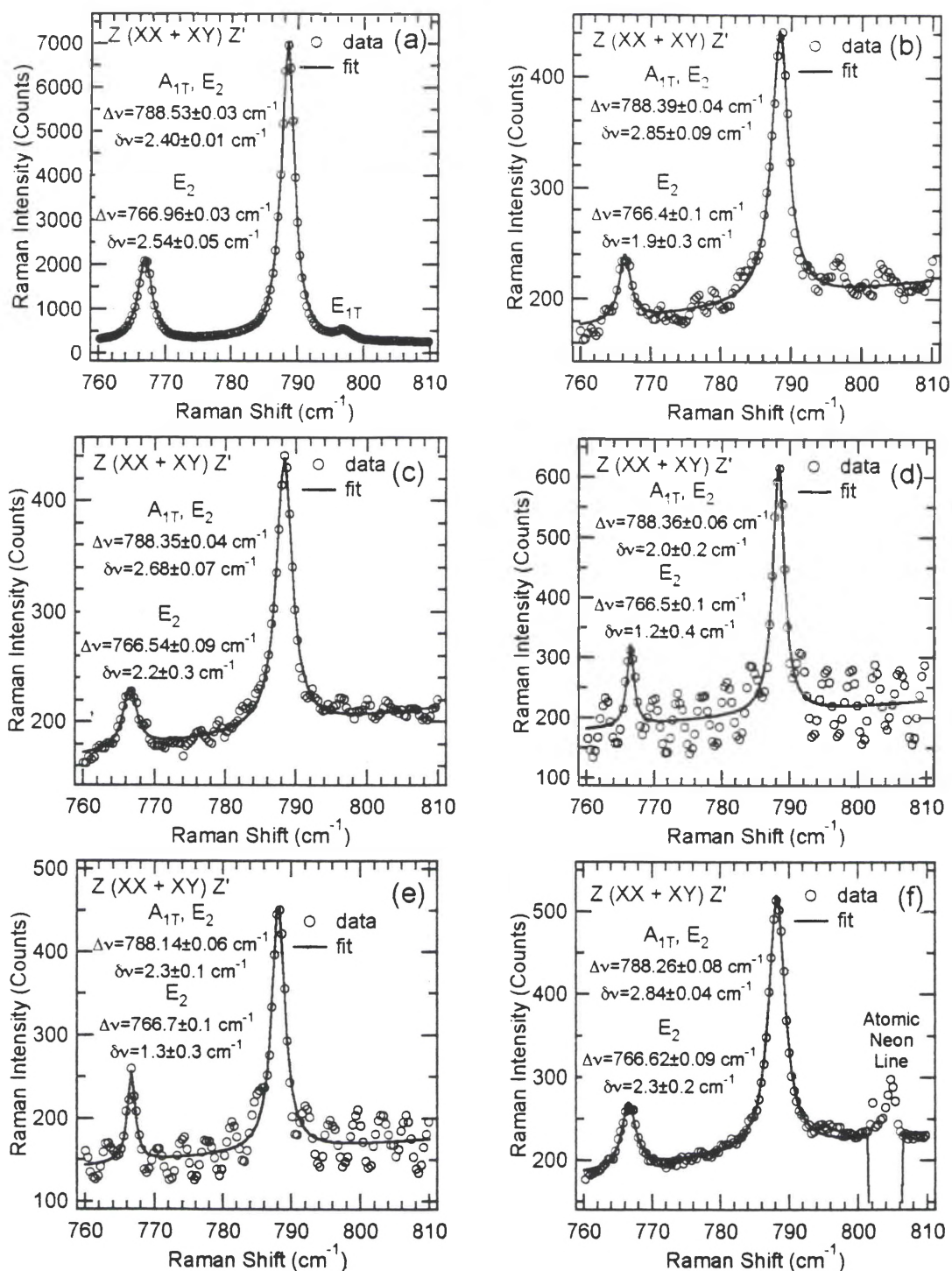
Figure 46. Comparison of Raman spectra from a 6H SiC single crystal specimen using different scanner configurations to determine scanner performance: (a) beam splitter and laser line without dove prism; (b) beam splitter and laser spot without dove prism; (c) beam splitter, laser spot, and dove prism; (d) scanner (stationary) and laser spot without dove prism; (e) scanner (stationary), laser spot, and dove prism; (f) scanner (scanning), laser spot, and dove prism.

The scanning amplitude was set to 0.17 V_{p-p} which equates to a total scanning range of 0.85° (The scanner window was physically rotating within a scanning range of 0.425°). The computed scan length was 51.8 μm and was measured using a micropositioner stage and a binoculars reticle to be about 50 μm. In Figure 46(f) a distinct Raman spectrum was obtained which did not exhibit a channeled spectrum, probably due to an averaging of the signal from the positions illuminated by the scan (similar to obtaining a composite spectrum using the laser line illumination method). Despite the low signals obtained using a simple glass window as the scanner element, this study effectively demonstrated that the galvanometer scanner implementation was a viable upgrade to the Raman microprobe system.

Since the galvanometer scanner will eventually be computer controlled, the following methodology was devised to control the scanning path as a function of time using the computer or data acquisition board's onboard clock. To cover the entire scanning range, it was observed that a low frequency series function such as a ramp (sawtooth), triangle, or sine function was necessary to uniformly scan the range for a number of periods. In addition, it was observed that some sort of "stepping" function would be necessary for correct exposure at each surface position so that enough Raman signal is collected without excessive specimen heating. The long period scanning functions would serve as envelopes for short period "stepping" functions which modulate the envelope functions. The combined function could form a "stairstep" function, for instance, going only up as a ramp function or going up and down as a triangle function.

Assume that $E(t)$ represents the envelope function from which a portion will serve to construct a repeating envelope function $E_r(t)$ with period Δt_e. Likewise, let $M(t)$ represent the modulation function from which a portion will serve to construct a repeating modulation function $M_r(t)$ with period Δt_m. In addition, a logical variable STEP is included to form steps in the total scanning function for a value of "1" and to form no steps for a value of "0." The repeating envelope and modulation functions are given by, respectively,

$$E_r(t) = E\left([t - \Delta\phi_e] - \Delta t_e \text{INT}\left[\frac{t - \Delta\phi_e}{\Delta t_e} + \frac{1}{2} \right] \right) \tag{42}$$

$$M_r(t) = M\left([t - \Delta\phi_m] - \Delta t_m \text{INT}\left[\frac{t - \Delta\phi_m}{\Delta t_m} + \frac{1}{2} \right] \right) \tag{43}$$

where INT(x) returns the highest integer no greater than x. The parameters $\Delta\phi_e$ and $\Delta\phi_m$ are time "phase" factors. Assuming that the scanning function $S(t)$ is simply the envelope function $E_r(t)$ with steps, this function may be described by

$$S(t) = E_r\left(\Delta t_m \text{INT}\left[\frac{t - \Delta\phi_m}{\Delta t_m} + \frac{1}{2} \right] \right) \tag{44}$$

The general scanning function $S(t)$ is then described by

$$S(t) = E_r\left(\text{STEP} \cdot \Delta t_m \text{INT}\left[\frac{t - \Delta\phi_m}{\Delta t_m} + \frac{1}{2} \right] + |\text{STEP} - 1| \cdot t \right) + M_r(t) \tag{45}$$

for a summation of the envelope and modulation functions, with or without steps. The envelope function $E(t)$ might be a triangle function or a ramp function given by

$$E(t) = E_{amp}\left(2\Lambda\left(\frac{2t}{\Delta t_e} \right) - 1 \right) \text{ (triangle)} \tag{46}$$

$$E(t) = E_{amp}\left(\frac{2t}{\Delta t_e} \right) \text{ (ramp)} \tag{47}$$

where both functions have an amplitude E_{amp}, a period Δt_e, and (in this case) a "phase" $\Delta\phi_e$ of zero. The unit triangle function $\Lambda(x)$ is defined as $1 - |x|$ for $|x| \leq 1$. The driving voltage function $V(t)$ for the scanner is given by

$$\tan\left(V(t) \cdot \Phi \right) = \frac{S(t)}{f} \tag{48}$$

where Φ is the angular voltage deflection factor (such as 5°/V), $S(t)$ is the deflection position on the specimen surface, and f is the focal length of the focusing microscope objective.

CHAPTER VII

DISCUSSION AND CONCLUSIONS

Studies of the Relative Residual Surface Stresses in 6H SiC

The main goal of this thesis was to study the correlation between the Raman spectra of 6H SiC subjected to different machining procedures. The effort was aimed at determining how the measured spectral parameters relate to the flexural strength of the material and the machining processes in order to identify the machined surfaces which produce the least amount of damage and the highest strength characteristics. These relative residual surface stresses were measured using laser Raman microprobe spectroscopy. The use of a Nd:YAG 532 nm laser or an Ar ion laser coupled with the ability to focus an elliptical laser line with cylindrical optics or a laser spot via a fiber optic system onto the specimen surface and collect the scattered Raman signal with either the PMT or CCD array detection systems gave the Raman microprobe system a wide range of flexibility. Using weighted statistical averaging of the measured Raman shifts and linewidths of the Raman modes in the 790 cm^{-1} region for the 6H SiC specimens, the relative residual surface stresses were ascertained for each type of machining process. When these data were compared with flexural strength data for baseline, creep feed, and ultrasonic grind specimens, a strong correlation was found for the baseline specimens. The Raman shift/flexural strength correlation was found to be -6±1 cm^{-1}/GPa and the

Raman linewidth/flexural strength correlation was found to be -20±4 cm^{-1}/GPa. This study revealed that creep feed grinding produced less residual surface stress than baseline grinding. However, when baseline specimens were heat treated or oxidized, these processes greatly reduced the relative residual surface stresses, increasing the flexural strength significantly. The oxidation process did not reduce the residual surface stress to the degree observed with just heat treatment. The ultrasonic grind process produced the largest residual surface stress. It is believed that this is due to the up-and-down pounding of abrasive particles in the slurry against the specimen surface during grinding. The Raman linewidth for this process was lower than anticipated because the grinding process is fairly uniform across the surface, such that there is very little variation in the relative residual stress across the surface. Overall, creep feed grinding was appealing because it produced very little residual surface stress compared with conventional grinding. However, other final processes such as heat treatment or oxidation reduced the residual stresses found in baseline specimens and thus increased their material strength. The results of this study suggest that these processes could be performed on creep feed grind specimens for further reductions in residual surface stress and increased material strength.

Other Studies of 6H SiC

Other studies in this thesis included: examining single crystal specimens in a polarization study of their Raman spectra; performing laser penetration depth studies of creep feed and baseline grind specimens using different wavelengths; obtaining "reference" Raman data from the unprocessed ends of polycrystalline specimens and comparing the

results with those of as-sintered specimens; performing a "survey" study of polycrystalline specimens by varying the incident laser polarization, the type of processed specimen, and the probe location on the same specimen; analyzing the presence of 4H SiC polytype in specimens; observing the occurrence of fluorescence in specimens; and finally observing the preliminary operation of the galvanometer scanner upgrade to the Raman microprobe system. The single crystal studies revealed the appearance of the 790 cm^{-1} region Raman modes characteristic of 6H SiC for different polarization configurations. These studies confirmed the appearance of the 767 cm^{-1} (E$_2$), 788 cm^{-1} (A$_{1T}$/E$_2$), and 797 cm^{-1} (E$_{1T}$) modes for typical Raman spectra from 6H SiC specimens at normal experimental conditions. The laser penetration depth studies were useful in obtaining the relative damage profile of the creep feed and baseline specimens using the 488 nm Ar ion laser wavelength in addition to the 532 nm Nd:YAG wavelength. Although preliminary, this study demonstrated how the relative residual stress could be obtained as a function of wavelength, revealing how the relative damage changes with depth. This study confirmed the experimental data which showed that creep feed grinding produces less residual surface stress than baseline grinding and that, as expected, the residual stress was higher for both machining methods closer to the surface using the 488 nm incident laser light. Although varied, the Raman data from the unprocessed ends of polycrystalline specimens demonstrated that the residual stresses were less than those of machined surfaces even though the data was skewed slightly due to flaws and defects when compared with the data obtained from an as-sintered specimen. The "survey" study of polycrystalline specimens using different experimental conditions such as polarization, specimen type, and

different illumination locations on the same specimen simply confirmed the observations of later research but served as a guide for further investigation. Although it was not realized at the time of the study, the occasional appearance of the 777 cm^{-1} and the 783 cm^{-1} Raman lines signified the presence of 4H SiC polytype. These Raman lines are designated as the E_2 and A_{1T} modes, respectively. This study became much more significant once the identification of these Raman lines became clear and indicates a direction for further study of polytypes in SiC. The studies of fluorescence in SiC is another direction for further research. Several sites were investigated by performing long range spectral surveys, but no definitive conclusions could be made about the origin of this effect other than, as suggested by the data, the presence of a rare earth or transition element (these elements have long been known to exhibit fluorescence behavior).

Recommendations For the Prototype Galvanometer Scanner

The incorporation and preliminary operation of a galvanometer scanner within the Raman microprobe system was one of the final studies performed during this research. With the use of a simple glass window as a scanner element, Raman spectra were successfully observed from a 6H SiC single crystal specimen, although a channeled spectrum was noticed in the background due to Fabry-Perot interference between the two glass window surfaces. This effect could be eliminated if the surfaces are AR-coated. For scanning operation, a dove prism was necessary to rotate the scattered light such that the image of the linear scan path is aligned with the length of the entrance slit to the double spectrometer. The channeled spectrum was not observed in scan mode due to statistical

averaging of the collected signal from the entire region along the scan path. This study revealed that Raman spectra would be successfully obtained using the scanner system if appropriate considerations are made for the design of the scanner element, namely to maximize the power reaching the specimen surface without undue specimen heating and to maximize the collected Raman signal. Further study of the scanner system will be necessary to fully realize its potential within the Raman microprobe system. At peak performance, the scanner system will provide uniform illumination of the specimen surface in one dimension and eliminate the problem inherent in the Gaussian illumination profile along the length of the elliptical line produced by the cylindrical optics system. In addition, the illumination coverage will be increased and the position of the scanning spot along one direction will be fully computer controlled. The addition of an actuator-driven micrometer stage that is computer-controlled and operates transverse to the scan path would allow two-dimensional spectral mappings of regions on a specimen surface, thus widening the possibilities for image processing applications. The use of a pulsed laser or a beam chopper could further aid the scanner operation by controlling specimen heating, reducing unwanted fluorescence effects, and accurately maintaining illumination at specific localized regions along the scan path. Overall, the galvanometer scanner system will vastly improve characterization of materials by merging Raman spectroscopy with image processing capabilities.

REFERENCES

1. R. S. Krishnan, "Historical Introduction," in <u>The Raman Effect</u>, Vol. 1: Principles, edited by A. Anderson (Marcel Dekkar, Inc., New York, 1971), pp. 2-5, 28-29.

2. Wilfried König and Jens Wemhöner, "Optimizing Grinding of SiSiC," Amer. Ceram. Soc. Bull. 68 (3), 545-548 (1989).

3. Evangelos Anastassakis, "Inelastic Light Scattering in the Presence of Uniaxial Stresses," J. Raman Spectrosc. 10, 64-76 (1981).

4. J. D. Jackson, <u>Classical Electrodynamics</u>, 2nd ed. (John Wiley & Sons, New York, 1975), pp. 394-397.

5. M. Tobin, <u>Laser Raman Spectroscopy</u> (Wiley-Interscience, New York, 1971), pp. 5-7.

6. P. M. A. Sherwood, <u>Vibrational Spectroscopy of Solids</u> (Cambridge University Press, New York, 1972), pp. 14-25, 42, 50, 171.

7. Robert Eisberg and Robert Resnick, <u>Quantum Physics of Atoms, Molecules, Solids, Nuclei, and Particles</u>, 2nd Ed. (John Wiley & Sons, New York, 1985), pp. Q 1-7.

8. Ralph W. G. Wyckoff, <u>Crystal Structures</u>, 2nd Ed. (Interscience Publishers, New York, 1965), Vol. 1, pp. 109-120.

9. D. W. Feldman, J. H. Parker, Jr., W. J. Choyke, and L. Patrick, "Raman Scattering in 6H SiC," Phys. Rev. 170 (3), 698-704 (15 June 1968).

10. Charles Kittel, <u>Introduction to Solid State Physics</u>, 4th Ed. (John Wiley & Sons, Inc., New York, 1971), p. 129.

11. <u>Hamamatsu Photomultiplier Tubes</u>, (Hamamatsu Corporation).

12. J. Blackshire and P. Yaney, Bull. Am. Phys. Soc. (1991), J. Blackshire, M.S. Thesis in Electro-Optics, University of Dayton, (December 1991).

13. S. Ernst and P. Yaney, Bull. Am. Phys. Soc. (1992), S. L. Ernst, M.S. Thesis in Electro-Optics, University of Dayton, (August 1992).

14. American Institute of Physics Handbook, 2nd Ed. G. H. Dieke, At. and Mol. Phys. Sec. Editor. Dwight E. Gray, Coor. Editor. (McGraw-Hill Book Co., Inc., New York, 1963), pp. 7-43 to 7-125.

15. T. C. Damen, S. P. S. Porto, and B. Tell, Phys. Rev. 142, 570 (1966).

16. "Standard Test Method for Flexural Strength of Advanced Ceramics at Ambient Temperature," ASTM Designation C 1161-90 (1990), pp. 1-7.

17. D. P. Stinton, "Assessment of the State of the Art in Machining and Surface Preparation of Ceramics," ORNL/TM-10791 (Martin Marietta, 1988) pp. 1-36.

18. Thomas Hollstein and Wulf Pfeiffer, "The Strength and Fracture Behaviour of Engineering Ceramics--Influence of Machining and Residual Stresses," Int. Symp. Ceram. Mater. Compon. Engines, 4th (1992) Meeting Date 1991, Editors: Roger Carlsson, Thomas Johansson, and Lars Kahlman. Publisher: Elsevier, London, UK. pp. 821-829.

19. David W. Richerson, Modern Ceramic Engineering: Properties, Processing, and Use in Design, 2nd Ed. (Marcel Dekker, Inc., New York, 1992), pp. 180-181, 602-603.

20. N. L. Hecht, "Environmental Effects in Toughened Ceramics," Ceramic Technology Project Semiannual Report to Martin-Marietta Energy Systems, Inc. (University of Dayton Research Institute, Report No. UDR-TR-96-55, October 1995-March 1996).

21. K. Jennings, "Studies of Grain Phase and Orientation in Advanced Silicon Carbide Ceramics Using a Laser Raman Microprobe," M.S. Thesis in Electro-Optics, University of Dayton, (1989).

22. Shin-ichi Nakashima, Atsuo Wada, and Zenzaburo Inoue, "Raman Scattering From Anisotropic Phonon Modes in SiC Polytypes," J. Phys. Soc. Jpn. 56 (9), 3375-3380 (September 1987).

23. Wulf Pfeiffer, "Characterization of Near-Surface Conditions of Machined Ceramics by Use of X-ray Residual Stress Measurements," Residual Stresses III, Elsevier Science Publ. Ltd., London, New York, Vol. 2 (1992), pp. 607-612.

24. "1993 Newport Catalog," (Newport Corp., CA, 1993).

25. John Strong, <u>Concepts of Classical Optics</u> (W. H. Freeman & Co., San Francisco, 1958), pp. 232-235.

26. Y.-R. Shen, in <u>Topics in Applied Physics</u>, edited by M. Cardona (Springer-Verlag, New York, 1975), Vol. 8, Chap. 7, p. 275.

27. W. Hayes and R. Loudon, <u>Scattering of Light by Crystals</u> (John Wiley & Sons, Inc., New York, 1978), p. 46.

28. Philip R. Bevington, <u>Data Reduction and Error Analysis For the Physical Sciences</u> (McGraw Hill Book Company, New York, 1969), pp. 66-80.

APPENDIX A

Calculations of the Absolute Power of Raman Scattering for
6H SiC Used in the Raman Microprobe Setup

From classical light scattering theory, the ratio of scattered power P_s to incident power P_i can be expressed as

$$\frac{P_s}{P_i} = N \cdot \sigma_\Omega \cdot \Omega \cdot L \tag{49}$$

where N is the number density of scattering sites (expressed in cm^{-3}), σ_Ω is the differential cross section of the scattering medium (expressed in cm^2/sr for a 1 m^3 scattering volume), Ω is the solid angle describing the cone of scattered light (expressed in sr), and L is the length of the scattering volume (expressed in cm) which, for a 180° backscattering geometry, runs parallel to the incident light propagation direction. The differential cross section σ_Ω has been integrated over the entire spectrum so that only the solid angle Ω is needed to determine the cross section. Some sources quote the differential cross section as the differential cross section per unit volume of the scattering site (expressed in units of cm^{-1} sr^{-1}). This quantity is simply the product of the differential cross section and the number density of the scattering sites. For InSb, a material similar in cross section to that of SiC, this quantity has a value of roughly 10^{-7} cm^{-1} sr^{-1}.[26] The solid angle Ω for a collecting microscope objective of known numerical aperture (NA) is given by

$$\Omega = 2\pi\left(1 - \sqrt{1 - (\text{NA})^2}\right) \tag{50}$$

107

Since the 3.49 mm 60x ELWD microscope objective has a 0.7 NA, the solid angle Ω is about 1.80 sr. Since the penetration depth using 532 nm light was approximately 1 μm, the length L of the scattering volume is assumed to be 1 μm. Inserting these quantities into Equation (49) gives a value of about 2×10^{-11}. Thus, based on these calculations, scattered power of the Raman signal is roughly eleven orders of magnitude smaller than the incident power.

Another way to "check" this calculation is to use experimental values gathered from the actual system. The incident power at the specimen surface using an elliptical line of 532 nm laser illumination is approximately 7.1 mW. The measured signal strength of the 788 cm^{-1} Raman line using the PMT detection system was typically 600 counts for a ten second exposure. Losses in the system must be estimated in order to adequately determine the total power of the Raman signal scattered directly from the surface. A "loss" inventory is shown in Table 13. (Refer to the experimental setup in Figure 15.)

Table 13. System "loss" inventory for determining the absolute power of Raman scattering for the 788 cm^{-1} line of 6H SiC.

System Element(s)	Transmittance
% solid angle of scattered light collected	0.14
microscope objective	0.8
1 beam splitter	0.7
13 mirrors	$(0.92)^{13}$
3 lenses (6 surfaces)	$(0.98)^{6}$
3 gratings	$(0.6)^{3}$
PMT efficiency	0.2
Combined System	0.0010

The detected photon rate was 60 photons/s for the 788 cm^{-1} Raman line. Dividing this rate by the system transmittance gives a scattering photon rate of about 59,000 photons/s. Since the corresponding wavelength of the 788 cm^{-1} Raman signal is 555.39 nm, the energy per photon E can be found using

$$E = \frac{hc}{\lambda} \tag{51}$$

where h is Planck's constant and c is the speed of light. At this wavelength, the energy per photon is approximately 2.24 eV. Multiplying this energy by the scattering photon rate gives a scattered power of 2.1 x 10^{-14} W. An estimate of the scattered power to incident power ratio is then about 3 x 10^{-12}. The result compares favorably with the "derived" result of 2 x 10^{-11}, being different by less than one order of magnitude.

APPENDIX B

Igor Pro 2.0 Software Macros Written to Analyze Raman Spectral Data

Macro/Function Hierarchy:

I.   Functions

    A.   U (step)

    B.   RMP (ramp) - U

    C.   RECT (rect) - U

    D.   TRI (unit triangle) - RMP - U

    E.   TRIN (general triangle) - TRI - RMP - U

    F.   TRIANGLE (alternate general triangle)

    G.   LR (unit Lorentzian)

    H.   LRN (general Lorentzian)

    I.   LORENTZIAN (one line with background) - LRN - LR

    J.   DBLPEAKS (two lines with background) - LRN - LR

    K.   ONETILT (one line with tilted background) - LRN - LR

    L.   DBLTILT (two lines with tilted background) - LRN - LR

    M.   TRIPLETILT (three lines with tilted background) - LRN - LR

    N.   QUADRATILT (four lines with tilted background) - LRN - LR

    O.   QUINTATILT (five lines with tilted background) - LRN - LR

II.   Raman Fitting, Statistics, and Graphing Procedures

    A.   Menu

    B.   Raman Fitting Procedures

        1.   Initial - Reference - GetWave

        2.   Reference - GetWave

        3.   Raman

            a.   TRIANGLE

            b.   ButtonProc

        4.   Raman2 - (ONETILT or DBLTILT or TRIPLETILT or QUADRATILT or QUINTATILT)

    C.   Raman Statistics - Stat

        1.   Statname

        2.   GetRam - GetWave

    D.   Raman Graphing Procedures

        1.   RamGraph

            a.   GetRam - GetWave

            b.   Prmpt

        2.   RamGrapha

            a.   Prmpt

            b.   GraphWin

        3.   RamGraph2

III.   Atomic Line Fitting and Statistics Procedures

    A.   Menu

    B.   Atomic Line Fitting Procedures

        1.   InitAtom - AtomGraph - GetWave

        2.   AtomGraph - GetWave

        3.   RepeatAtom - TRIANGLE

    C.   Atomic Line Statistics - AtomStat

        1.   Atomstatname

        2.   GetRam - GetWave

Macro/Function Listings:

```
|Raman Fit Functions

FUNCTION U(X)
| STEP FUNCTION
     VARIABLE X

     RETURN((SIGN(X)+1)/2)
END

FUNCTION RMP(X)
| RAMP FUNCTION
     VARIABLE X

     RETURN(X*U(X))
END

FUNCTION RECT(X)
| RECTANGLE FUNCTION
     VARIABLE X

     RETURN(U(X+1/2)*U(-X+1/2))
END
```

```
FUNCTION TRI(X)
| TRIANGLE FUNCTION
     VARIABLE X

     RETURN(RMP(X+1)-2*RMP(X)+RMP(X-1))
END

FUNCTION TRIN(A,B,C,X)
| GENERAL TRIANGLE FUNCTION
     VARIABLE A,B,C,X |AMPLITUDE,WIDTH,CENTER POSITION,POSITION

     RETURN(A*TRI((X-C)/B))
END


| TRIANGLE FIT FOR ATOMIC SPECTRA
| EQUATION:   TRIANGLE = h - m*|X-Xo|
| WAVE W CONTAINS THE COEFFICIENTS TO TRIANGLE.  A DESCRIPTION OF THE
| COEFFICIENTS IS AS FOLLOWS . . .
| W[0] = h,  W[1] = m,  W[2] = Xo

FUNCTION TRIANGLE (W,X)
     WAVE W; VARIABLE X

     RETURN(W[0]-W[1]*ABS(X-W[2]))
END


FUNCTION LR(X)
| LORENTZIAN FUNCTION
     VARIABLE X

     RETURN(1/(1+X^2))
END

FUNCTION LRN(A,B,C,X)
| GENERAL LORENTZIAN FUNCTION
     VARIABLE A,B,C,X | AMPLITUDE,WIDTH,CENTER POSITION,POSITION

     RETURN(A*LR((X-C)*2/B))
END


| 1 PEAK LORENTZIAN DISTRIBUTION
| LORENTZIAN:  LR=1/(1+X^2)
| GENERAL LORENTZIAN:  LRN=A*LR((X-V)*2/DV)
| EQUATION:  L1 = LRN(A1,DV1,V1,X)
|            LORENTZIAN = L1 + C
| WAVE W CONTAINS THE COEFFICIENTS TO LORENTZIAN.  A DESCRIPTION OF THE
| COEFFICIENTS IS AS FOLLOWS . . .
| W[0] = A1,  W[1] = DV1,  W[2] = V1,  W[3] = C
```

```
FUNCTION LORENTZIAN(W,X)
     WAVE W; VARIABLE X


     RETURN(LRN(W[0],W[1],W[2],X)+W[3])
END


| 2 PEAK LORENTZIAN DISTRIBUTION
| LORENTZIAN:  LR=1/(1+X^2)
| GENERAL LORENTZIAN:  LRN=A*LR((X-V)*2/DV)
| EQUATION:  L1 = LRN(A1,DV1,V1,X)
|            L2 = LRN(A2,DV2,V2,X)
|            DBLPEAKS = L1 + L2 + C
| WAVE W CONTAINS THE COEFFICIENTS TO DBLPEAKS.  A DESCRIPTION OF THE
| COEFFICIENTS IS AS FOLLOWS . . .
| W[0] = A1, W[1] = DV1,  W[2] = V1, W[3] = A2, W[4] = DV2, W[5] = V2,
| W[6] = C


FUNCTION DBLPEAKS(W,X)
     WAVE W; VARIABLE X


     RETURN(LRN(W[0],W[1],W[2],X)+LRN(W[3],W[4],W[5],X)+W[6])
END


| 1 PEAK LORENTZIAN DISTRIBUTION WITH TILTED BACKGROUND
| LORENTZIAN:  LR=1/(1+X^2)
| GENERAL LORENTZIAN:  LRN=A*LR((X-V)*2/DV)
| EQUATION: 1TILT =LRN(A1,DV1,V1,X) + M*(X-V1) + B
| WAVE W CONTAINS THE COEFFICIENTS TO 1TILT.  A DESCRIPTION OF THE
| COEFFICIENTS IS A FOLLOWS . . .
| W[0] = A1, W[1] = DV1, W[2] = V1, W[3] = M, W[4] = B


FUNCTION ONETILT(W,X)
     WAVE W; VARIABLE X


     RETURN(LRN(W[0],W[1],W[2],X)+W[3]*(X-W[2])+W[4])
END


| 2 PEAK LORENTZIAN DISTRIBUTION WITH TILTED BACKGROUND
| LORENTZIAN:  LR=1/(1+X^2)
| GENERAL LORENTZIAN:  LRN=A*LR((X-V)*2/DV)
| EQUATION:  L1 = LRN(A1,DV1,V1,X)
|            L2 = LRN(A2,DV2,V2,X)
|            DBLTILT = L1 + L2 + M*(X-V1) + B
| WAVE W CONTAINS THE COEFFICIENTS TO DBLPEAKS.  A DESCRIPTION OF THE
| COEFFICIENTS IS AS FOLLOWS . . .
| W[0] = A1, W[1] = DV1,  W[2] = V1, W[3] = A2, W[4] = DV2, W[5] = V2,
| W[6] = M, W[7] = B
```

```
FUNCTION DBLTILT(W,X)
      WAVE W; VARIABLE X

      RETURN(LRN(W[0],W[1],W[2],X)+LRN(W[3],W[4],W[5],X)+
          W[6]*(X-W[2])+W[7])
END


|  3 PEAK LORENTZIAN DISTRIBUTION WITH TILTED BACKGROUND
|  LORENTZIAN:  LR=1/(1+X^2)
|  GENERAL LORENTZIAN:  LRN=A*LR((X-V)*2/DV)
|  EQUATION:  L1 = LRN(A1,DV1,V1,X)
|             L2 = LRN(A2,DV2,V2,X)
|             L3 = LRN(A3,DV3,V3,X)
|             TRIPLETILT = L1 + L2 + L3 + M*(X-V1) + B
|  WAVE W CONTAINS THE COEFFICIENTS TO DBLPEAKS.  A DESCRIPTION OF THE
|  COEFFICIENTS IS AS FOLLOWS . . .
|  W[0] = A1, W[1] = DV1,  W[2] = V1, W[3] = A2, W[4] = DV2, W[5] = V2
|  W[6] = A3, W[7] = DV3, W[8] = V3, W[9] = M, W[10] = B

FUNCTION TRIPLETILT(W,X)
      WAVE W; VARIABLE X

      RETURN(LRN(W[0],W[1],W[2],X)+LRN(W[3],W[4],W[5],X)+
          LRN(W[6],W[7],W[8],X)+W[9]*(X-W[2])+W[10])
END


|  4 PEAK LORENTZIAN DISTRIBUTION WITH TILTED BACKGROUND
|  LORENTZIAN:  LR=1/(1+X^2)
|  GENERAL LORENTZIAN:  LRN=A*LR((X-V)*2/DV)
|  EQUATION:  L1 = LRN(A1,DV1,V1,X)
|             L2 = LRN(A2,DV2,V2,X)
|             L3 = LRN(A3,DV3,V3,X)
|             L4 = LRN(A4,DV4,V4,X)
|             QUADRATILT = L1 + L2 + L3 + L4 + M*(X-V1) + B
|  WAVE W CONTAINS THE COEFFICIENTS TO DBLPEAKS.  A DESCRIPTION OF THE
|  COEFFICIENTS IS AS FOLLOWS . . .
|  W[0] = A1, W[1] = DV1,  W[2] = V1, W[3] = A2, W[4] = DV2, W[5] = V2
|  W[6] = A3, W[7] = DV3, W[8] = V3, W[9]=A4, W[10]=DV4, W[11] = V4
|  W[12] = M, W[13] = B

FUNCTION QUADRATILT(W,X)
      WAVE W; VARIABLE X

      RETURN(LRN(W[0],W[1],W[2],X)+LRN(W[3],W[4],W[5],X)+
          LRN(W[6],W[7],W[8],X)+LRN(W[9],W[10],W[11],X)+
          W[12]*(X-W[2])+W[13])
END
```

```
| 5 PEAK LORENTZIAN DISTRIBUTION WITH TILTED BACKGROUND
| LORENTZIAN:   LR=1/(1+X^2)
| GENERAL LORENTZIAN:   LRN=A*LR((X-V)*2/DV)
| EQUATION:   L1 = LRN(A1,DV1,V1,X)
|             L2 = LRN(A2,DV2,V2,X)
|             L3 = LRN(A3,DV3,V3,X)
|             L4 = LRN(A4,DV4,V4,X)
|             L5 = LRN(A5,DV5,V5,X)
|             QUINTATILT = L1 + L2 + L3 + L4 + L5 + M*(X-V1) + B
| WAVE W CONTAINS THE COEFFICIENTS TO DBLPEAKS.  A DESCRIPTION OF THE
| COEFFICIENTS IS AS FOLLOWS . . .
| W[0] = A1, W[1] = DV1,  W[2] = V1, W[3] = A2, W[4] = DV2, W[5] = V2
| W[6] = A3, W[7] = DV3, W[8] = V3, W[9]=A4, W[10]=DV4, W[11] = V4
| W[12] = A5, W[13] = DV5, W[14] = V5, W[15] = M, W[16] = B


FUNCTION QUINTATILT(W,X)
      WAVE W; VARIABLE X

      RETURN(LRN(W[0],W[1],W[2],X)+LRN(W[3],W[4],W[5],X)+
            LRN(W[6],W[7],W[8],X)+LRN(W[9],W[10],W[11],X)+
            LRN(W[12],W[13],W[14],X)+W[15]*(X-W[2])+W[16])
END



|Raman Menu

Menu "Macros"
      "Initial/0"
      "Reference/1"
      "Raman/2"
      "Raman2/3"
      "Stat/4"
      "RamGraph/5"
      "RamGrapha/6"
      "RamGraph2/7"

End

|Raman Fit Procedures

Function Initial()
|THIS FUNCTION IS USED AT THE START OF AN EXPERIMENT TO BEGIN CURVE
|FITTING OF A SERIES OF RUNS.  IT PROVIDES INITIAL PARAMETERS SUCH AS
|INCIDENT WAVELENGTH AND WAVELENGTH DISPERSION TO BE USED THROUGHOUT THE
|CURVE FITTING PROCEDURE.  THE DEFAULT PARAMETERS MAY BE CHANGED SIMPLY
|BY EDITING THE PROCEDURE.  (ONE MAY WISH TO PLACE A COPY OF THESE
|FUNCTIONS AND MACROS INTO THE PROCEDURE FILE OF THE EXPERIMENT SO AS
|NOT TO ALTER THE ORIGINAL PROCEDURE FILES.)  IT AUTOMATICALLY CALLS THE
|"REFERENCE" FUNCTION AT THE END OF THE FIRST RUN.  THEREFORE, THE CURVE
|FITTING FUNCTION SEQUENCE THAT THE USER MUST FOLLOW IS:
|RUN 1:   INITIAL, RAMAN, RAMAN2
|RUN 2:   REFERENCE, RAMAN, RAMAN2
```

```
|RUN 3:   REFERENCE, RAMAN, RAMAN2
|AND SO ON UNTIL CURVE FITTING OF THE SERIES OF RUNS IS COMPLETE.
      datafile suffix, prefix, path, and extension
      string/g suf1="A",pref1="T010195",
          pat1="Data:Joe Binford:DATAstor3:",ext1="prn"
|     sample triangle fit parameters of atomic spectral line in pixel
|     scale (pixel=23 micron) (amplitude from 0,slope,position)
|     string/g peak1="coeff={839,325.5,350.5}"
|     sample Raman parameters for 1-5 peaks in wavenumber scale
|     including background slope and amplitude. Each peak has parameters
|     of amplitude (from background), spectral FWHM width, and spectral
|     position. The peak1a and peak2 include 788 and then 767 lines
|     since these are the most common for 6H SiC single crystal (phonon
|     propagation parallel to c-axis).
      string/g peak1a="coeff={244.4,4.6,788,0.13,191}"
      string/g peak2="coeff={51.2,5.2,767,244.4,4.6,788,0.13,191}"
|     The peaks 3-5 were primarily used for 6H SiC ceramic specimens
|     since 3-5 peaks were almost always observed.  The most common were
|     the 767,788, and 797, then the 777 line, and finally the 783 line
|     was the most infrequent.
      string/g peak3="coeff={51.2,5.2,767,244.4,4.6,788,74.9,6.4,797,
                  0.13,191}"
      string/g peak4="coeff={51.2,5.2,767,244.4,4.6,788,74.9,6.4,797,
                  12.6,3.4,777,0.13,191}"
      string/g peak5="coeff={51.2,5.2,767,244.4,4.6,788,74.9,6.4,797,
                  12.6,3.4,777,60,5.1,783,0.13,191}"
|     known parameters: these parameters, whose values and uncertainties
|     were stored in the waves c and ce respectively, were the 532 nm
|     DPSS Nd:YAG laser wavelength in angstroms, the Ne reference line
|     wavelength in angstroms used for calibration in the 780 1/cm
|     region, the position in which the wavenumber difference between
|     the two lines will be stored (see below), the wavelength
|     dispersion (angstroms/pixel), and the wavenumber dispersion
|     (1/cm/pixel) (this last parameter is not used in computations).
      make/d/o/n=5 c={5321.0379,5562.76620,0,.113079,.365857}
      make/d/o/n=5 ce={0.0026,0.00005,0,0.000022,0.000070}
|     The following two lines are for use when using the Ar ion 488 nm
|     laser line
      make/d/o/n=5 c={4879.85016,5080.38520,0,.1136121,.365857}
      make/d/o/n=5 ce={0.00514,0.00005,0,0.0000332,0.000070}
|     computation of wavenumber difference in laser line and neon atomic
|     reference line and error
      c[2]=1e8*(1/c[0]-1/c[1])
      ce[2]=1e8*sqrt((ce[0]/c[0]^2)^2+(ce[1]/c[1]^2)^2)
|     start the Reference function for loading and fitting the neon
|     atomic reference line for calibration.  Once the cycle for fitting
|     the first data file (a) is complete, the execution of this
|     "Initial()" function is no longer necessary since the constant
|     parameters are stored in memory. The cycles for following
|     datafiles can begin with the "Reference()" function.
      Execute "Reference()"
End
```

```
function Reference()
     |     THIS FUNCTION LOADS A DATA RUN AND PREPARES THE GRAPH FOR FITTING
     |     AN ATOMIC REFERENCE LINE (FIT IS PERFORMED ON PIXEL SCALE)
     |     define strings for storing the wave names of the count data y, the
     |     best fit data b of the Raman lines, the triangle fit t of the
     |     atomic line, and the graph name gra of the resulting graph
           string/g y,b,t,gra,pat1,pref1,suf1,ext1,peak1
     |     tell Igor that wav0 is a wave (wav0 is the horizontal pixel scale
     |     used for all runs)
           wave wav0=wav0
     |     obtain prefix, suffix, path, and extension of wave
           execute "GetWave()"
     |     load Raman run (update the current path of the datafile)
           newpath/q/o np, pat1
     |     load the wave with current prefix, suffix, and extension with
     |     wavename wav1
           loadwave/g/d/q/n=wav/p=np pref1+suf1+"."+ext1
     |     reassigns wavename wav1 with wavename "y"+suffix ($ sign indicates
     |     wave with name of the following string)
           y="y"+suf1
           rename wav1,$y
     |     display reference graph
           b="b"+suf1;t="t"+suf1
           make/d/n=578 $b,$t
     |     building window...
           execute "display /w=(5,42,400,250) $y,$b,$t vs wav0"
           gra="g"+pref1+suf1
     |     make graph window with name of gra
           dowindow/c $gra
     |     make data have circle markers and fits be lines
           execute "ModifyGraph mode($y)=3"
           execute "ModifyGraph marker($y)=8"
           execute "ModifyGraph rgb($b)=(0,65000,0),rgb($t)=(0,0,65000)"
           SetAxis/a
     |     set cursors at approximate location of atomic reference line
           Cursor A $y 348;Cursor B $y 351
     |     show cursor information (coordinates)
           ShowInfo
     |     reset fitting parameters used for both atomic and Raman lines for
     |     atomic line fit
           make/d/o/n=3 coeff=0,W_sigma=0
     |     prints the STATEMENT to assign the current parameters of the coeff
     |     wave to itself.  The purpose of this is to allow the user to
     |     change the current parameters at the command line to update
     |     necessary changes in "guesses" for fitting parameters.  The user
     |     clicks on the printed STATEMENT in the history while holding down
     |     the command key to bring the STATEMENT to the command line.  Then
     |     the user edits the parameters as necessary and presses RETURN to
     |     accept the new "guesses" for the fitting parameters of the atomic
     |     line fit.
           print peak1
end
```

```
Macro GetWave(suf,pref,pat,ext)
      string suf=suf1,pref=pref1,pat=pat1,ext=ext1
      prompt suf, "Enter suffix letter of wave"
      prompt pref, "Enter prefix of wave to load"
      prompt pat, "Enter path of wave to load"
      prompt ext, "Enter extension of wave to load"
|     THIS MACRO OBTAINS A WAVE.  THE USER DEFINES THE SUFFIX, PREFIX,
|     PATH AND EXTENSION.
|     Obtain suffix, prefix, path and extension of wave.  Current
|     information which doesn't need to be changed will remain the
|     default and doesn't need to be re-entered (such as prefix,path,
|     or extension).  Assign global string values to local macro string
|     values of datafile designation.  Update global string values using
|     new local macro string values.
      suf1=suf
      pref1=pref
      pat1=pat
      ext1=ext
endmacro


function Raman()
|     THIS FUNCTION FITS THE ATOMIC REFERENCE LINE ACCORDING TO THE
|     FITTING PARAMETERS GIVEN, SCALES THE HORIZONTAL AXIS TO
|     WAVENUMBERS, AND PREPARES THE GRAPH FOR FITTING THE RAMAN LINES
|     Add ram wave to store final fitting parameters of wave.
|     ram wave consists of 40 elements for storing data from up to five
|     Raman lines.
|     (3 values/Raman line)*5 (max Raman lines) + background slope +
|           background amplitude + 3 values for atomic line fit =
|     20 elements--the final 20 elements are the uncertainties in each
|     of these parameters.  Note that unused elements are designated
|     with a 0.
|     wavnum wave is the horizontal wavenumber scaling computed from the
|     atomic line fit.  Since the fit can vary from run to run, there
|     are the same number of wavnum waves as there are fits and are
|     designated with the appropriate datafile suffix.
      string/g y,b,t,gra,ram,wavnum,peak1,pref1,suf1
|     V_npnts and V_chisq store the total number of points and the chi
|     square distribution for the atomic line fit.
      variable/d/g V_npnts,V_chisq
      wave c=c,ce=ce,wav0=wav0,coeff=coeff,W_sigma=W_sigma
|     Perform triangle fit to reference
      execute"FuncFit/q TRIANGLE coeff $y(xcsr(A),xcsr(B))  /X=wav0
              /D=$t"
|     Check and see if the number of points in the triangle fit is 3.
|     If so, then another method for estimating the center position (in
|     pixels) of the atomic line must be used so that
|     ERROR=+/-OFFSET*(width uncertainty in pixels/width in pixels).
|     Since the width in pixels is estimated at 2+/-1 pixels, the error
|     is given by ERROR=+/-OFFSET/2
      if (V_npnts == 3)
          W_sigma[0]=0;W_sigma[1]=0
```

```
            W_sigma[2]=abs(coeff[2]-round(coeff[2]))/2
         endif
|        print out the results of the triangle fit to the atomic line
         print "File "+pref1+suf1+".prn TRIANGLE fit:ywave=y"+suf1+",
            xwave=wav0, fitwave=t"+suf1+", V_chisq=",V_chisq
         printf "coeff={%9.4f,%9.4f,%9.4f}
         W_sigma={%9.4f,%9.4f,%9.4f}",coeff[0],coeff[1],coeff[2],
                 W_sigma[0],W_sigma[1],W_sigma[2];print""
|        Determine the wavenumber position uncertainty from the atomic
|        position uncertainty in pixels.
         printf "wavenumber position uncertainty=%9.4f",1e8/2/c[3]/
            W_sigma[2]*(sqrt(1+(2*c[3]*W_sigma[2]/c[1])^2)-1);print""
|        Redefine peak1 string to contain current fitting parameters for
|        atomic line
         peak1="coeff={"+num2str(coeff[0])+","+num2str(coeff[1])+","+
            num2str(coeff[2])+"}"
|        Make ram string name for this run (pref1[1,6] designates run date,
|        i.e., 021295).
         ram="ram"+pref1 [1,6]+suf1;wavnum="wavnum"+suf1
|        Define wavenumber scale and make fit and error coefficient array
|        (indices 17-19 & 37-39 are reference fit and error)
         make/d/n=578 $wavnum=1e8*(1/c[0]-1/(c[1]-c[3]*(coeff[2]-wav0)))
         make/d/n=40 $ram
         wave rm = $ram
|        store reference PIXEL position and uncertainty in coefficient
|        array
         rm[19]=coeff[2];rm[39]=W_sigma[2]
         rm[17]=coeff[0];rm[37]=W_sigma[0]
         rm[18]=coeff[1];rm[38]=W_sigma[1]
|        Delete Reference Graph
         dowindow/k $gra
|        make dummy wave for y data in order to delete "bad points"
         duplicate/d/o $y dum1
|        display Raman Graph
         PauseUpdate | building window...
         execute "Display /W=(5,42,400,250) dum1,$b,$t vs $wavnum"
         dowindow/c $gra
         execute"ModifyGraph mode(dum1)=3"
         execute"ModifyGraph marker(dum1)=8"
         execute"ModifyGraph rgb($b)=(0,65000,0),rgb($t)=(0,0,65000)"
         SetAxis/a
         Cursor A dum1 164;Cursor B dum1 334
         ShowInfo
|        Show button on graph that when pressed deletes bad point that
|        Cursor A is presently on.
         Button button0 proc=ButtonProc,title="Zap"
|        print out STATEMENT for revising coeff wave for Raman fit
|        parameters (simply by backspacing and typing 4 or 5 before hitting
|        return one can obtain the current parameters in string peak4 or
|        string peak5 for 4 or 5 Raman lines).
         print "print peak3"
End
```

```
Function ButtonProc(ctrlName) : ButtonControl
      String ctrlName

|     Create button for use with the Raman graph to eliminate "bad
|     points" from being used in the fitting routines.
      Wave w= $CsrWave(A)
      w[pcsr(A)]= NaN
End


function Raman2()
|     THIS FUNCTION FITS THE RAMAN LINES ACCORDING TO THE FITTING
|     PARAMETERS GIVEN, AUTOSCALES THE GRAPH, AND SAVES THE GRAPH AS A
|     GRAPH MACRO IN THE PROCEDURE SO THAT IT MAY BE REBUILT WHEN
|     DESIRED.

      variable i        | local count variable
      variable V_chisq
      variable/g nm      | global variable for number of Raman peaks in
                         | run
|     peak1a, peak2, peak3, peak4, and peak5 store default Raman fitting
|     parameters for one, two, three, four, and five Raman lines in a
|     run.
      string/g y,b,t,gra,ram,rme,wavnum,ft,st,peak1a,peak2,peak3,peak4,
                  peak5,pref1,suf1
|     local dummy string for storing revised default Raman fitting
|     parameters after fitting this run
      string peak
      wave coeff=coeff,W_sigma=W_sigma,c=c
|     waves for finding uncertainty in Raman line position due to
|     uncertainty in reference neon line
      make/d/o/n=5 llr=0,dl=0,pr=0,spr=0,sdl2=0,slr2=0,sdvr=0
|     llr=equivalent Raman wavelength
|     dl=wavelength difference between Raman line and reference line
|     pr=reference line pixel position; spr=reference line pixel
|          uncertainty (sigma)
|     sdl2=wavelength difference variance
|     slr2=total wavelength variance in Raman line
|     sdvr=total wavenumber uncertainty in Raman line position

|     Determine if run contains one, two, three, four, or five Raman
|     peaks.
      nm=(numpnts(coeff)-2)/3
      if ((nm==1)%|(nm==2))
            if (nm==1)
                  ft="ONETILT"
            else
                  ft="DBLTILT"
            endif
      else
            if ((nm==3)%|(nm==4))
                  if (nm==3)
                        ft="TRIPLETILT"
```

```
                  else
                        ft="QUADRATILT"
                  endif
            else
                  ft="QUINTATILT"
            endif
      endif
```
Perform Lorentzian fit to Raman peaks
(If necessary, one may abort the fit during the fitting routine
without aborting the RAMAN2 function so as to adjust the fitting
parameter "guesses" by typing "." while holding down the command
key. Also, one can prematurely end the fitting routine at
the current iteration by clicking on the QUIT button. The
function will then proceed to the end using the fitting parameters
obtained at the end of that iteration. By default, Igor tries up
to 40 iterations, but will quit if 9 iterations in sequence do not
produce a decrease in chi-square.)
```
execute"FuncFit/q $ft coeff dum1(xcsr(A),xcsr(B))  /X=$wavnum
          /D=$b"
wave rm=$ram
```
Assign fitting coefficients and uncertainties to coefficient array
(34 elements are allocated for up to five Raman lines, background
slope, and background amplitude)
```
rm[0,nm*3-1]=coeff[x]
rm[20,nm*3+19]=W_sigma[x-20]
```
include reference line position uncertainty in Raman line position
uncertainty.
      find Raman wavelengths
```
llr[0,nm-1]=1/(1/c[0]-coeff[3*x+2]/1e8)
```
      find wavelength difference
```
dl[0,nm-1]=c[1]-llr[x]
```
      find Raman pixel position
```
pr[0,nm-1]=rm[19]-dl[x]/c[3]
```
      find the uncertainty in the Raman pixel position (due to
      fitting)
```
spr[0,nm-1]=1e8/2/c[3]*(1/(1e8/llr[x]-W_sigma[3*x+2])-
      1/(1e8/llr[x]+W_sigma[3*x+2]))
```
      find variance in the wavelength difference
```
sdl2[0,nm-1]=(dl[x])^2/(rm[19]-pr[x])^2*(rm[39]^2+spr[x]^2)
```
      find total wavelength variance in Raman line
```
slr2[0,nm-1]=sdl2[x]
```
      find total wavenumber uncertainty in Raman line position
```
sdvr[0,nm-1]=1e8*sqrt(slr2[x])/llr[x]^2
```

Place total wavenumber uncertainty of Raman line position into
coefficient array
```
rm[22,nm*3+19;3]=sdvr[(x-22)/3]
```

Place background amplitude and slope into coefficient array
```
rm[15,16]=coeff[x-(5-nm)*3]
rm[35,36]=W_sigma[x-(5-nm)*3-20]
```
print out results of fit

```
print ft+" fit:ywave=y"+suf1+", xwave=wavnum"+suf1+",
      fitwave=b"+suf1+", V_chisq=",V_chisq
peak="coeff={"
i=0
do
      st="["+num2str(i*3)+"]={%8.4f,%6.4f,%8.4f}"
      printf ("coeff"+st+" W_sigma"+st),rm[i*3],rm[i*3+1],
            rm[i*3+2],rm[i*3+20],rm[i*3+21],rm[i*3+22];print""
      printf ("wavenumber position fit error=%8.4f"),
            W_sigma[i*3+2];print""
      peak=peak+num2str(rm[i*3])+","+num2str(rm[i*3+1])+","+
            num2str(rm[i*3+2])+","
      i+=1
while(i < nm)
st="["+num2str(i*3)+"]={%6.4f,%8.4f}"
printf ("coeff"+st+" W_sigma"+st+"/r"),rm[15],rm[16],rm[35],rm[36]
peak=peak+num2str(rm[15])+","+num2str(rm[16])+"}"
if ((nm==1)%|(nm==2))
      if (nm==1)
            peak1a=peak
      else
            peak2=peak
      endif
else
      if ((nm==3)%|(nm==4))
            if (nm==3)
                  peak3=peak
            else
                  peak4=peak
            endif
      else
            peak5=peak
      endif
endif

kill window and make graph with "true" data
dowindow/k $gra
execute "display /w=(5,42,400,250) $y,$b,$t vs $wavnum"
dowindow/c $gra
execute "ModifyGraph mode($y)=3"
execute "ModifyGraph marker($y)=8"
execute "ModifyGraph rgb($b)=(0,65000,0),rgb($t)=(0,0,65000)"

make graph macro and kill window
dowindow/n $gra; dowindow/k $gra

End
```

```
|Raman wave statistics

function Stat()
      variable/g ct=0
      variable i,j |i=wave index,j=wave number
      variable/d sum1,sum2,sumx,sumxb,sumstd,count
      string/g y,z,ref1,ls=" ",prom1="Enter name of statistics wave"
      execute "statname()"
      GetRam()
      make/d/o/n=40 $ref1=0, stdstat=0, weightstat=0
      wave reff=$ref1
      THE PURPOSE OF THE STAT FUNCTION IS TO CALCULATE THE MEAN AND
      UNCERTAINTY IN THE MEAN USING WEIGHTED STATISTICAL AVERAGING.  THE
      FUNCTION USES THE RELATIVE UNCERTAINTIES (FITTING UNCERTAINTIES)
      TO WEIGHT THE CALCULATION OF THE ESTIMATED VARIANCE.  THE
      CALCULATION OF THE MEAN SIMPLY USES THE RELATIVE UNCERTAINTIES,
      BUT THE UNCERTAINTY IN THE MEAN REQUIRES KNOWLEDGE OF THE
      ESTIMATED VARIANCE (WHICH IS DIVIDED BY N TO FIND THE VARIANCE IN
      THE MEAN).  THE WAVES TO BE AVERAGED MUST BE 40 ELEMENTS LONG, THE
      FIRST 20 BEING THE DATA POINTS AND THE LAST 20 BEING THE
      CORRESPONDING UNCERTAINTIES IN THESE DATA POINTS.  OFTEN, SOME
      DATA POINTS MAY HAVE UNCERTAINTIES OF ZERO.  THE AVERAGING
      PROCEDURE IGNORES THESE POINTS AND KEEPS TRACK ONLY OF THOSE
      POINTS WHOSE UNCERTAINTIES ARE NONZERO.  THUS, EVEN THOUGH 15
      MEASUREMENTS MAY HAVE BEEN MADE FOR EACH QUANTITY OF INTEREST, THE
      AVERAGE OF QUANTITY A MAY ONLY REPRESENT 12 MEASUREMENTS WHILE THE
      AVERAGE OF QUANTITY B MAY ONLY REPRESENT 14 MEASUREMENTS.  FOR
      RAMAN DATA, THIS COULD BE THE CASE IF A RAMAN LINE DOESN'T APPEAR
      FOR SOME OF THE MEASUREMENTS.  THE FUNCTION ALSO CREATES TWO DUMMY
      WAVES, STDSTAT AND WEIGHTSTAT, FOR COMPARING EQUAL WEIGHTING WITH
      THE WEIGHTING BASED ON THE RELATIVE UNCERTAINTIES OF THE DATA
      POINTS.  OF COURSE, WEIGHTSTAT IS A DUPLICATE OF THE WAVE NAMED BY
      THE USER FOR STORAGE OF THE STATISTICAL DATA.

      Refer to Philip R. Bevington, DATA REDUCTION AND ERROR ANALYSIS
      FOR THE PHYSICAL SCIENCES (McGraw Hill Book Co., New York, 1969),
      pp. 66-80.

      Calculate Raman statistics of waves
      i=0
      do
            j=0
            sum1=0;sum2=0;sumx=0;count=0
            do
                  z=GetStrFromList(ls,j,";")
                  wave zq=$z
                  if (zq[i+20] != 0)
      find sum of data for calculating the mean
                        sumx=sumx+zq[i]
      find sum of the data points divided by their relative variances
      for finding weighted mean
                        sum1=sum1+zq[i]/zq[i+20]^2
```

```
            find sum of the inverse of the relative variances for finding the
            weighted mean and the average variance
                        sum2=sum2+1/zq[i+20]^2
      count the number of data points with nonzero uncertainties
                        count+=1
                  endif
                  j+=1
            while(j < ct)
            j=0
            sumstd=0;sumxb=0
            do
                  z=GetStrFromList(ls,j,";")
                  wave zq=$z
                  if (zq[i+20] != 0)
      sum of the square of the errors for finding the standard
      uncertainty in the mean
                        sumstd=sumstd+(zq[i]-sumx/count)^2
      sum of the square of the errors weighted by the relative
      uncertainties for finding the average variance (divide sumxb by
      N-1, then normalize by dividing this quantity by sum2/N to get
      average variance--divide average variance by N to get variance in
      the mean)
                        sumxb=sumxb+(zq[i]-sumx/count)^2/zq[i+20]^2
                  endif
                  j+=1
            while(j < ct)

            if (count > 1)
      find the equal-weighted mean and the uncertainty in the mean
                  stdstat[i]=sumx/count;
                        stdstat[i+20]=sqrt(sumstd/(count-1)/count)
      find the weighted mean and its respective uncertainty
                  weightstat[i]=sum1/sum2;
                        weightstat[i+20]=sqrt(sumxb/sum2/(count-1))
            endif
            reff[i]=weightstat[i];reff[i+20]=weightstat[i+20]
            i+=1
      while(i < 20)
      kill all loaded waves except statistics wave
      j=0
      do
            z=GetStrFromList(ls,j,";")
            wave zq=$z
            killwaves zq
            j+=1
      while(j < ct)
      ls="";ct=0
End
```

```
macro statname(ref)
|     obtain name of statistics (reference) wave
      string ref="ref010195",prom=prom1
      prompt ref, prom
      ref1=ref;prom1=prom
endmacro

function GetRam()
      string/g suf1="A",pref1="RAM010195",
          pat1="Data:Joe Binford:DATAstor3:fun Folder:",ext1="BWAV",y,
          z,ls
      variable/g ct=0,refer
|     start loop
      do
|     Obtain suffix, prefix, path and extension of wave
          execute "GetWave()"
|     Check and make sure that the suffix doesn't equal "" or
|     "reference".  If the suffix equals "" then for the statistics or
|     graphing macros, this means that you are finished loading the
|     waves.  If the suffix equals "reference" then for the graphing
|     macros, this means that not only are you finished loading the
|     waves, but that the very last wave is to be used as a reference in
|     computing %change in Raman width, shift, etc.
          if ((CmpStr(suf1,"") != 0)%&(CmpStr(suf1,"reference")!=0))
|             load Raman run
              newpath/q/o np pat1
              LoadWave/q/h/o/p=np pref1+suf1+"."+ext1
|     The following routine is used basically to keep track of the wave
|     names in string ls.
              if (CmpStr(ls,"") != 0)
                  if (CmpStr(ls," ") == 0)
                      ls=""
                  endif
                  ls=ls+pref1+suf1+";"
              endif
              ct+=1
          endif
      while ((CmpStr(suf1,"") != 0)%&(CmpStr(suf1,"reference")!=0))
      if (CmpStr(suf1,"reference")==0)
          ct=ct-1;refer=1
      else
          refer=0
      endif
End
```

|Raman Graph Procedures

Function RamGraph()
| THIS FUNCTION ENABLES THE USER TO COMPILE RAMAN DATA IN A FORM
| WHICH CAN BE GRAPHED IN A "BAR CHART" FORMAT. THIS FIRST FUNCTION
| ONLY COMPILES QUANTITIES WHICH COME FROM EACH INDIVIDUAL RUN. IN
| OTHER WORDS, NO COMPARISONS ARE MADE WITH DATA FROM OTHER RUNS
| SUCH AS A "REFERENCE". BESIDES INTENSITY, WIDTH, AND RAMAN SHIFT
| (POSITION), THE TWO COMPUTED QUANTITIES ARE RELATIVE INTENSITY
| (BASED ON THE STRONGEST RAMAN LINE) AND POSITION FROM THE
| REFERENCE (SUCH AS THE NEON ATOMIC LINE). PLEASE NOTE THAT THE
| THREE GRAPHING FUNCTIONS, RAMGRAPH, RAMGRAPHA, AND RAMGRAPH2, MUST
| BE RUN IN A CERTAIN SEQUENCE TO WORK PROPERLY.
| If you simply want graphs of the first five quantities listed
| above, you only need to run RamGraph first and then run RamGrapha.
| Please note that when entering the Raman waves (40 element,
| *.bwav), YOU MUST enter different suffixes. When finished
| entering the waves, type "" for the suffix and press RETURN. This
| signals Igor that you are finished loading waves. RamGraph
| calculates all five quantities, so you only need to run it once
| for graphing all five quantities for a total of five graphs.
| RamGrapha may be run repeatedly for obtaining graphs of all five
| quantities for all combinations of Raman lines and sets of Raman
| data.
| NOTE: For one given quantity, such as width, you must use a
| different graph letter (actually it can be any suffix) for each
| new graph. However, you may use the same graph letter for
| different quantities, such as width and position. So, in other
| words, if you wanted to make two graphs of each quantity, you
| would need to run RamGraph once, then RamGrapha five times, then
| RamGraph again (giving it a graph letter "b"), and then RamGrapha
| five more times for a total of ten graphs. IF YOU WANT TO USE A
| REFERENCE to calculate other quantities such as relative intensity
| (%), change in linewidth, % change in linewidth, or change in
| position, then you must use the function RamGraph2. You must
| return to RamGrapha to graph these new quantities. So the
| sequence is RamGraph, RamGrapha, RamGraph2, RamGrapha. (You may
| not actually need graphs for the first four quantities, but
| RamGraph2 needs them to compile the second set of quantities)
| Also, when loading the waves during the execution of RamGraph, you
| have two options: You may include the reference when graphing the
| other waves or not. In other words, the reference wave would show
| values of 0 for the second set of quantities if you chose to graph
| it along with the other waves. TO LEAVE OUT THE REFERENCE WAVE,
| simply load the other waves, load the reference wave, then enter
| "reference" as the suffix to conclude the loading process and to
| indicate to IGOR that the last wave was the reference wave. Thus
| the loading sequence is: wave1, wave2, wave3,..., waven, refwave,
| "reference". TO INCLUDE THE REFERENCE WAVE, include the reference
| wave in the list of waves and include it again at the end BUT WITH
| A DIFFERENT SUFFIX! To do this, you might have a reference wave
| name of ref061896. You might pick the first suffix to be "6" and

the prefix to be "ref06189". Then, to include the reference wave
at the end, you might load the wave with a suffix of "96" and a
prefix of "ref0618". Of course, it might be more helpful to write
the names down to keep track of them (with prefixes and suffixes)
and to rename them with names which are easier to keep track of
and remember. The loading sequence would then be: wave1, wave2,
refwave, wave3,..., waven, refwave, "reference". It may be easier
to see this sequence by showing suffixes and prefixes. Let's say
you have 5 waves: ram061296a, ramave061396, ram061496b,
ram052396f, and ramave052996 plus your reference ref061896.
You could load these waves as follows (assume the reference is the
3rd wave):
SUFFIX FIRST, PREFIX SECOND
"061296a"+"ram", "061396"+"ramave", "061896"+"ref",
"061496b"+"ram", "052396f"+"ram", "ef061896"+"r"
After loading the waves in RamGraph, you are asked to specify the
sequence of Raman peaks to be displayed in the graph. The
sequence can be in any order and can be up to five peaks. For
6H SiC, the five peaks typically observed in the 790 1/cm region
are the 767, the 777, the 783, the 788, and the 797 Raman lines.
The Raman fitting procedures actually compile the Raman data
according to the following sequence of lines: 767, 788, 797, 777,
783 or the sequence {0,3,4,1,2}. (Note that 0 is the first in the
sequence.) This was because the 767, 788, and 797 are always
present. The 777 line is less frequent and the 783 line is least
frequent of all. However, the RamGraph procedure sorts each wave
individually, sorting the Raman shift from least to greatest.
PLEASE NOTE: currently the major flaw with this procedure is that
the sorting routine doesn't know where to put zeros (nonexistent
lines) so it just ignores them and sorts the other numbers
For instance, the sequence {797 0 788 767 777} sorts as
{767 0 777 788 797} giving an index wave of {4 1 3 0 2}. The
missing Raman line is of course the 783 line, so it should have
sorted as {767 777 0 788 797} giving an index wave of {4 2 3 0 1}.
The trick here is to place the zeroes for the missing Raman lines
where they should go when sorted so that the other lines will fall
into place. For example, by switching the 788 and 0, the
procedure will sort correctly: the sequence {797 788 0 767 777}
sorts as {767 777 0 788 797} with an index wave of {4 3 2 0 1}.
(This step can be done by editing the wave, copying and pasting
the set of three values for the 788 line--in this case, points
3,4, & 5 and pasting them to the 0--points 6, 7, and 8. DON'T
FORGET! ADD 20 and do the same for the uncertainties. Copy and
paste points 23, 24, & 25 to points 26, 27, & 28. Then put zeroes
in for points 3, 4, & 5 and for points 23, 24, & 25. Now to
revise this function, I suppose one could write it to check and
see if the values fall within a couple of wavenumbers of a
standard or reference set of Raman shift values such as the
integers {767 777 783 788 797}. Or better still, have it check
the Raman shift values against the last wave loaded to see if the
values fall within a couple of wavenumbers of each other. This
last wave could be the reference wave containing all of the lines

to be graphed. Of course, another alternative is to make sure the
Raman lines are sorted before running this function (i.e.,
revising the Raman fitting procedures to place the lines
sequentially or just ensuring that the zeroes for the missing
Raman lines are placed correctly. These graphing functions worked
well for me since all of the statistical data contained all five
lines, so that each wave was sorted perfectly (there were no
missing Raman lines in the "composite" waves). RamGraph and
RamGraph2 give the quantity waves wavenames of the form:
"quantityname like WID or DELPOS"+"wave#"+graph letter. If you
load five waves for graph letter a, then there will be five waves
such as WID0a, WID1a, WID2a, WID3a, WID4a. The size of these
waves depends on the number of Raman lines being displayed in the
graph. In these case, if three Raman lines are displayed, then
all but three elements would be zero for spacing in the bar chart.
The possible quantity names are:
INT, WID, POS, RELINT, POSFROMREF for RamGraph and
PERRELINT, DELWID, PERWID, DELPOS for RamGraph2
UNCERTAINTIES for the values in these waves are stored in waves
having respective quantity names with "ERR" in front, such as
ERRINT or ERRWID. Of course, one could add other quantitynames to
RamGraph2, such as PERPOSRELWID, for the percent change in Raman
shift position relative to the reference linewidth, or a
particular quantityname to RamGraph which doesn't require a
reference such as DELPOSINTEG for the Raman shift relative to an
integer value like 788 (i.e., 788.125 returns 0.125 and 787.78
returns -0.22). After running RamGraph2, the execution of
RamGrapha also compiles waves for tabular use of the quantity to
be graphed. These waves have names of the form
"TOT"+"quantityname like WID or DELPOS"+"ramanline#"+graph letter.
The uncertainties in the values of these waves stored in waves
having respective names with "ERR" in front, such as ERRTOTWID or
ERRTOTINT. These waves contain all the data for a particular
quantity, such as the width of the 788 line. If you loaded five
waves, then this wave contains five linewidths of the 788 line.
The way this function is written, you must run RamGraph2 and then
RamGrapha (a second time) for each particular quantity that you
desire to obtain the "TOT" waves for. To do this, the following
sequence must be followed:
RamGraph, RamGrapha, RamGraph2, RamGrapha (for first quantity)
RamGrapha, RamGraph2, RamGrapha (for second quantity)
RamGrapha, RamGraph2, RamGrapha (for third quantity)

```
variables
variable/g ct=0,refer=0,nume
variable i,j,k,l,temp
i=wave index,j=wave number,k/l=arbitrary indices,
      temp=temporary storage
string/g ls=" ",y1,y2a,y2b,z2,z2s,typ1,sumy2a,sumy2b,run,pz
known parameters
make/d/o/n=5 c={5321.0379,5562.7662,0,.113079,.365857}
make/d/o/n=5 ce={0.0026,0.0001,0,0.000022,0.000070}
```

```
c[2]=1e8*(1/c[0]-1/c[1])
ce[2]=1e8*sqrt((ce[0]/c[0]^2)^2+(ce[1]/c[1]^2)^2)
GetRam()
z2="int;wid;pos;relint;posfromref;"
z2s="0)None 1)Intensity 2)Width 3)Position 4) Rel. Strength
      5) Pos. From Ref."
make/o nd={0,1,2,3,4}, ne={0,1,2,3,4}
pz="Enter the letter of the graph (i.e., a)"
typ1="a"
execute"prmpt()"
typ1="run=\""+typ1+"\""
execute typ1
pz="Enter the sequence of peaks to be included, from left to right
     (i.e. 0,3,1)"
typ1="{0,1,2,3,4}"
execute"prmpt()"
typ1="make/o ne="+typ1
execute typ1
nume=numpnts(ne)
typ1="1"
Cycle through each wave for the graph, building the graph.
j=0
do
Get wavename from list
     y1=GetStrFromList(ls,j,";")
     wave yq1=$y1
     sort Raman lines (ignoring 0's, meaning nonexistent lines)
     (This sort routine works, but ignores 0's, meaning that if
     the 0's aren't in the proper position--such as zeroes in
     indices 1 and 2 for the 777 and 783 lines, then the
     resultant "sorted" wave will be incorrect with respect to a
     sorted wave containing all five lines.
     k=0
     do
          if (yq1[2+3*nd[k]]!=0)
               l=k+1
               do
                    if ((yq1[2+3*nd[l]]<yq1[2+3*nd[k]])
                              %& (yq1[2+3*nd[l]]!=0))
                         temp=nd[l];nd[l]=nd[k];nd[k]=temp
                    endif
                    l+=1
               while (l<5)
          endif
          k+=1
     while (k<4)

     i=0
     do
make quantity waves to store values for graphs (dummy wavenames
yq2a and respective error yq2b)
          y2a=GetStrFromList(z2,i,";")+num2str(j)+run;
```

```
                        y2b="err"+y2a
                make/d/o/n=(nume*(ct+1))  $y2a=0,$y2b=0
                wave yq2a=$y2a,yq2b=$y2b
                if ((refer==1)%&(j==ct))
                        j=0;refer=2
                endif
get quantity if intensity, width, or position
                if (i<3)
                        yq2a[j, ;ct+1]=yq1[i+3*nd[ne[(p-j)/(ct+1)]]];
                        yq2b[j, ;ct+1]=yq1[20+i+3*nd[ne[(p-j)/(ct+1)]]]
                else
                        if (i==3)
get quantity if relative intensity
                                yq2a[j, ;ct+1]=yq1[3*nd[ne[(p-j)/
                                        (ct+1)]]]/yq1[3*nd[3]]
                                yq2b[j, ;ct+1]=yq2a*sqrt((yq1[20+3*
                                        nd[ne[(p-j)/(ct+1)]]]/
                                        yq1[3*nd[ne[(p-j)/(ct+1)]]])^2+
                                        (yq1[20+3*nd[3]]/yq1[3*nd[3]])^2)
                        else
get quantity if position from reference
                                yq2a[j, ;ct+1]=yq1[2+3*nd[ne[(p-j)/
                                        (ct+1)]]]-yq1[19]
                                yq2b[j, ;ct+1]=sqrt((yq1[22+3*nd[ne[(p-j)/
                                        (ct+1)]]])^2+(yq1[39])^2)
                                k=0
                                do
check if position=0--if so, then make these values in the quantity
waves=0
                                        if (yq1[2+3*nd[ne[k]]]==0)
                                                yq2a[j+k*(ct+1)]=0;
                                                        yq2b[j+k*(ct+1)]=0
                                        endif
                                        k+=1
                                while(k<nume)
                        endif
                endif
                if ((refer==2)%&(j==0))
                        j=ct;refer=1
                endif
                i+=1
        while (i<5)

        j+=1
while (j<(ct+refer))

End
```

```
Macro Prmpt(typ)
|     obtain type of graph
      string/g pz
      string typ=typ1
      prompt typ, pz
      typ1=typ
EndMacro


Function RamGrapha()
      string/g z2s,typ1,pz=z2s
|     Display bar graph of int,wid,pos,relint, posfromref, perrelint,
|     delwid, perwid, or delpos vs Raman line for each run
      execute"Prmpt()"
      if (CmpStr(typ1,"0") != 0)
            GraphWin()
      endif
End


Function GraphWin()
|     See Comments for RamGraph() for additional information about
|     RamGrapha (or GraphWin)
|     Variables
      variable i,j,pow1,pow2,tot1a,tot1b,tot2,sigfig
      variable/d m,n
      variable/g ct,rn,nume
      string/g y2a,y2b,yra,yrb,yrc,yrd,sum2a,sum2b,z2,typ1,lb,lb0,lb1,
            lb2,lb3,lb4,lb5,lb6,lb7,lb8,t1,taa,tbb,tcc,tdd
      string/g tta,tbl,errtbl,tblist="",sumy2a,sumy2b,run,ls
      PauseUpdate | building window...
|     Define possible labels for y axis
      lb0="Intensity Counts"
      lb1="Raman Line Width (cm\\S-1\\M)"
      lb2="Raman Shift (cm\\S-1\\M)"
      lb3="Relative Raman Line Strength"
      lb4="Raman Line Offset From Neon Reference (cm\\S-1\\M)"
      lb5="Percent Change in Relative Raman Line Strength"
      lb6="Change in Raman Line Width (cm\\S-1\\M)"
      lb7="Percent Change in Raman Line Width (%)"
      lb8="Change in Raman Shift (cm\\S-1\\M)"
      lb=lb0+";"+lb1+";"+lb2+";"+lb3+";"+lb4+";"+lb5+";"+lb6+";"+lb7+
            ";"+lb8+";"
      sumy2a="";sumy2b=""
|     Build up list of quantity names
      j=0
      do
            y2a=GetStrFromList(z2,str2num(typ1)-1,";")+num2str(j)+run
            sumy2a=sumy2a+y2a+","
            sumy2b=sumy2b+"err"+y2a+","
            j+=1
      while(j<ct)

|     display bar graph
```

```
y2a=GetStrFromList(sumy2a,0,",")
wave yq2a=$y2a
execute "Display /W=(5,43,627,464) $y2a"
j=1
do
      y2a=GetStrFromList(sumy2a,j,",")
      wave yq2a=$y2a
      execute "AppendToGraph $y2a"
      j+=1
while(j<ct)
ModifyGraph font="Arial"
ModifyGraph mode=5
ModifyGraph hbFill=4
ModifyGraph offset={-0.5,0}
ModifyGraph grid(left)=2
ModifyGraph tick(left)=2,tick(bottom)=3
ModifyGraph mirror=1
ModifyGraph minor(left)=1
ModifyGraph sep(left)=2
ModifyGraph noLabel(bottom)=1
ModifyGraph lblMargin(bottom)=1
ModifyGraph axOffset(left)=-2
Label left GetStrFromList(lb,str2num(typ1)-1,";")
y2a=GetStrFromList(sumy2a,round(ct/2-0.5),",")
if (str2num(typ1)>4)
for plotting quantities in the first set (intensity, width,
position, relinten, posfromreference)
      Label bottom "Reference Specimen Raman Lines
                     (Position/Width) Observed"
      i=0
      do
            Determine decimal places for tag (for listing value
            and uncertainty on each bar)
            j=0
            tta="\\JC\\F'Arial'\\Z10"
            do
                  yra=GetStrFromList(z2,2-j,";")+num2str(rn)+run
                  yrb="err"+yra
                  wave yqra=$yra,yqrb=$yrb
                  tot1a=1;tot1b=1;sigfig=3
                  if (yqra[i*(ct+1)]!=0)
                        pow1=round(log(abs(yqra[i*(ct+1)]))-0.5)
                  else
                        pow1=0
                  endif
                  pow2=round(log(yqrb[i*(ct+1)])-0.5)
                  tot2=sigfig-1-pow2
                  if (tot2<1)
                        tot2=0;tot1a=tot1a-1;tot1b=tot1b-1
                  endif
                  tot1a=tot1a+tot2+1;tot1b=tot1b+tot2+1
                  if (yqra[i*(ct+1)]<0)
```

```
                                        tot1a=tot1a+1
                        endif
                        if (pow1>0)
                                tot1a=tot1a+pow1
                        endif
                        if (pow2>0)
                                tot1b=tot1b+pow2
                        endif
                        taa="%"+num2str(tot1a)+"."+num2str(tot2)+"f"
                        sprintf tcc, taa, yqra[i*(ct+1)]
                        tta=tta+tcc
                        if (j==0)
                                tta=tta+" cm\\S-1\\M\r\\F'Arial'\\Z10("
                        else
                                tta=tta+" cm\\S-1\\M)"
                        endif
                        j+=1
                while(j<2)
                Tag/F=0/A=MT/L=0 $y2a, round(ct/2-0.5)+i*(ct+1), tta
                i+=1
        while(i<nume)
else
for plotting quantities in the second set (using reference wave)
        Label bottom "Approximate Raman Lines Observed"
        yra=GetStrFromList(z2,2,";")+"0"+run
        yrc=GetStrFromList(z2,1,";")+"0"+run
        wave yqra=$yra,yqrc=$yrc
        i=0
        do
                Tag/F=0/A=MT/L=0/P=10 $y2a, round(ct/2-0.5)+i*(ct+1),
                        "\\JC\\F'Arial'\\Z10"+
                        num2str(round(yqra[i*(ct+1)]))+" cm\\S-1\\M"
                i+=1
        while(i<nume)
endif
Textbox/N=textc/F=0/A=MT/E "\\JC\\F'Arial'\\Z14"+
        GetStrFromList(z2,str2num(typ1)-1,";")
Textbox/N=textd/F=0/A=RB/X=-0.91/Y=-34.77
        "\\F'Arial'\\Z10J. Binford\r"+Secs2Date(DateTime,0)
Textbox/N=textb/F=0/A=MC/X=18.28/Y=-32.81
        "\\F'Arial'\\Z10Laser wavelength is 532.10379±0.00026 nm"
AppendText "Neon reference wavelength is 556.276620±0.000010 nm\r
                Wavenumber difference is 816.6582±0.0092 cm\\S-1\\M"
Legend/J/N=texta/F=0/A=MB/X=0.80/Y=1.90/E ""
i=0
create waves of quantity with specimen for each peak ("TOT" waves)
do
        tbl="tot"+GetStrFromList(z2,str2num(typ1)-1,";")+
                num2str(i)+run;errtbl="err"+tbl
        tblist=tblist+tbl+";"
        make/d/o/n=(ct) $tbl=0,$errtbl=0
        i+=1
```

```
while(i<nume)
j=0
do
        y2a=GetStrFromList(sumy2a,j,",");
            y2b=GetStrFromList(sumy2b,j,",")
        wave yz1=$y2a,yz2=$y2b
        ErrorBars/Y=15 $y2a Y,wave=(yz2,yz2)
        t1="\\s("+y2a+") "+GetStrFromList(ls,j,";")
        AppendText/n=texta t1
        i=0
        do
                tbl=GetStrFromList(tblist,i,";");errtbl="err"+tbl
                wave wtbl=$tbl,etbl=$errtbl
                if (yz2[j+i*(ct+1)]!=0)
                        Determine decimal places for tag
                        tot1a=1;tot1b=1;sigfig=3
                        if (yz1[j+i*(ct+1)]!=0)
                                pow1=round(log(abs(yz1[j+i*(ct+1)])))-0.5)
                        else
                                pow1=0
                        endif
                        pow2=round(log(yz2[j+i*(ct+1)])-0.5)
                        tot2=sigfig-1-pow2
                        if (tot2<1)
                                tot2=0;tot1a=tot1a-1;tot1b=tot1b-1
                        endif
                        tot1a=tot1a+tot2+1;tot1b=tot1b+tot2+1
                        if (yz1[j+i*(ct+1)]<0)
                                tot1a=tot1a+1
                        endif
                        if (pow1>0)
                                tot1a=tot1a+pow1
                        endif
                        if (pow2>0)
                                tot1b=tot1b+pow2
                        endif
                        taa="%"+num2str(tot1a)+"."+num2str(tot2)+"f"
                        tbb="%"+num2str(tot1b)+"."+num2str(tot2)+"f"
                        sprintf tcc, taa, yz1[j+i*(ct+1)]
                        sprintf tdd, tbb, yz2[j+i*(ct+1)]
                        Tag/F=0/A=LB/L=0/O=90/X=0/Y=0 $y2a, j+i*(ct+1),
                                "\\JR\\F'Arial'\\Z08"+tcc+"\r±"+tdd
                        wtbl[j]=round(yz1[j+i*(ct+1)]*
                                10^(tot2)-0.5)/10^(tot2)
                        etbl[j]=round(yz2[j+i*(ct+1)]*
                                10^(tot2)-0.5)/10^(tot2)
                endif
                i+=1
        while(i<nume)
        j+=1
while(j<ct)
End
```

```
Function RamGraph2()
      See Comments for RamGraph() for additional information about
      RamGraph2
      variables
      variable/g ct,refer,nume,rn=-1 |reference number
      variable i,j,k,l,temp |i=wave index,j=wave number,k/l=arbitrary
                            |indices,temp=temporary storage
      variable u,v |t/v=arbitrary indices
      string/g ls,y1a,y1b,yra,yrb,y2a,y2b,z2,z2s,typ1="1",sumy2a,sumy2b
      string/g prom1="Enter name of reference wave",ref1,run,pz
      z2=z2+"perrelint;delwid;perwid;delpos;"
      z2s="0)None 6)%Del in Rel. Strength 7)Width Del 8)%Del in Width
            9) Del in Pos."
      Assign reference position
      rn=ct

      make/o nd={3,1,1,2} |locations of relint, wid, wid, and pos for
                          |four parameters requiring reference
      j=0
      do
            i=5
            do
                  y1a=GetStrFromList(z2,nd[i-5],";")+num2str(j)+
                        run;y1b="err"+y1a
                  yra=GetStrFromList(z2,nd[i-5],";")+num2str(rn)+
                        run;yrb="err"+yra
                  y2a=GetStrFromList(z2,i,";")+num2str(j)+
                        run;y2b="err"+y2a
                  make/d/o/n=(nume*(ct+1)) $y2a=0,$y2b=0
                  wave yq1a=$y1a,yq1b=$y1b,yqra=$yra,yqrb=$yrb,
                        yq2a=$y2a,yq2b=$y2b

      for calculating change in relative strength or %change in width
      relative to reference.
                  if ((i==5) %| (i==7))
                        k=0
                        do
                              u=j+k*(ct+1)
                              v=k*(ct+1)
                              if ((yqra[v]!=0)%&(yq1a[u]!=0))
                                    yq2a[u]=100*(yq1a[u]/yqra[v]-1)
                                    yq2b[u]=100*abs(yq1b[u]/yqra[v])
                                    if (yq2a[u]==0)
                                          yq2b[u]=0
                                    endif
                              endif
                              k+=1
                        while(k<nume)
                  else
      for calculating change in width or change in position relative to
      reference
                        k=0
```

```
                            do
                                    u=j+k*(ct+1)
                                    v=k*(ct+1)
                                    if ((yqra[v]!=0)%&(yq1a[u]!=0))
                                            yq2a[u]=yq1a[u]-yqra[v]
                                            yq2b[u]=yq1b[u]
                                            if (yq2a[u]==0)
                                                    yq2b[u]=0
                                            endif
                                    endif
                                    k+=1
                            while(k<nume)
                    endif
                    i+=1
            while (i<9)

            j+=1
        while (j<ct)
End


|Atomic Line Fitting Menu

Menu "Macros"
        "InitAtom/0"
        "AtomGraph/1"
        "RepeatAtom/2"
        "AtomStat/3"
End



|Atomic Line Fitting Procedures

Function InitAtom()
        string/g suf1="A",pref1="T010195",
            pat1="Data:Joe Binford:DATAstor3:",ext1="prn"
        string/g peak1="coeff={839,325.5,350.5}"
        string/g peak2="coeff={839,325.5,350.5}"
        string/g peak3="coeff={839,325.5,350.5}"
|       known parameters (atomic lines for finding wavelength dispersion
|       (& also laser wavelength if applicable)
        variable/g/d l12=(507.42007+508.03852)/2,
            diff12=508.03852-507.42007
        Execute "atomgraph()"
End

function atomgraph()
|       THE PURPOSE OF INITATOM, ATOMGRAPH, AND REPEATATOM IS TO FIT
|       TRIANGLE FUNCTION TO ATOMIC LINES SUCH AS NEON IN ORDER TO
|       ACCURATELY DETERMINE THEIR POSITIONS (IN PIXELS) AND ULTIMATELY
|       DETERMINE THE WAVELENGTH DISPERSION (& LASER WAVELENGTH IF
|       APPLICABLE).
```

```
        Note:  In the procedure window, the maximum number of elements in
|       the stat wave is 12, not 40.  In other words, there are six
|       parameters and six uncertainties instead of 20 parameters and 20
|       uncertainties.
        string/g y,t,gra,las,pat1,pref1,suf1,ext1,peak1
        variable/g/d am=2,ami=0  |number of atomic lines to fit/iteration
                                 |number
|       if am=2 just find wavelength dispersion
|       if am=3 find both wavelength dispersion and wavelength of third
|       line (laser line)
        wave wav0=wav0
|       obtain path and prefix of wave
        execute "GetWave()"
|       load Raman run
        newpath/q/o np pat1
        loadwave/g/d/q/n=wav/p=np pref1+suf1+"."+ext1
        y="y"+suf1
        rename wav1,$y
|       display reference graph
        t="t"+suf1
        make/d/n=578 $t
|       building window...

        execute "display /w=(5,42,400,250) $y,$t vs wav0"
        gra="g"+pref1+suf1
        dowindow/c $gra
        execute "ModifyGraph mode($y)=3"
        execute "ModifyGraph marker($y)=8"
        execute "ModifyGraph rgb($t)=(0,0,65000)"
        SetAxis/A
        Cursor A $y 348;Cursor B $y 351
        ShowInfo
        make/d/o/n=3 coeff=0,W_sigma=0

        las="las"+pref1 [1,6]+suf1
        make/d/n=12 $las

        print peak1

end

function RepeatAtom()
        string/g y,t,gra,las,peak1,peak2,peak3,pref1,suf1
        string peak,pk
        variable/d/g V_npnts,V_chisq,am,ami=ami+1,diff12,l12
        wave wav0=wav0,coeff=coeff,W_sigma=W_sigma,ls=$las
|       Perform triangle fit to reference
        execute"FuncFit/q TRIANGLE coeff $y(xcsr(A),xcsr(B))  /X=wav0
                /D=$t"
        if (V_npnts == 3)
            W_sigma[0]=0;W_sigma[1]=0;W_sigma[2]=abs(coeff[2]-
                round(coeff[2]))/2
```

```
        endif
        print "File "+pref1+suf1+".prn TRIANGLE fit:ywave=y"+suf1+",
            xwave=wav0, fitwave=t"+suf1+", V_chisq=",V_chisq
        printf "coeff={%9.4f,%9.4f,%9.4f} W_sigma={%9.4f,%9.4f,%9.4f}",
            coeff[0],coeff[1],coeff[2],W_sigma[0],W_sigma[1],
            W_sigma[2];print""
        peak="coeff={"+num2str(coeff[0])+","+num2str(coeff[1])+","+
            num2str(coeff[2])+"}"
        if ((ami==1)%|(ami==2))
            if (ami==1)
                peak1=peak
            else
                peak2=peak
            endif
        else
            peak3=peak
        endif

|       store atomic PIXEL position and uncertainty in coefficient array
        if (ami==3)
            ls[0]=coeff[2];ls[6]=W_sigma[2]
        else
            ls[ami]=coeff[2];ls[ami+6]=W_sigma[2]
        endif

        if (((am==2)%&(ami==2))%|((am==3)%&(ami==3)))
            ls[3]=(ls[1]+ls[2])/2
            ls[9]=sqrt(ls[7]^2+ls[8]^2)/2
            ls[4]=diff12/(ls[2]-ls[1])
            ls[10]=ls[4]*2*ls[9]/(ls[2]-ls[1])
            if(am==3)
                ls[5]=l12-(ls[3]-ls[0])*ls[4]
                ls[11]=sqrt((ls[4]*ls[9])^2+(ls[4]*ls[6])^2+
                    ((ls[3]-ls[0])*ls[10])^2)
            endif
| kill graph window
            dowindow/k $gra
        else
            Setaxis/a
            print"print peak2"
        endif

End

|Atomic line statistics

macro atomstatname(ref)
|       obtain name of statistics (reference) wave
        string ref="ref010195",prom=prom1
        prompt ref, prom
        ref1=ref;prom1=prom
endmacro
```

```
function AtomStat()
      variable/g ct=0
      variable i,j  |i=wave index,j=wave number
      variable/d sum1,sum2,sumx,sumxb,sumstd,count
      string/g y,z,ref1,ls=" ",prom1="Enter name of statistics wave"
      execute "atomstatname()"
      GetRam()
      make/d/o/n=12 $ref1=0, stdstat=0, weightstat=0
      wave reff=$ref1
|     THE PURPOSE OF THE STAT FUNCTION IS TO CALCULATE THE MEAN AND
|     UNCERTAINTY IN THE MEAN USING WEIGHTED STATISTICAL AVERAGING.  THE
|     FUNCTION USES THE RELATIVE UNCERTAINTIES (FITTING UNCERTAINTIES)
|     TO WEIGHT THE CALCULATION OF THE ESTIMATED VARIANCE.  THE
|     CALCULATION OF THE MEAN SIMPLY USES THE RELATIVE UNCERTAINTIES,
|     BUT THE UNCERTAINTY IN THE MEAN REQUIRES KNOWLEDGE OF THE
|     ESTIMATED VARIANCE (WHICH IS DIVIDED BY N TO FIND THE VARIANCE IN
|     THE MEAN).  THE WAVES TO BE AVERAGED MUST BE 12 ELEMENTS LONG, THE
|     FIRST 6 BEING THE DATA POINTS AND THE LAST 6 BEING THE
|     CORRESPONDING UNCERTAINTIES IN THESE DATA POINTS.  OFTEN, SOME
|     DATA POINTS MAY HAVE UNCERTAINTIES OF ZERO.  THE AVERAGING
|     PROCEDURE IGNORES THESE POINTS AND KEEPS TRACK ONLY OF THOSE
|     POINTS WHOSE UNCERTAINTIES ARE NONZERO.  THUS, EVEN THOUGH 15
|     MEASUREMENTS MAY HAVE BEEN MADE FOR EACH QUANTITY OF INTEREST, THE
|     AVERAGE OF QUANTITY A MAY ONLY REPRESENT 12 MEASUREMENTS WHILE THE
|     AVERAGE OF QUANTITY B MAY ONLY REPRESENT 14 MEASUREMENTS.  FOR
|     RAMAN DATA, THIS COULD BE THE CASE IF A RAMAN LINE DOESN'T APPEAR
|     FOR SOME OF THE MEASUREMENTS.  THE FUNCTION ALSO CREATES TWO DUMMY
|     WAVES, STDSTAT AND WEIGHTSTAT, FOR COMPARING EQUAL WEIGHTING WITH
|     THE WEIGHTING BASED ON THE RELATIVE UNCERTAINTIES OF THE DATA
|     POINTS.  OF COURSE, WEIGHTSTAT IS A DUPLICATE OF THE WAVE NAMED BY
|     THE USER FOR STORAGE OF THE STATISTICAL DATA.

|     Refer to Philip R. Bevington, DATA REDUCTION AND ERROR ANALYSIS
|     FOR THE PHYSICAL SCIENCES (McGraw Hill Book Co., New York, 1969),
|     pp. 66-80.

|     Calculate Raman statistics of waves
      i=0
      do
            j=0
            sum1=0;sum2=0;sumx=0;count=0
            do
                  z=GetStrFromList(ls,j,";")
                  wave zq=$z
                  if (zq[i+6] != 0)
|     find sum of data for calculating the mean
                        sumx=sumx+zq[i]
|     find sum of the data points divided by their relative variances
|     for finding weighted mean
                        sum1=sum1+zq[i]/zq[i+6]^2
|     find sum of the inverse of the relative variances for finding the
|     weighted mean and the average variance
```

```
                        sum2=sum2+1/zq[i+6]^2
    count the number of data points with nonzero uncertainties
                    count+=1
            endif
            j+=1
        while(j < ct)
        j=0
        sumstd=0;sumxb=0
        do
            z=GetStrFromList(ls,j,";")
            wave zq=$z
            if (zq[i+6] != 0)
    sum of the square of the errors for finding the standard
    uncertainty in the mean
                    sumstd=sumstd+(zq[i]-sumx/count)^2
    sum of the square of the errors weighted by the relative
    uncertainties for finding the average variance (divide sumxb by
    N-1, then normalize by dividing this quantity by sum2/N to get
    average variance--divide average variance by N to get variance in
    the mean)
                    sumxb=sumxb+(zq[i]-sumx/count)^2/zq[i+6]^2
            endif
            j+=1
        while(j < ct)

        if (count > 1)
    find the equal-weighted mean and the uncertainty in the mean
            stdstat[i]=sumx/count;
                    stdstat[i+6]=sqrt(sumstd/(count-1)/count)
    find the weighted mean and its respective uncertainty
            weightstat[i]=sum1/sum2;
                    weightstat[i+6]=sqrt(sumxb/sum2/(count-1))
        endif
        reff[i]=weightstat[i];reff[i+6]=weightstat[i+6]
        i+=1
    while(i < 6)
    kill all loaded waves except statistics wave
    j=0
    do
        z=GetStrFromList(ls,j,";")
        wave zq=$z
        killwaves zq
        j+=1
    while(j < ct)
    ls="";ct=0
End
```

APPENDIX C

Wavelength Dispersion Linearity of Spectrometers

The dispersion of a spectrometer can be derived using the grating equation, given as

$$m\lambda = d \ (\sin\alpha + \sin\beta) \tag{52}$$

where m is the order, λ is the diffracted light wavelength, d is the grating period, α is the angle of incidence, and β is the angle of diffraction. For Ebert and Czerny-Turner mounts (typical for most spectrometers), the grating equation can be rewritten as

$$m\lambda = d \ (2\sin\theta \ \cos\phi) \begin{cases} \alpha = \theta + \phi \\ \beta = \theta - \phi \end{cases} \tag{53}$$

where θ is the grating angle measured from zero order and ϕ is a specific constant angle of the instrument. Equation (52) is used for a fixed grating with a constant angle of incidence α such as the case for detection using a CCD array detector and no spectrometer exit slit. Equation (53) is used for a grating which is scanned so that the angles α and β are both changing such as the case for detection of the light passing through the exit slit using a PMT. For the fixed grating case, the angle of incidence α is fixed so that the dispersion is $d\beta/d\lambda$. Reciprocal dispersion is defined as $d\lambda/d\beta$. Since the differential displacement dl of the image at the exit slit plane is related to the differential diffraction angle $d\beta$ by the focal length f of the focusing mirror using $dl=f \, d\beta$, the linear reciprocal dispersion D_{slit} is $d\lambda/d\beta$, usually expressed in Å/mm or nm/mm. This quantity is

also referred to simply as the linear dispersion of the spectrometer. The spectrometer used in the studies for this thesis is a 0.85 m Czerny-Turner double spectrometer, each half of which uses a 1200 lines/mm grating and has a specific angle ϕ of 6.25°. Since the CCD array detector was used in a fixed grating condition, the linear dispersion is one-half of the linear dispersion derived for a scanning grating in a PMT detection system. In addition, the resultant linear dispersion at the CCD detector, which is mounted on a double spectrometer with additive dispersion, is one-half that of a single spectrometer. These factors result in a linear dispersion that is one-fourth that of a single spectrometer in which the grating is scanned. The wavelength dispersion in this thesis is given as $D_\lambda = d\lambda/dp$ in which dp is the differential image displacement at the CCD array in pixels. Thus, $p\,dp=dl$, where p is the pixel length (23 μm). Therefore, using Equation (53), the wavelength dispersion for these studies is given by

$$D_\lambda = \left(\frac{1}{4}\right)\left(\frac{p}{f}\right)\left(\frac{2\,d\cos\phi}{m}\right)\cos\theta \qquad (54)$$

Note that the wavelength dispersion slowly decreases with increasing diffraction angle (or increasing wavelength). This effect is perhaps more easily seen if $\cos(\theta)$ is solved for in Equation (53) and substituted into Equation (54) to derive D_λ in terms of wavelength, given as

$$D_\lambda = \frac{p}{4mf}\sqrt{4d^2\cos^2\phi - m^2\lambda^2} \qquad (55)$$

The change in wavelength dispersion dD_λ/dp is given in terms of diffraction angle θ as

$$\frac{dD_\lambda}{dp} = -\left(\frac{1}{4}\right)\left(\frac{p}{f}\right)^2\left(\frac{2d\cos\phi}{m}\right)\sin\theta \qquad (56)$$

or in terms of λ as

$$\frac{dD_\lambda}{dp} = -\left(\frac{1}{4}\right)\left(\frac{p}{f}\right)^2 \lambda \qquad (57)$$

This last equation shows that D_λ decreases linearly with increasing wavelength. If the pixel position p_r and the wavelength λ_r of a reference atomic line on an acquired spectrum are known and the wavelength dispersion in the region of the spectrum is known, then the spectral data may be calibrated to a wavelength scale using a Taylor series expansion given by

$$\lambda(p_r + \delta p) = \lambda_r + \left.\delta p \frac{d\lambda}{dp}\right|_{p_r} + \left.\frac{\delta p^2}{2}\frac{d^2\lambda}{dp^2}\right|_{p_r} + \text{higher order terms} \qquad (58)$$

where δp is the difference in pixels between the reference wavelength and the wavelength in question. Using the definition of the wavelength dispersion D_λ, Equation (58) may be rewritten as

$$\lambda(p_r + \delta p) = \lambda_r + \left.|\delta p\, D_\lambda|\right._{p_r} + \left.\frac{\delta p^2}{2}\frac{dD_\lambda}{dp}\right|_{p_r} + \text{higher order terms} \qquad (59)$$

Using $f = 85$ cm, $p = 23$ µm/pixel, $\lambda_r = 556.27662$ nm, and $m = 1$ as typical system parameters for the majority of the studies concerning the 790 cm^{-1} region Raman modes of 6H SiC with a neon reference line, dD_λ/dp is found to be about -1×10^{-7} nm/pixel^2, a negligible rate of wavelength dispersion change over a 70 cm^{-1} range, meaning that the approximation

$$\lambda(p_r + \delta p) = \lambda_r + \left.|\delta p\, D_\lambda|\right._{p_r} \qquad (60)$$

is most suitable for wavelength calibration in these studies.

Raman Tensor Analysis

Raman tensors for the C_{6v}^4 point group symmetry[27] were used to determine the Raman active modes for each polarization configuration and the crystalline axis (c-axis) orientation relative to the phonon propagation direction. The effect of the microscope objective's NA is not considered since the purpose of these calculations is to roughly define the mode selection capability of the Raman microprobe for different experimental geometries. The Raman tensors for hexagonal C_{6v}^4 SiC, assuming symmetry in the off-diagonal elements, are shown in Table 14.

Table 14. Raman tensors used for hexagonal C_{6v}^4 SiC.[a]

$$
A_1 \quad \begin{vmatrix} a & & \\ & a & \\ & & b \end{vmatrix}
\qquad
E_1 \quad \begin{vmatrix} & & \\ & & c \\ & c & \end{vmatrix}
\qquad
E_1 \quad \begin{vmatrix} & & -c \\ & & \\ -c & & \end{vmatrix}
$$

$$
E_2 \quad \begin{vmatrix} & d & \\ d & & \\ & & \end{vmatrix}
\qquad
E_2 \quad \begin{vmatrix} d & & \\ & -d & \\ & & \end{vmatrix}
$$

[a] Reference 27.

The Raman mode calculation equation for the relative Raman scattered signal I_S is given as

$$I_S \propto \left| \vec{e}_s^{\,T} \cdot \overleftrightarrow{R} \cdot \vec{e}_i \right|^2 \tag{61}$$

where $\overleftrightarrow{R}$ is the Raman tensor, $\vec{e}_i$ and $\vec{e}_s$ are the incident and scattered field polarization vectors, and T denotes a matrix transpose of a column vector to a row vector. An

example of this calculation would be for the 180° backscattering configuration in which the incident and scattered wavevectors are parallel to the c-axis (in this case, the z axis) so the polarization vectors have components in the x-y plane given by

$$\vec{e}_i = e_{ix}\hat{x} + e_{iy}\hat{y} \text{ and } \vec{e}_s = e_{sx}\hat{x} + e_{sy}\hat{y} \tag{62}$$

so that the scattered intensity from the A_1 mode of $C_{6v}{}^4$ SiC is given by

$$I_S \propto \left| \begin{bmatrix} e_{sx} & e_{sy} & \end{bmatrix} \begin{bmatrix} a & & \\ & a & \\ & & b \end{bmatrix} \begin{bmatrix} e_{ix} \\ e_{iy} \\ \end{bmatrix} \right|^2 = |a \cdot e_{ix} \cdot e_{sx} + a \cdot e_{iy} \cdot e_{sy}|^2 \tag{63}$$

From Equation (63) it is evident that the signal for this A_1 mode is nonzero only if the incident and scattered light polarizations are parallel to each other. The notations for the appearance of this mode are given by $z\,(x, x)\,z'$, $z\,(y, y)\,z'$, or $z\,(xy, xy)\,z'$ in which a prime indicates propagation in the direction opposite to the indicated axis.

All the possible results for a 180° backscattering geometry are shown below in Table 15. Note that x and y may be reversed throughout the entire table and give identical results since hexagonal SiC is uniaxial.

Table 15. Polarization and propagation symbols used for determining phonon symmetry for $C_{6v}{}^4$ SiC in the 180° backscattering geometry (Note that x and y may be reversed for identical results).

Polarization Symbol	Phonon Symmetry	Propagation Symbol	Phonon Propagation Angle θ
-(x , x)- (parallel)	A_1 , E_2	z(- -)z'	0°
-(x , y)- or -(y , x)- (crossed)	E_2		
-(y , y)- (parallel)	A_1 , E_2	x(- -)x'	90°
-(z , z)- (parallel)	A_1		
-(y , z)- or -(z , y)- (crossed)	E_1		

APPENDIX E

Weighted Statistical Averaging

The Raman data obtained from each specimen was statistically averaged over the total number of spectra taken for a given specimen according to the following conventions. Weighted statistical averaging was chosen because it more accurately reflects the true uncertainty of an experimental measurement. The uncertainties of data obtained from an individual Raman spectrum were derived from least squares fitting uncertainties in fitting the Raman lines and from calibration uncertainties in the position of the reference atomic line. The following discussion on weighted statistical averaging was based on a treatment by Bevington.[28] The statistical mean and variance in the mean are given, respectively, by

$$\mu = \frac{\sum\limits_{i=1}^{N}\left(\dfrac{x_i}{\sigma_i^{\,2}}\right)}{\sum\limits_{i=1}^{N}\left(\dfrac{1}{\sigma_i^{\,2}}\right)} \text{ and } \sigma_\mu^2 = \frac{1}{\sum\limits_{i=1}^{N}\left(\dfrac{1}{\sigma_i^{\,2}}\right)} \tag{64}$$

where x_i and σ_i are the value and uncertainty of one data point in the sample to be averaged and N is the number of data points. Often, the relative uncertainties σ_i' of the data x_i are known, but the absolute uncertainties σ_i are not. This is the case for the Raman data of this research in that the fitting uncertainties give a relative uncertainty for comparison with similar data.

147

The absolute variances σ_i^2 can be estimated from the relative variances $\sigma_i'^2$ by

$$\sigma_i^{-2} = \sigma^{-2} \frac{w_i'}{\frac{1}{N}\sum_{j=1}^{N} w_j'} \tag{65}$$

where

$$w_i' = \frac{1}{\sigma_i'^2} \tag{66}$$

and

$$\sigma^2 \cong s^2 = \frac{\frac{1}{N-1}\sum_{i=1}^{N}\left[w_i' \cdot (x_i - \bar{x})^2\right]}{\frac{1}{N}\sum_{i=1}^{N} w_i'} \tag{67}$$

where σ^2 and s^2 are the estimated and weighted variances, respectively, of the sample.

The absolute weights w_i are given by

$$w_i = \frac{1}{\sigma_i^2} \tag{68}$$

and the average variance $\bar{\sigma}^2$ is given by

$$\bar{\sigma}^{-2} = \frac{1}{N}\sum_{i=1}^{N} \sigma_i^{-2} = \frac{1}{N}\sum_{i=1}^{N} w_i \tag{69}$$

From Equation (64), the variance in the mean σ_μ^2 is given by

$$\sigma_\mu^{-2} = \sum_{i=1}^{N} \sigma_i^{-2} = \sum_{i=1}^{N} w_i \tag{70}$$

Therefore, substituting the summation of w_i into Equation (69) gives

$$\sigma^{-2} \cong \bar{\sigma}^{-2} = \frac{1}{N}\sigma_\mu^{-2} \text{ or } \sigma_\mu^2 = \frac{\sigma^2}{N} \tag{71}$$

The uncertainty in the mean σ_μ can then be calculated by first finding the estimated variance of Equation (67) and substituting this result into Equation (71).

The statistical mean and variance of groups A and B can be obtained if the means μ_A and μ_B and the variances $\sigma_{\mu A}^2$ and $\sigma_{\mu B}^2$ are known. The overall mean and variance are given, respectively, by

$$\mu_T = \sigma_{\mu T}^2 \cdot \left(\frac{\mu_A}{\sigma_{\mu A}^2} + \frac{\mu_B}{\sigma_{\mu B}^2} \right) \text{ where } \frac{1}{\sigma_{\mu T}^2} = \frac{1}{\sigma_{\mu A}^2} + \frac{1}{\sigma_{\mu B}^2} \tag{72}$$

Equation (72) can be generalized in the following form:

$$\mu_T = \sigma_{\mu T}^2 \cdot \sum_{i=1}^{N} \frac{\mu_i}{\sigma_{\mu i}^2} \text{ where } \frac{1}{\sigma_{\mu T}^2} = \sum_{i=1}^{N} \frac{1}{\sigma_{\mu i}^2} \tag{73}$$

Equation (72) was used to compute the mean and variance of the Raman data from a group of specimens processed in the same way when the means and variances from each specimen are known. The uncertainties in the flexural strength data from some of the specimens were computed using the known standard deviation σ_{sd} and the number of measurements N to find the standard deviation in the mean σ_μ, given by

$$\sigma_\mu = \frac{\sigma_{sd}}{\sqrt{N}} \tag{74}$$